Role of City Texture in identifying Drag Coefficients of Buildings to prevent Hurricane Damage

by

Jacob Roxon

S.M. Civil and Environmental Engineering, MIT (2016)

Submitted to the Department of Civil and Environmental Engineering in partial fulfilment of the requirements for the degree of

Doctor of Philosophy in Civil and Environmental Engineering

at the

MASSACHUSETTS INSTITUTE OF TECHNOLOGY

February 2020

Signature redacted

Author ....

Department of Civil and Environmental Engineering

Signature redacted January 24, 2020

Certified by .....

Franz-Josef Ulm

Professor of Civil and Environmental Engineering

Thesis Supervisor

Signature redacted

Certified by ....

Roland J.-M. Pellenq

Senior Research Scientist in Civil and Environmental Engineering

Thesis Reader

Signature redacted

Accepted by ....

Colette L. Heald

Professor of Civil and Environmental Engineering

Chair, Graduate Program Committee

Role of City Texture in identifying Drag Coefficients of Buildings to prevent Hurricane Damage

by

Jacob Roxon

Submitted to the Department of Civil and Environmental Engineering
on January 24, 2020
in partial fulfilment of the requirements for the degree of Doctor of Philosophy in Civil and Environmental Engineering.

Abstract

Hurricane damage is one of the costliest and most frequent of natural disasters. In total, the cumulative cost of all 16 hurricanes in the US in 2017 was in excess of $300 billion and by 2075 the average annual damage cost in the US is expected to rise by nearly 40%. In order to mitigate disaster damage, governments mandate minimum standards for construction depending on location and building type—standards known as building codes. Yet most codes remain insufficient as they account only for individual buildings and overlook the influence of city layout on wind speeds and storm damage. To reinvigorate design codes and better predict hurricane damage, we propose a new city texture resilience approach, which accounts for local geometric layouts to predict more accurate building codes. Tested using computational fluid dynamics simulations for different city textures with common geometrical layouts, we found that the city texture model, derived using online GIS data of building footprints, predicts with 67% accuracy damage from 2018 Hurricane Michael in Mexico Beach, FL. Furthermore, we find that ordered "crystal" cites have higher susceptibility to hurricane damage showing higher proportion of buildings with upper range values of drag coefficients. Using this approach, stakeholders can readily identify entire cities (or neighborhoods) with high susceptibility to hurricane damage. Moreover, they can identify buildings with the highest risk of damage, which will offer targeted retrofitting, thereby enabling more resilient developments and urban planning to reduce the risk of hurricane damage and mitigate the kinds of extreme damage experienced by communities with histories of high speed winds, especially as climate change is going to intensify future storms.

Thesis Supervisor: Franz-Josef Ulm
Title: Professor in Civil and Environmental Engineering and Faculty Director at the Concrete Sustainability Hub

Acknowledgments

Supposedly the easiest, yet to a certain degree the hardest, this section brings pleasure and sorrow. Being the final part, on the one side brings an end, on the other a commencement. With many obstacles and turns, it wasn't an easy one to reach, but in the end, the support, help, encouragement that I have received along that way made it attainable, made it possible. Where there's a will, there's a way, but too often that will gets only ignited by friends and family. And it is those few who have been dear to my heart and those few who continue to remain the source of that inspiration I would like to share my sincerest and deepest gratitude with. More formally, I wish to extend this to the board of this thesis committee, my advisors, teachers, mentors: Prof. Marta Gonzalez, Prof. Franz-Josef Ulm and Dr. Roland Pellenq – you played an important role in my development and I wholeheartedly thank you for your performance.

Contents

List of Figures

List of Tables

Chapter 1

1. Introduction

In this chapter, we introduce the topic of climate change, its causes and consequences. We discuss common mitigation techniques and relate it to Urban Heat Island effect and energy consumption of buildings. We then transition to present climate change adaptation approaches focusing specifically on safety design codes for residential buildings. In the final part of this chapter, we introduce the role of cities—their history, growth and their function in the lives of humans—and different textures their buildings demonstrate. Towards the end, we present objectives of this research, followed by outline and significance of this thesis.

1.1. Climate Change

Extreme heatwaves in Europe during the summer of 2019. Severe tropical storms like Harvey, Irma, Michael, Maria, or Matthew. The most intense period of drought in California, USA, for almost a decade. Some of the most extensive and devastating wildfires in Australia. Records of extensiveness and damage coming from floods across the world. The climate is changing; and all disastrous events recorded in the second decade of the 21st century are a clear example of that. What's more, their intensity and quantity has been on the rise and despite the prediction of future severity of climate change, the effects have already begun to unravel (*1–3*). The time is to act is now.

Although our population appears not unified on the topic, there are many among us, ranging from students to political representatives, who recognize that the severity of the potential long-term consequences of the climate change (*4–6*). With its first global climate strike, year 2019 has become a historic one. Millions of people, kids, students, adults, people of all generations, but especially the younger ones, all over the world have been coming together to have their voices heard (*7*, *8*), to have our leaders do something about the climate changing, our planet warming up. *"The clock is ticking", "the time is now", "take it to the streets"*, are just some of the slogans that

have been visible on posters and fluctuating through social media. The argument has been that the crisis isn't going to wait, so neither should we. In more than three quoters of the countries, people are voting to end the era of fossil fuels. Young people have been leading the climate strike loud enough to awaken millions of adults. The fight won't be an easy one, as it is not one that history could guide as through. There are many unknowns in this complex climate equation, which is the core of the argument, whether or not the climate change is real.

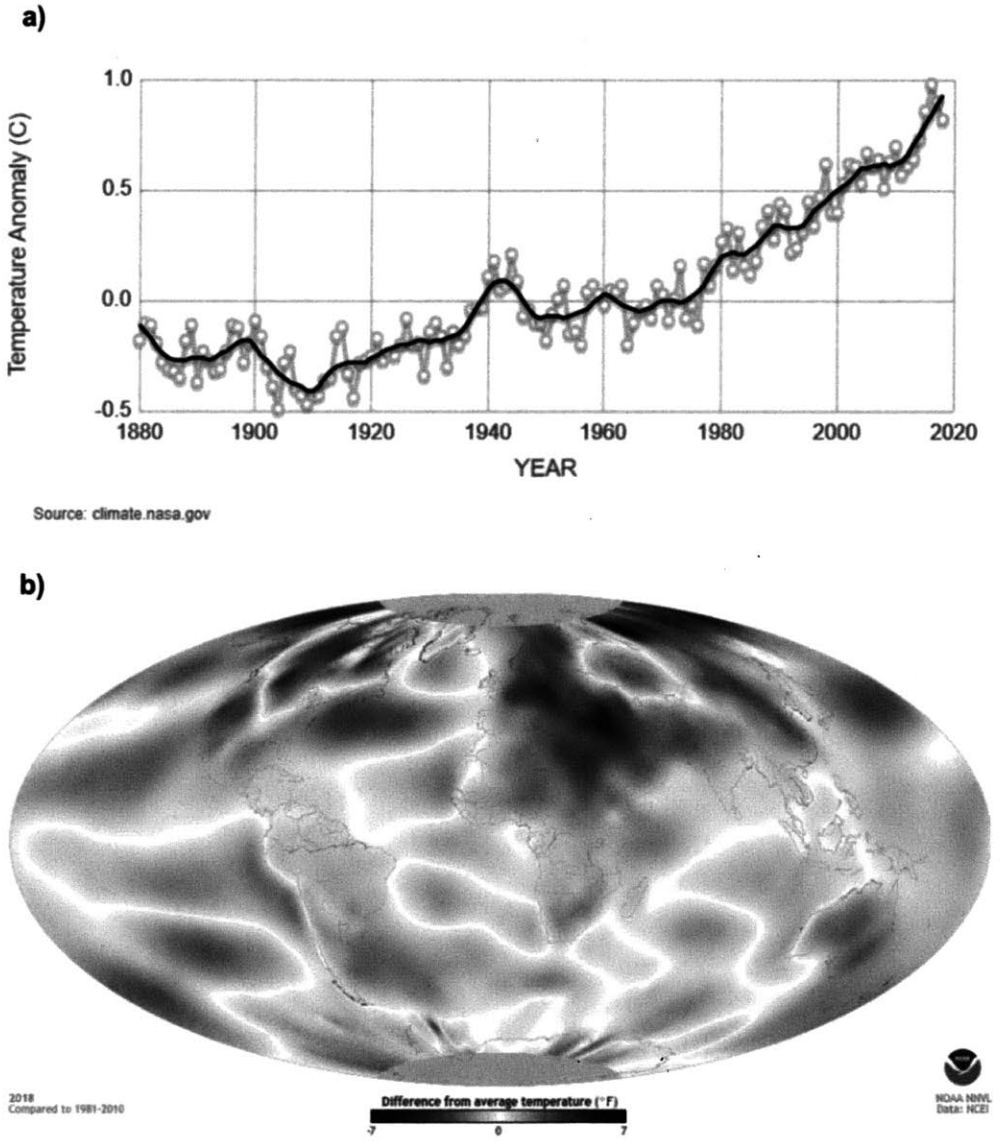

FIG.1-1 Global Climate Change patterns.

1.2. Consequences of Climate Change

Extensive data collected during multiple decades suggests that climate change is happening (*1*, *9–14*). Thousands of scientists argue that it is (*15*). The world with its extreme natural disasters is telling us it is (*1*, *3*, *16*, *17*). From north to south, from east to west, our planet earth has been warming up [Fig.1-1]. Earth's temperature goes up and down from year to year, but the fact is that in the past century the average surface temperature has increased by 1 degree Celsius [Fig.1-1.a, (*18*, *19*)] and as much as 3 degrees Celsius when compared to 1981-2010 averages [Fig.1-1.b]. However, in many places the temperature has increased even more. If this trend continues, we can be sure to expect much warmer future. And while this might appear appealing in some aspects, considering that many of the crops are more fruitful in warmer climates, or that people are more likely to enjoy living in a warmer climate, (especially those retiring) many research studies find that the cost of a warmer climate that we expect to occur far outweighs its potential benefits (*20*, *21*).

1.2.1. Rising Sea Level

Warming up climate is accompanied by extreme and often disastrous weather events with both short- and long-term impacts. Studies conducted by researchers over the recent years document that rising temperatures are going to lead to shifts in migrating patterns of wildlife, possibly also resulting in emigration from their natural habitats (*22–24*). Similar outcomes may the results of melting ice, especially at the north and south poles with millions of square miles covered with glacial ice. During the period of 23 years, between 1993 and 2016, experiments show that 286 billion tons of ice melted in the north pole, while 127 billion tons in the south pole with its rate of the mass loss tripling in the past decade (*25–28*). Much of that melting ice, in addition to thermal expansion of water due to increased temperature of water by 0.2 degrees Celsius since 1970s, is going to contribute to rising sea levels (*29*, *30*). With current predictions for increasing temperature, it is expected that by the end of the century sea levels will rise by 0.3-1.3 meters (*25*, *30*), although some experts believe that coastal areas should be prepared for the growth of 2 meters (*31*, *32*). Such rise would lead to an economic damage in excess of trillions of dollars, forcing millions of people to re-locate and lose their properties (*11*, *16*, *33*, *34*). Cities like New Orleans

LA, Miami FL, San Francisco CA, New York NY, Boston MA, and more worldwide, all located in coastal areas, are highly likely to have some parts of their land affected by sea level rises in the next century or two – the exact severity remains unknown. However, beyond the sea rising levels and the damage that comes with it, climate change poses another threat to our society, one that is going to have its effects visible in this decade with hurricanes and storms, droughts and floods likely to become more frequent and more severe in the near future.

1.2.2. Hurricanes and Storms

Predictive models for precipitations show an increased risk of severe droughts for many regions around the world (*35*), which can be explained by two factors: 1) general declines in climate related regional-precipitation and 2) increases in surface and air temperatures, which is going to cause earlier melting of the snow and for many days in the year result in rain instead of snow precipitation. In addition, precipitation rates are likely to decrease in quantity, but rise in intensity, which is going to translate to periods of dry weather with heavy and intense storms. These storms have already been prevailing around the world, causing an especially substantial damage in the US. According to research conducted by Office for Coastal Management from National Oceanic and Atmospheric Administration *"The cumulative cost of the 16 separate billion-dollar weather events in the U.S. in 2017 was $306.2 billion, breaking the previous cost record of $214.8 billion (2005)"*. In fact, some of the costliest in the American history hurricanes struck the US in the past 15 years [Fig.1-2]. However, the increasing quantity and intensity of storms accompanied by hurricanes (or their sole presence for that matter) is not a direct outcome of droughts; rather it can be attributed to an increasing water temperature. The warmer the water temperature, the more heat energy is available for a tropical cyclone to evolve, and eventually under the right set of weather conditions, a hurricane may emerge (*12*, *36*). While some studies on this topic suggest that there isn't enough evidence to link frequency of hurricanes with global warming (*11*, *12*), there is a consensus among scientist that there is a positive correlation between global warming and intensity of tropical storms (*16*, *17*, *36*). This global warming is believed to be induced by humans (*37*, *38*) due to an evident relationship between CO2 levels and temperature (*14*, *39*) [Fig.1-3].

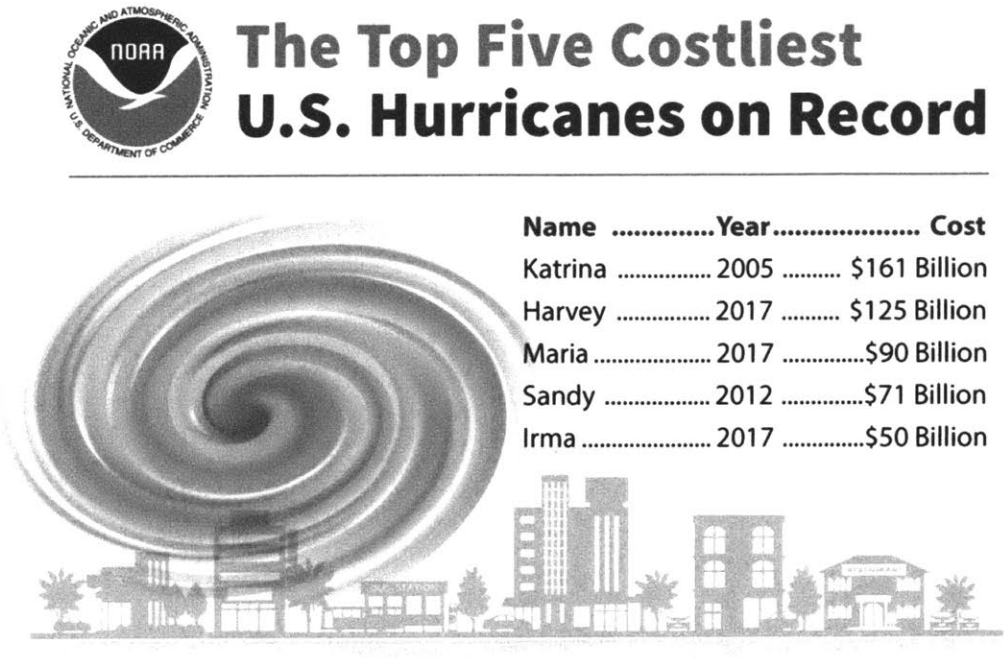

FIG.1-2. US Hurricane Damage Cost (*40*).

1.3. Greenhouse Gases

Although the amount of energy coming from the Sun has increased slightly over the past century, most climatic models are unable to reproduce the historical temperature trends without including an increase in CO_2 as well as other greenhouse gases (GHG) emissions (*9*). This is further justified by the fact that if GHG gases did not play a role in increased temperatures, we would expect to see temperature rise in all layers of the atmosphere, as opposed to only the lower part (*9*). This happens because greenhouse gases block the heat from the Sun that is reflected from Earth's surface. Increased GHG concentration in Earth's atmosphere leads to a stronger heat trap, which reflects greater amount of heat back to Earth's surface. These gases are composed of water vapor, carbon dioxide (CO_2), methane (CH_4), tropospheric ozone (O_3), nitrous oxide (N_20), chlorofluorocarbons, and carbon monoxide (not a direct GHG, but is able to modulate production of O_3 and N_20).

Although water vapor is the most abundant and potent GHG, its quantity increases as Earth's air temperature warms, but unlike other GHG, it is not generated directly from a human activity. Therefore, much of the scientific and societal focus has been focused on understanding

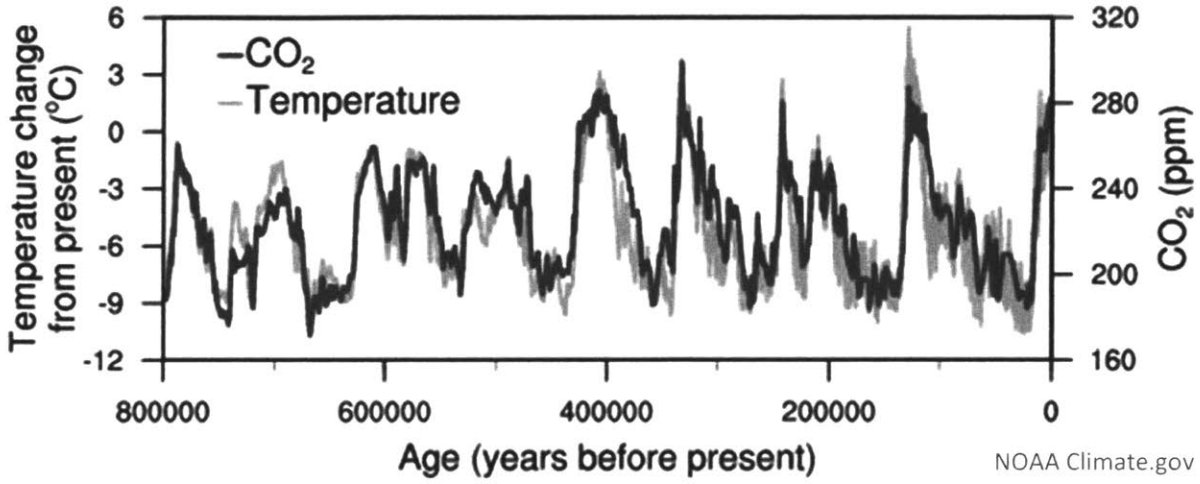

FIG.1-3 Correlation between Temperature (*14*) and Carbon Emissions (*39*).

the mitigation of other gases, especially reducing the amounts of carbon dioxide, which is the most prominent of the greenhouse gases [Fig.1-4]. Carbon dioxide is released through human activities ranging from land use changes, deforestation to burning fossil fuels; it is also released through natural processes, such as respiration or eruptions of volcanos. However, since 1950s the main cause for the increase in CO_2 concertation has been humanity burning fossil fuels (*41*, *42*) at a rate that in 50 years has increased CO_2 levels by almost one third [Fig.1-5.b] from a level that had already been higher than the highest previous known CO_2 concertation over 330,000 years ago [Fig.1-5.a]. To verify the hypothesis about the impact of human activity, a panel of hundreds of scientific experts from countries across the globe agreed that we, the people, are solely responsible for intensified warming climate (*15*). In order to mitigate the coming consequences of climate change, to adapt we must find ways to reduce sources of CO_2 sources and adapt for the future for more resilient and sustainable infrastructure.

1.4. Climate Change Mitigation

On the mitigation side, there is a wide range of readily available solutions that can help us, both individually and in larger groups, reduce the rate at which we are burning the fossil fuels. In recent years, global leaders and legislators have come to recognize the perils of climate change and under the United Nations Framework Convention on Climate Change, in 2016 the Paris Climate Agreement was established with the long-term goal of reducing GHG emissions and keeping the global temperature rise below 2°C above pre-industrial levels. However, in 2017 the second largest domestic polluter and first in the western hemisphere, United States of America, had its federal government announce that it would cease its participation in the global climate change mitigation efforts captured in the charters of the Paris Accord. Moreover, in 2018 under the Section 201 of the Trade Act, the federal government has imposed new tariffs on solar energy imports, which in

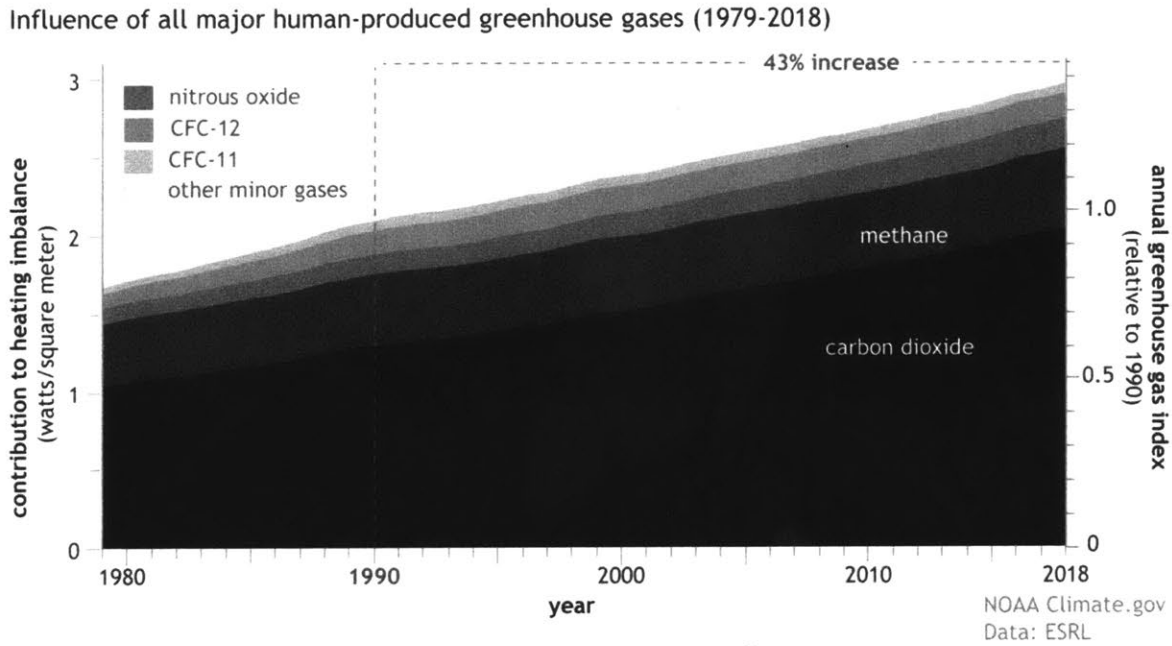

FIG.1-4 Global Human-Produced Greenhouse Gases.

the past few years created limited interest in renewable energy growth in the US. However, encouraged by climate supporters worldwide and recognition of future consequences and potential benefits of more energy-efficient technology, many business, cities and some states across the US have voluntarily come together to declare the *"We are still in"* and *"America's Pledge"* coalitions

that will continue to support the climate action plan to meet the Paris Climate Agreement. Although, US Climate Alliance of this kind has the potential to mitigate the effects of climate change, majority of the US nation continues to be under no official obligation to reduce carbon emissions and improve energy efficiency. This poses a great environmental threat to the US and rest of the world for two reasons: first the effectiveness of energy policies is much higher when compliance is mandatory as opposed to voluntary (*43*, *44*) and second, US has the second largest CO_2 emissions in the world. Unequivocally, establishment of mandatory regulations is a portion of the challenge to achieve goals of the Paris Agreement; however, the other important portion of the challenge is selection of the sector and approach that would offer the greatest opportunity for economic and environmental changes rather than be solely a climate mitigation solution (*45*, *46*).

1.4.1. Energy Consumption of Buildings

According to International Energy Agency, electricity and heat production combined with buildings make up almost 60% of the world's CO_2 emissions, which creates a huge opportunity for reduction of emissions with more sustainable, energy efficient infrastructure (*47–49*). This mitigation potential extends to United States where Energy Information Administration (EIA) estimates that 40% of total domestic energy consumption buildings are the single most energy consuming source of infrastructure in the US and thus have been the primary focus of energy policies (*50*). Space heating and cooling is estimated to contribute to about 20-25% of total energy consumption (*51*), which for the US residential stock of about 113 million units translates to about 10% of the total domestic energy consumption. Globally, the impact of the residential sector is even more significant – it is estimated that its contribution to total energy consumption is 27%, which translates to 17% of CO_2 emissions (*38*).

a)

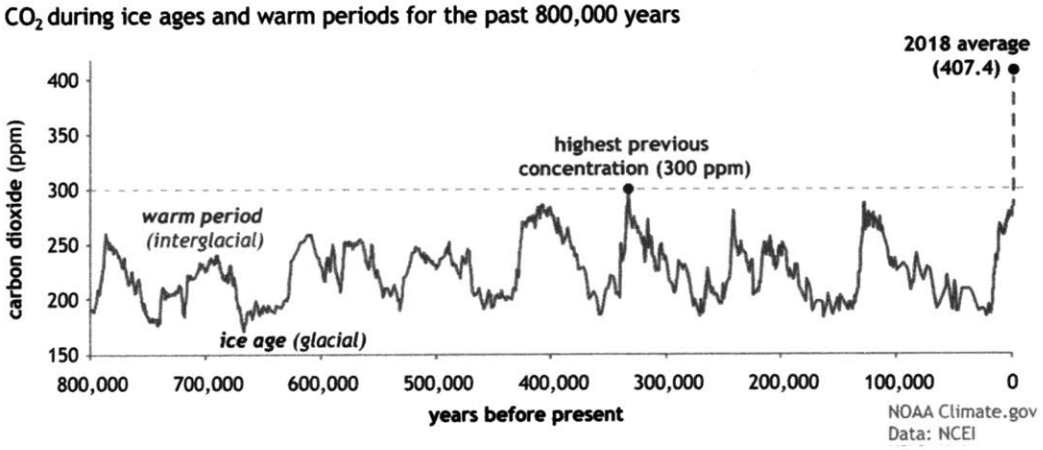

b)

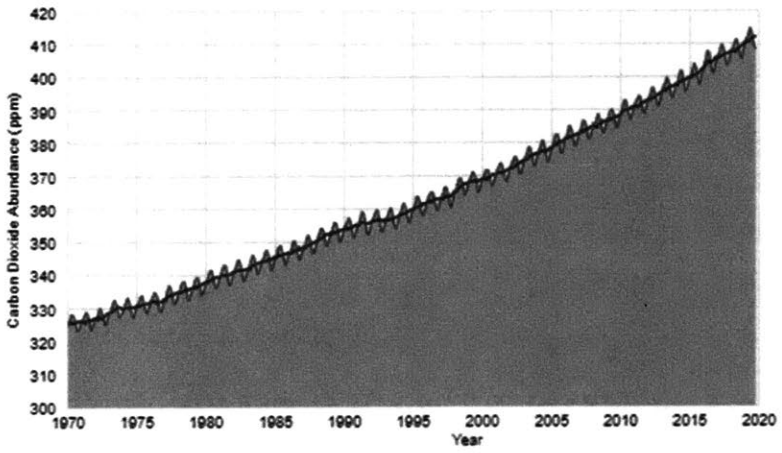

FIG.1-5 Historical Carbon Dioxide Atmospheric Concentration

1.4.2. Urban Heat Island

One of the main factors that influences energy consumption of residential buildings is outdoor air temperature (*52*). That temperature depends on both regional and local climates. With wind, cloud coverage and seasonality, the former is considered an uncontrollable variable (*53*). The latter one, however, is influenced by the humankind and shaped through urban growth (*54*, *55*). This is because urbanization changes the structure of natural land by replacing open areas and vegetation with various forms of infrastructure. Buildings and pavements are arranged in different geometrical layouts (*56*, *57*) and use different types of materials (*58*), both of which are known to

influence the amount of solar radiation that is stored during the day and its release rate at nighttime. In addition to storage and release of radiant energy, ventilation (*59*), indoor temperatures (*60*) and anthropogenic heat (*61*), all have been listed as factors that lead to thermal changes in the environment causing formations of UHIs. Although, there is no general consensus on the magnitude of local temperature changes with different studies estimating its values to be (i) (*62*) 5-15°C, (ii) (*55*) 1-8°C, (iii) (*57*) 1.4-4.2°C at nighttime, (iv) (*56*) 1°C, (v) (*63*) 3°C. Nighttime UHI is dominated by two factors: 1) the ability of materials to store solar radiation during the day, and 2) the rate at which this energy is released at night (*64*). For the day-time UHI, detailed periodic hourly variations have been found to be related to changes in convection efficiency in the lower atmosphere between different climate zones (*60*). It has been estimated that average daytime UHI causes air temperature to intensify by 1-3°C in the US (*65*) and 1.72°C globally (*66*). While it is well known that the release of solar irradiance heat at night is the inducement of intensified temperatures in cities (*64*), detailed quantitative descriptions of correlations with city texture parameters are mostly limited to single street canyons (*67*). Changes in material properties (*68*), or geometries of infrastructure (*69*, *70*) instigate an alternation of various physical processes at Earth's surface leading to notable climate effects, such as UHI. These processes reveal geographical and periodic (i.e. hourly, daily, seasonal) influences on higher temperatures that come in a form of UHI (*71*, *72*).These higher temperatures, in general, necessitate higher energy demand, which translates to economic and environmental losses for cities worldwide (*50*, *66*). Beyond increased energy usage, UHI has been found to create externalities in the forms of increased air pollution (*53*, *73*) and deteriorated human comfort (*74*), which during extreme heatwaves has been attributed to augmented mortality rates (*75*). Moreover, with global climate change patterns (*76*) and urban growth (*77*), future impacts of UHI are expected to intensify (*66*). Because of that, UHI mitigation strategies and techniques—traditionally to include tree and vegetation (*53*) cover and reflective pavements (*73*)—have been studied extensively with their importance expected to grow in the future (*78*). Reflective materials, cool and green roofs and cool pavements have proved to be successful in diminishing negative UHI effects (*65*, *79*). Most of the UHI studies have been focused on quantifying the impact on the demand for cooling energy during hot summer months (*50*, *53*, *73*), leaving the topic about the influence of UHI on the annual heating and cooling energy sectors in the need of further investigation. Energy modeling of buildings and numerical simulation have been used to provide comprehensive assessment of UHI

mitigation tactics on the building's energy demand. Reductions of outdoor temperate of 1°C during peak time cooling energy demand could reduce energy consumption by as much 6% (*80*). However, during cold winter months, heating energy may be halved in urban areas when compared to their rural surrounding due to UHI effect (*81*). It is important to note that while reducing UHI in areas with high cooling energy demand is beneficial for the economy and environment, in regions with high heating and low cooling energy demands, alleviating UHI is likely to increase overall energy costs and pollution. Therefore, in order understand the impact that UHI has on energy consumption, annual heating and cooling energies, rather than just solely summer or winter months, must be considered. The outcomes of such studies suggest that in the presence of UHI, the combined annual heating and cooling energy may decrease (*82*). However, more regional energy modeling studies are needed to evaluate the impact of UHI effect and its countermeasures on the energy consumption of the entire state or country. Above all, any studies should account for the climate change by using climatic predictions for intensified air temperature (*83–85*).

1.4.3. Energy Consumption Models

Building energy modeling techniques for regional or national studies for residential energy consumption can be divided into two types (*86*): (1) top-down and (2) bottom-up. Top down models rely on historical aggregate energy consumption data and generally are considered to be simplistic with small number of input variables providing average estimates of the energy consumption. As such, they lack the ability to account for new stock of buildings, any advances in building energy technology or identifying areas for improvements. However, it is their simplicity and availability of data that makes them an attractive choice for many national building energy modeling studies. The second category, bottom-up models are known for their high level of detail and ability to identify areas for improvements and measure their future impact; however, this comes at the price of increased complexity and necessity for more input data, which oftentimes requires energy bill data that generally is limited to the local scale. As such, bottom-up models work best for studies that aim to identify specific areas for improvements and quantify predictions for future energy consumption.

1.5. Climate Change Adaptation

The impacts of UHI for the entire energy sector, on average, have found to be negative for the economy, environment and society (*11*, *16*, *33*, *37*). In the future of global climate becoming warmer (*84*), these effects are only going to magnify. Although, we have policies in place and public support to adopt mitigation methods to reduce global CO_2 emissions, we should also allocate our resources to prepare ourselves for the future consequences of climate change, which includes frequency and intensity of droughts, floods, storms and hurricanes (*13*, *17*, *27*, *35*). Hurricane damage is one of the costliest and most frequent of natural disasters. In total, NOAA's figures show that the cumulative cost of all hurricanes in the US in 2017 was in excess of $300 billion and by 2075 the average annual damage cost in the US is expected to rise by nearly 40%. Engineers and scientists have established a set of retrofitting approaches, which have the potential to prevent damage (*87–91*).

1.5.1. Building Design Codes

An example of that would be a single building in Mexico Beach, Florida, USA that withstood damage from hurricane Michael in 2018, a building that was built with elevated steel and concrete foundations, reinforced joints, glass, roof shingles (*92*) – a full hurricane proof structure capable of withstanding speeds beyond greater than the maximum category (cat. 5) hurricanes with speeds above 75 m/s. That building is a prime example of an appropriate structural specification, a code, which considering the failure of most buildings, had been selected to be above the minimum standards required by the local and/or state requirements, whichever one exceeds (*93*, *94*). Despite extensive and devastating damage in Mexico Beach, Michael isn't the only example of a hurricane that destroyed residential buildings failing under the code standard during a hurricane cat 3 or 4. Yet, according to FEMA, *"Building codes are sets of regulations governing the design, construction, alteration, and maintenance of structures."* Their purpose is to protect the inhabitants of a building from natural disasters by specifying the strength of that building. And for majority of the cases in fact they do. Codes come in a form of guideline with most common structures (*93*), which allow the engineer to identify appropriate pressure loads in a specific wind environment, which is based on historical wind speed maps (*93*, *95*). However, these maps don't

get updated frequently enough, which with the increasing intensity of storms in the future is going to become even a bigger problem (*16*, *34*, *37*). But there is another challenge, which comes from the shape of the building. To keep buildings safe from wind hazards, codes stipulate how a building must interact with the wind, a value known as a drag coefficient. The drag coefficient of a building determines the amount of air resistance it will experience when exposed to the wind. As a building's drag coefficient increases, the damage it experiences can as well. Design codes assume that buildings have a range of drag coefficients, which is composed of exposure, environment and purpose (*93*, *95–97*), which makes it fixed for specific group of buildings (i.e. residential) – in some ways makes sense, since the shapes of buildings do not change much (*98*, *99*) and the variations of drag coefficients with increasing speed is minimal in turbulent regimes (*100*). Yet most codes remain insufficient as they account only for individual buildings and overlook the influence of city layout on wind speeds (*101*, *102*), which has been found to vary depending on planar (*99*, *103–105*) and frontal density (*106*, *107*), changes depending on wind direction (*108*, *109*), and size of the height to width ratio between buildings (*103*, *110*) – a metric also known as urban canyon. Such canyons, just like building densities, in some cases can reduce wind loads by offering shelter to certain buildings, but in other cases they have the potential to magnify wind speeds (*104*, *107*, *111*) by several factors of what the norm requires. To understand the impact of building heights, it is critical to study variability of heights—a parameter also known as surface roughness—in city-like environments (*109*, *112*). However, the underlaying challenge with any of the wind tunnel experiments (*113*) or wind flow computational fluid dynamics models (*109*, *114*) used to derive these correlations is that by being predominantly highly ordered, regular grid or staggered configurations (*103*, *111*), they rarely are able to capture the unique geometrical layouts that prevail in urban and suburban environments (*57*, *115*).

1.6. Role of Cities

The world as we know it converges to cities. Over 55% of the population lives in urban areas and urban migration rates have been on the rise with over 75 millions of dwellers annually in the past five years moving into cities [Fig.1-7]; and although United Nations estimations suggest that the rate of urban growth is going to decline in the 30 years, medium variant projections conjecture that each year approximately 9 cities of the size equivalent to the current population of New York City,

NY [Fig.1-6] are going to have to be built in order to accommodate growth and inflow of new urban residents. This poses an extreme—of higher than ever before magnitude—challenge on our society to create even more sustainable, resilient and appealing to live in environments, historically defined as fundamental reasons for admiration of cites. Of course, it would be wrong to say that cities are superior in every aspect. In fact, human history and culture did not originate in cities (*116*), and it wasn't really until the last century or so that they have become the focal point of our societal needs and desires (*117*, *118*). A natural instinct of our humanity is to strive for ameliorated life and it is a reciprocal palpability that cities have the greatest potential to provide foundations for those vital needs and desires (*117*). While, it would be contemptuous to undervalue the significance of non-urbanized land on human life, the spectrum of our interest extends far beyond the rural areas; urban zones cover a minor portion of the global land, a mere 2% in fact, yet they form home to greater portion of the population, which for the more developed parts of the world stands at the mark exceeding 75%. Since the middle of 20th century, the ratio of people living in cities has almost doubled from 30% to 56% and is expected to reach two thirds by the middle of 21st century (*119*). In less relativistic terms, the overall numbers of the urban swift are as follows: urban dwellers are projected to be pullulated from today's 4.3 billion to 6.7 in 2050, and rural inhabitants are expected to experience a shift in the opposite direction from 3.2 to 3.1 billion. Moreover, high urbanization rates establish an additional factor of importance to the urban growth equation magnifying the relevance of cities exclaiming for an augmented input from experts in the fields of science, engineering and architecture. Unequivocally, in order to accommodate the profound changes in socioeconomic systems and land usage, exigency for new cities is formed. And although they will revivify the economy (*118*) and foster prosperity (*117*), they will also elicit imperative environmental and health concerns (*120*), impacts of which will be significant, yet are not fully comprehensible by our humanity (*121*).

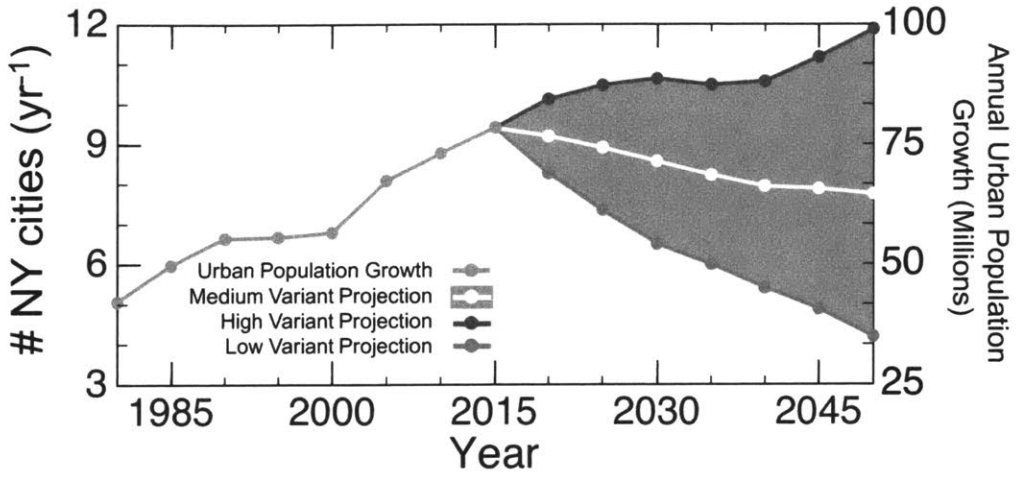

FIG.1-6. Urban Population Growth.

Global historical annual growth of urban population between 1980 and 2015 and future expectations (secondary y-axis) presented as a number of cities of size equivalent to New York (NY) City (primary y-axis) necessary to be built in order to accommodate that growth. The data has been derived using 5-year interval projections and 2014 NY population. Urban population growth data can be obtained from United Nations, Department of Economic and Social Affairs, Population Division (2015), World Population Prospects: The 2015 Revision, DVD Edition.

1.6.1. City Texture

However, the urban challenge is not just demographic – rather it incorporates the more complex nature of dynamic and heterogeneous landscapes, ever evolving frameworks that aim to establish a stable linkage between nature and society. At their zenith, life prospects offered are virtuous – foundations for the highest form of communities (*122*). Supported by the expanding concentration of people, such systems employ socioeconomic magnets that exert an efficacious and dynamic growth. At first glance, this scaling appears to be a chaotic single cluster emerging from a focal point, which typically is considered to be the central business district (*123*). However, in more depth analysis of city morphology unravels geometrical symmetries and social networks of interconnected clusters, fractal and molecular patterns (*124*) that can be studied to develop models with the potential to unify the efforts of experts from diversified fields of science, architecture and engineering bridging the gap between the form and function. Emphatically, cities are complex structures that emerge from a collection of complementary ingredients (infrastructure,

transportation, economy, social networks etc.), which in isolation and short term can be understood, but collectively their long-term impact has proven to be unpredictable and lacking quantitative component (*124–126*).

In the past century, but most notably in the last decade, urban planners, scientists, economists and sociologists have demonstrated unified efforts to study form and growth of cities on the path of deriving the urban equation to create smart, sustainable and resilient cities (*125–127*). The classical approach of city planners and architects to shape the urban space has challenged them with establishing a healthy compromise between what is aesthetically pleasing and functional. With time, however, novel changes have been incorporated to maximize the efficiency and justice within the boundaries of the city constrained by the aligned forces of its government and economy. A Theory of Good City Form was developed (*128*), which in its underlying essence argues that in addition to the two earlier mentioned factors (aesthetics and function), city's performance is a measure of five additional variables: fit, access, vitality, sense and control. A just city is one with a fair allocation of resources, it provides the means of domiciliating infrastructure with networks for the urban dwellers (fit), while not suppressing the diversity of age and culture (access). It must be sustainable and safe (vitality) and allow people to comprehend its purpose (sense), which has a potential to be adjusted to satisfy the current needs and desires of its occupants (control). A city of a good form is established when the linkage of these aspects becomes efficient. City planning, thus has become an eloquent and sophisticated method that aspires urban growth, which accordingly derives its roots from the interests of the public. For such methodology to function, the spatial growth must be a reflection of the spatial order, which can be enacted through the spatial discipline; for instance, functioning of the city can be ameliorated by introducing division of space arranged into discrete units to facilitate smooth economic and social growth characteristic of the changes in population and land. Unfortunately, however, perfect order of this kind has not found its way yet to be transformed from a theoretical utopian dream to a comprehensive restructuring practice visible in metropolitan zones (*129*). It is believed that the complex interactions between spatial arrangements and urban agents are the fundamental obstacles that hold back the transformation of chaotic and isolated urban space into a smoothly operating totality (*115*), which consequently may (and oftentimes do) lead to negative socio-economic and health effects. While, there are many questions yet to be answered by urban scientists in the context of their existence, form and sprawl,

herein the focus lies in understanding quantitatively the unique texture of cities and the impact it has on sustainability and resilience of cities; herein analyzed in the context of UHI and hurricane damage, especially as climate change intensifies future temperatures and storms.

1.7. Research Objectives

As we have established, climate change is going to have negative impact on our communities. Moreover, the frequency and intensity of storms and UHIs are going to increase as the climate becomes warmer in the future. Are our communities ready? How are cities going to prepare? In order to answer these questions, we begin by quantifying city texture for 43 cities worldwide and comparing them to 16 regular and staggered grids with disordered and ordered building configurations. Using local texture parameters, we identify a unique set of parameters that allow us to categorize cities as gases, liquids and crystals. Furthermore, we utilize these parameters to reconstruct statistical model of cities, which we use in wind flow simulations. In the end, we provide an insight on the influence of city texture on the intensity of Urban Heat Islands using a simplistic radiative heat model and the intensity of wind pressure loads acting on buildings during hurricanes using an enhanced frontal density model.

1.8. Thesis Outline

Following the 1) introduction part, there are five additional chapters that form this thesis. 2) Data acquisition and editing lists the raw data required for this study and the preparation process needed to prepare inputs analyses in chapters 3, 4 and 5. In chapter 3) we provide a detailed description of the Urban Physics methodology used to quantify local city texture parameters and how to use them to reconstruct their samples. In chapter 4) we derive a correlation between UHI and city texture and analyze residential heating and cooling cost of UHI. In chapter 5), we study the impact that local city texture has on wind building damage and derive a hurricane risk damage model. Final chapter 6) concludes the preceding work by depicting the potential of individual parameters, practical utilization strategies and the future research steps.

1.9. Research Significance

While many climate change mitigation solutions and adaptation techniques for existent cities have already been established, due to complex nature of urban infrastructure, general and simple to follow design guidelines for building more resilient to hurricane damage and changes to heat urban environments are still missing. Here, we show that the complexity of city networks can by examined with tools borrowed from statistical physics to derive novel urban norms in the form of city texture. We present that these techniques offer a unique insight on the role that textures of cities have in Urban Heat Island at nighttime, which from the financial and environmental perspectives may not always be negative. Moreover, at the local level, we find that the herein quantified unique geometrical patterns, or textures, can be used to explain changes in local wind speeds and lead to intensified, to what current design norms predict, coefficients in preventing building failure during hurricanes.

1.10. Summary

In this chapter we have established the eminence of climate change, while providing a general overview of its mitigation and adaptation techniques, specifically for Urban Heat Island and hurricanes. We elaborated on existing safety design norms of buildings and the changing role of cities in our communities. We have also explained the objectives, outline and significance of this work.

Chapter 2

2. Data Acquisition and Management

In this chapter we present the procedure with sources for acquisition of raw input data for the analyses we conduct in this work, explained in chapters 3-5. We begin with the air temperature and geographical information system (GIS) data for building footprints from online GIS databases and online mapping tools. For each process, we explain editing and limits we adopt that allow us to prepare samples in accordance with model requirements from proceeding chapters. We end this chapter with a comparison of GIS and online mapping building footprints data for validation purposes.

2.1. Air Temperature

Data is obtained using National Oceanic and Atmospheric Administration's (NOAA) extensive database. For major cities in the US, we search for stations located in urban part of the city as well as their rural surrounding environment used for temperature comparison. While ideal case would entail a situation with rural station located right outside the city's boundaries, for majority of cities we had to extend our searches for rural stations to tens of kilometers, which aligns directly with methods used by others in this field (*71*, *130*).However, to minimize the climatic regional difference impact on temperature for selecting stations, we applied the following limits as part of the selection process criteria:

1. Stations should not be separated by more than 100km in the horizontal plane
2. Stations should not be separated by more than 100m in the vertical plane.
3. Stations should not be located at major international airports.

For many cities, the above limitations left us with more than just a single rural station. To select the most appropriate pair, we compared temperatures for those multiple rural stations with the data obtained from the reference urban station. If, for a given day 4 or less hourly values had been missing, we would replace them with daily averages for that day. Days with more than 4 hourly

values missing were disregarded from calculations. Furthermore, we disregarded files for which more than 15% of hourly values were missing. For the remaining stations that for most were collections of almost 10 years of data for a period between 01/01/2006 and 12/31/2015, we finalized our selection to rural stations that would result in the highest temperature difference values for each city [Table 2-1]. In the end, we obtained a sample of twenty-two US urban air temperature time series for a period of multiple years, which is a sample large enough to provide us with statistically relevant data, but for the time series not too large to be influenced by global warming effects during a single decade (*84*).

		Urban Station			Rural Station		
	City	Name	Start Date	End Date	Name	Start Date	End Date
1	Austin, TX	Austin Camp Mabry	1/1/2006	6/30/2015	Largo Vista Rusty Allen	8/25/2008	6/30/2015
2	Boston, MA	Boston	2/1/2010	6/30/2015	Norwood Memorial	1/1/2006	6/30/2015
3	Chesapeake, VA	Money Point Va	1/1/2006	6/30/2015	Suffolk	1/1/2006	6/30/2015
4	Chicago, IL (1)	Calumet Ii	1/1/2006	6/30/2015	Burlington	1/1/2006	6/30/2015
5	Chicago, IL (2)	Chicago/Midway	1/1/2006	6/30/2015	Burlington	1/1/2006	6/30/2015
6	Dallas, TX (1)	Dallas Executive	1/1/2006	6/30/2015	Grayson County	1/1/2006	6/30/2015
7	Dallas, TX (2)	Dallas Love Field	8/1/2010	6/30/2015	Grayson County	1/1/2006	6/30/2015
8	Hartford, CT	Hartford-brainard	1/1/2006	6/30/2015	Norwood Memorial	1/1/2006	6/30/2015
9	Houston, TX (1)	Huston/Dunn Helistop	1/1/2013	6/30/2015	Beaumont Muni	3/10/2011	6/30/2015
10	Houston, TX (2)	Manchester	8/14/2012	6/30/2015	Beaumont Muni	3/10/2011	6/30/2015
11	Los Angeles, CA (1)	La Usc Downtown Cam	1/1/2006	6/30/2015	Marine Corps Air Station	1/1/2006	6/30/2015
12	Los Angeles, CA (2)	Jack Northrop Fld H	1/1/2006	6/30/2015	Marine Corps Air Station	1/1/2006	6/30/2015
13	Los Angeles, CA (3)	Long Beach/Lb Airp.	1/1/2006	6/30/2015	Marine Corps Air Station	1/1/2006	6/30/2015
14	Louisville, KY	Bowman Field	1/1/2006	6/30/2015	Bedford 5 Wnw	10/3/2007	6/30/2015
15	New York, NY (1)	Bergen Point	1/1/2006	6/30/2015	Dutchess County	1/1/2006	6/30/2015
16	New York, NY (2)	New York/La Guardia	1/1/2006	6/30/2015	Dutchess County	1/1/2006	6/30/2015
17	Oklahoma City, OK	Wiley Post	1/1/2006	6/30/2015	Watonga	1/1/2006	6/30/2015
18	Philadelphia, PA (1)	Northeast Philadelphia	1/1/2006	6/30/2015	Robert J Miller	11/14/2007	6/30/2015
19	Philadelphia, PA (2)	Philadelphia	1/1/2006	6/30/2015	Robert J Miller	11/14/2007	6/30/2015
20	Seattle, WA (1)	Seattle	1/1/2006	6/30/2015	Arlington Municipal	1/1/2006	6/30/2015
21	Seattle, WA (2)	Seattle Rent	1/1/2006	6/30/2015	Arlington Municipal	1/1/2006	6/30/2015
22	Washington, DC	Washington	7/24/2008	6/30/2015	Culpeper	1/1/2006	6/30/2015

TABLE 2-1. Sources for Temperature Data

2.2. Energy Cost

To quantify energy costs, we resort to a regression statistical bottom-up approach to perform a 12-year financial and environmental analysis of temperature and urban heat island for 48 US states (due to lack of data Hawaii and Alaska excluded) using annual household space heating and cooling energy consumption data combined with air temperature values, state prices for heating and cooling energy sources and carbon emissions associated with production of specific types of

energy. Due to limited availability of heating and cooling energy consumption data in the US for the commercial sector, our study is focused only on the residential stock of buildings. To obtain building energy consumption, we resort to the EIA's database—available to the public use—residential energy consumption surveys that were created using bottom-up modeling approaches. Although, the most recent energy survey was created for year 2015, its geographical resolution is too low for the purposes of our study – it divides the US into 4 regions. Therefore, we utilize the most recent version of the energy consumption, which offers the resolution at the state level. The earliest available dataset that offers that, is 2009 Residential Energy Consumption Survey Data (*131*). Using previously established regression models (*86*), we investigate the correlation between average annual household heating and cooling energy and annual heating and cooling degree days.

2.3. Degree Days

Degree days are a common metric used in the energy industry for calculating the effect that outdoor air temperature has on building's heating and cooling energy consumption. They are divided into two categories: Heating Degree Days (HDD) and Cooling Degree Days (CDD). HDD measure for how many days and how many degrees the air temperature was below a reference temperature, in this case (and typically) 65 °F. On the other hand, CDD measure the number of degrees above that reference value. Regional monthly or annual degree days can be obtained directly from the National Oceanic and Atmospheric Administration (NOAA) (*132*).

2.4. Geographic Information System (GIS) Data

Principal input data used in this study used to quantify city texture consists of GIS building footprints. Building footprints are commonly used by city's or state's GIS departments for network analysis and visualization purposes of urban geometries. They come in a form of shapefiles, which in addition to GPS coordinates of buildings' footprints may also store information on building properties, such as year of construction, number of floors, roof height, etc. However, while all this information may be useful, it is not necessary for this study – the minimum information required is merely 2D GPS coordinates of building footprints for an entire city. This type of information may be obtained directly from a city's GIS department [Table 2-2], where oftentimes they offer

more than just GPS coordinates. However, this approach generally only works for cities in the US and few major cities in Europe. For the US, it is also possible to download them directly for each state using data generated by Microsoft (*133*). With current accessibility to online data, however, the best approach to obtain GIS data is to refer to online mapping tools, such as Google or OpenStreetMap (OSM) maps, which have building footprints embedded as a layer in their maps.

		City	GIS Source
1	a	Austin, TX	ftp://ftp.ci.austin.tx.us/GIS-Data/Regional/coa_gis.html#environmental
2	b	Boston, MA	MIT University GIS Department
3	c	Chesapeake, VA	https://github.com/jonahadkins/chesapeake-OSM-imports
4	d	Chicago, IL (1)	https://data.cityofchicago.org/Buildings/Building-Footprints/6mpq-sfwi
5	e	Chicago, IL (2)	
6	f	Dallas, TX (1)	http://gis.dallascityhall.com/homepage/shapezip.htm
7	g	Dallas, TX (2)	
8	h	Hartford, CT	https://www.arcgis.com/home/item.html?id=243947f01ac94e0193fff69b2f6b7090
9	i	Houston, TX (1)	RICE University GIS Department
10	j	Houston, TX (2)	
11	k	Los Angeles, CA (1)	
12	l	Los Angeles, CA (2)	http://egis3.lacounty.gov/dataportal/2011/04/28/countywide-building-outlines/
13	m	Los Angeles, CA (3)	
14	n	Louisville, KY	http://portal.louisvilleky.gov/dataset/buildings-data
15	o	New York, NY (1)	https://nycopendata.socrata.com/Housing-Development/Building-Footprints/xe92-xce7
16	p	New York, NY (2)	
17	q	Oklahoma City, OK	https://data.okc.gov/Portal/desktop/page/datasets
18	r	Philadelphia, PA (1)	http://opendataphilly.org/opendata/resource/6/
19	s	Philadelphia, PA (2)	
20	t	Seattle, WA (1)	https://data.seattle.gov/dataset/2009-Building-Outlines/y7u8-vad7
21	u	Seattle, WA (2)	
22	v	Washington, DC	http://data.dc.gov/Metadata.aspx?id=59

TABLE 2-2. Sources for GIS data obtained from GIS departments.

Since areas of buildings differ substantially between cities, we adopt a density criterion for selection of GIS samples:

$$\rho_{city}^{area} = \frac{\sum_{i=1}^{N} A_b^i}{A_{city}} \geq 0.1 \qquad [2.1]$$

where A_{city} is the total area of the sample with N buildings, while A_b^i is the ground area of building i in the sample of N buildings. Since urban boundaries and areas differ significantly between cities, in order to have an objective comparison, we have decided to only use buildings that are within the boundaries of a uniform shape and area. Therefore, for every temperature station located in a

city, we created circular buffers and extracted buildings for 22 cities in the US [Table 2-2], which we use in proceeding calculations. At first, it had been unclear what radius size of the buffer would be appropriate, but after conducting tests with different radii lengths (1, 3 and 5 miles) we decided that buffers with 3-mil radii would be optimal. This is because, on the one hand, radii sizes < 3-mil would not be able to provide us with statistically sufficient size samples for proceeding calculations; on the other hand, radii sizes >3-mil in vast majority of instance would extend beyond the actual city boundaries, or on occasions would interfere with the density criterion from Eq. (2.1).

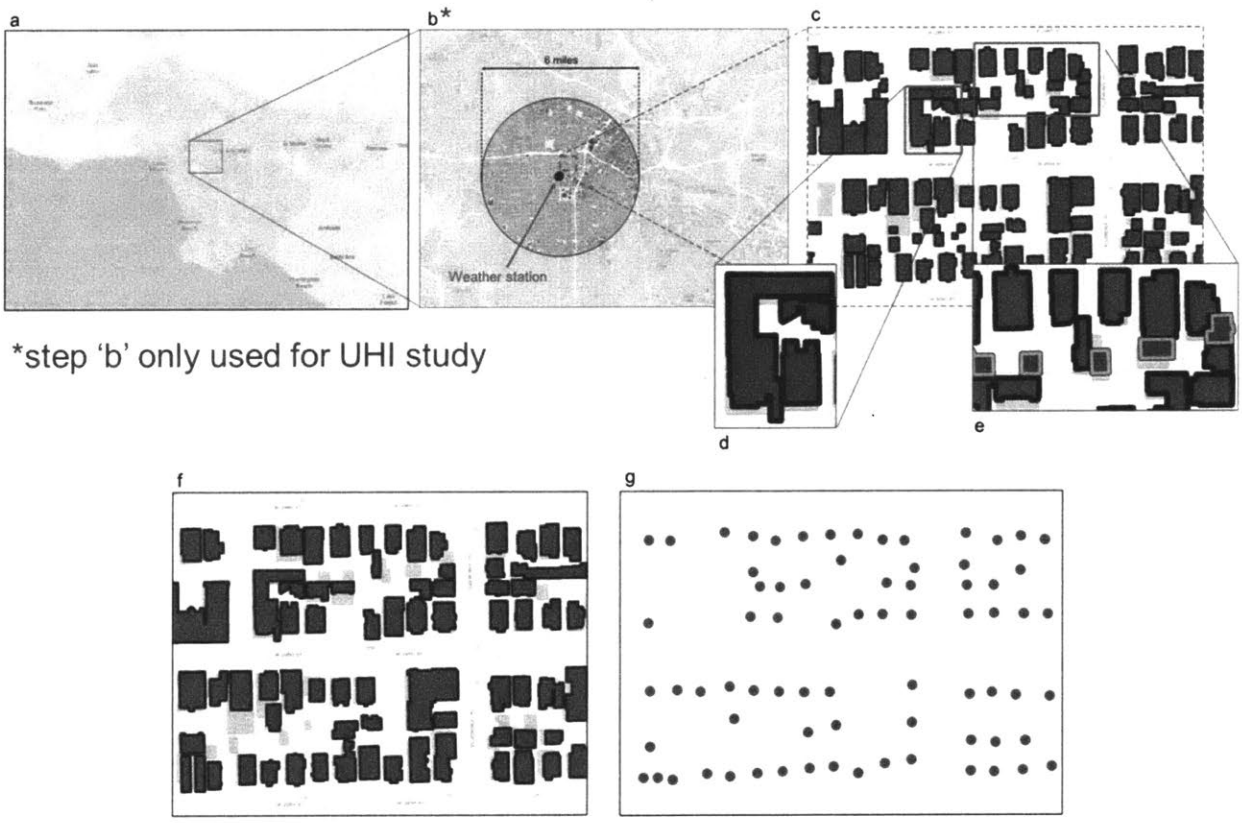

FIG. 2-1. Flowchart for extraction of GIS points from building footprints. The initial step to requires obtaining Geographical Information System (GIS) data with (a) 2D building footprints for a city. For each GIS file a local weather station is identified and a buffer of 3-mile radius is created around it (b) to extract buildings for further analysis (c). Any buildings that share a wall are merged (d) and any unoccupied buildings (ie garages), which make negligible contribution to energy heat transfer (e) are identified. Those unoccupied buildings are excluded from further analysis (f) and the remaining ones are transformed into single points (f) using buildings' centers of mass.

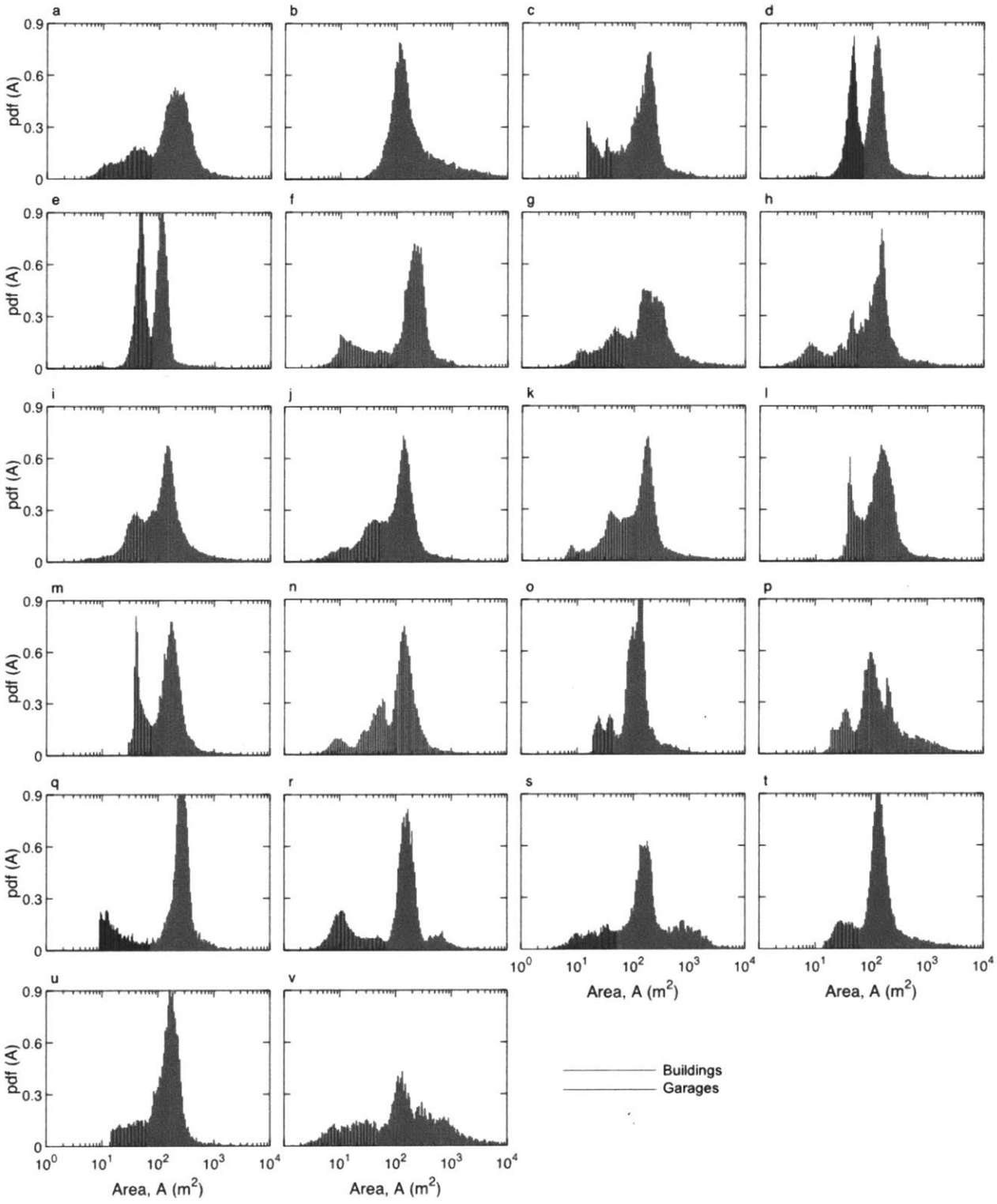

FIG. 2-2. Distributions of Areas of Buildings for GIS 3-mil cities.

To extract data for proceeding analyses, we adopt the following procedure, as visualized in Fig.2-1. To focus on the energy transfer between separated buildings or blocks, we merged all buildings sharing the same wall. We analyzed areas of merged buildings and found that in a logarithmic mode probability distribution function of buildings areas can be adequately captured with a bi-modal fit [Fig.2-2], which forms a clear distinction between unoccupied and occupied buildings, for instance garages and residential or commercial units, respectively. Unoccupied buildings are disregarded under the assumption that their contribution to the energy transfer between buildings is negligible, while the occupied buildings are represented by their two-dimensional center of mass.

2.4.1. OpenStreetMap (OSM) GIS Data

To analyze cities outside the US, we extend our data search to OpenStreetMap maps, which proves to be a most effective online platform choice, because it has no academic API restrictions, which allows researchers to freely download this type of data for any place in the world, assuming that mapping layers exist for that part of the world. The subsequent sections will explain how to download building footprints from OpenStreetMap and convert it to a format required for analysis in this study [Fig.2-1]. While different approaches may be used to obtain the same end results, here we adopt a city texture approach (*57*) by using the following software packages: QGIS, ArcGIS (licensed), Wambacher-osm, XAPI, Ubuntu, and MatLab (licensed).

Samples of data of spatial size 1000 x 1000m can be directly downloaded from OSM (www.openstreetmap.org/export) website. However, in order to be able to download data for an entire city, it is advisable to use XAPI server accessible using a terminal, which on most Windows platforms, it could be accessed using Ubuntu. The user must specify a rectangular region for data extraction using min and max GPS coordinates [bbox=Lon_{min}, Lat_{min}, Lon_{max}, Lat_{max}], which subsequently provides an OSM file, which later needs to be converted to an appropriate input file (shape file, .shp). QGIS software converts OSM file into buildings are stored as polygons. The shape file may contain other layers from the map, such as roads, landscape etc. However, each feature contains their unique tag. In the context of buildings, a Building Tag is used to mark a

given object as a building. Once buildings have been extracted, the user needs to identify buildings within a city's boundaries (which are never rectangular when downloaded as OSM from XAPI), which can be obtained from Wambacher-osm. Boundaries then are overlaid with polygons using either QGIS or ArcMap to extract the needed buildings. The next step, while optional, is advisable as it is going to offer in the proceeding steps an easier input for analysis; by converting GPS spherical coordinates of building footprints to a planar coordinate system in distance units (meters or feet), we can accurately depict areas of buildings and distances between them, without the need of using more time consuming algorithms to extract the same values using spherical degrees. The projection conversion depends on the geographical location and can be implemented using either QGIS or ArcMap conversion tools. After this step, to extract points representative of building footprints, we follow a similar procedure to the one we used to prepare GIS data from Table 2 [Fig.2-1].

Occasionally, buildings may have geometries stored for different parts of a building, which leads to overlaps and/or invalid polygons. To overcome this problem, we dissolve polygons (a tool in ArcMap) to create buildings with no inside geometries. In addition, this step allows us to merge any buildings that share a wall, which for the purposes of wind flow analysis is a necessary step. This is because in the context of wind flow, if we assume no change in building's properties, attached buildings can be considered to be a single structure. Before the final extraction of data, it is important to fill any voids inside polygons (which are the outcome of errors in the .osm data) so that it is possible to accurately quantify areas of buildings. This can be done directly with a "union" tool in ArcMap. With such defined .shp file, we can extract building footprints. The final step is conversion of buildings to points. Such conversion is completed using an ArcMap tool, which converts features to points. This tool creates a feature class containing points generated from the representative locations of input features and makes sure that the point is within the building's boundaries.

It is worth noting that building heights are available for some buildings in OSM data. The information for building height is either given by the number of levels (floors), or as a number depicting the actual height that includes the roof. This information is stored inside .shp file. However, for cities herein analyzed, it has been found that less than 5% of buildings have a positive

value attributed to the field signifying building height. While with time and increasing accuracy of OpenStreetMap data this value is very likely to increase, for the purposes of this study, <5% is inadequate to analyze building heights at the city level.

2.4.2. OSM GIS Data Validation

To validate the accuracy of OSM data, we introduce radial distribution function, $g(r)$ analysis and compare the results to results obtained using data obtained from cities' GIS departments. $g(r)$ is a probability density distribution, which captures the variation between a local density of buildings and the city's average. Here, we utilize the same data to juxtapose $g(r)$s using a sample of 3-mil radius cities [Fig.2-3] obtained from cities' GIS departments.

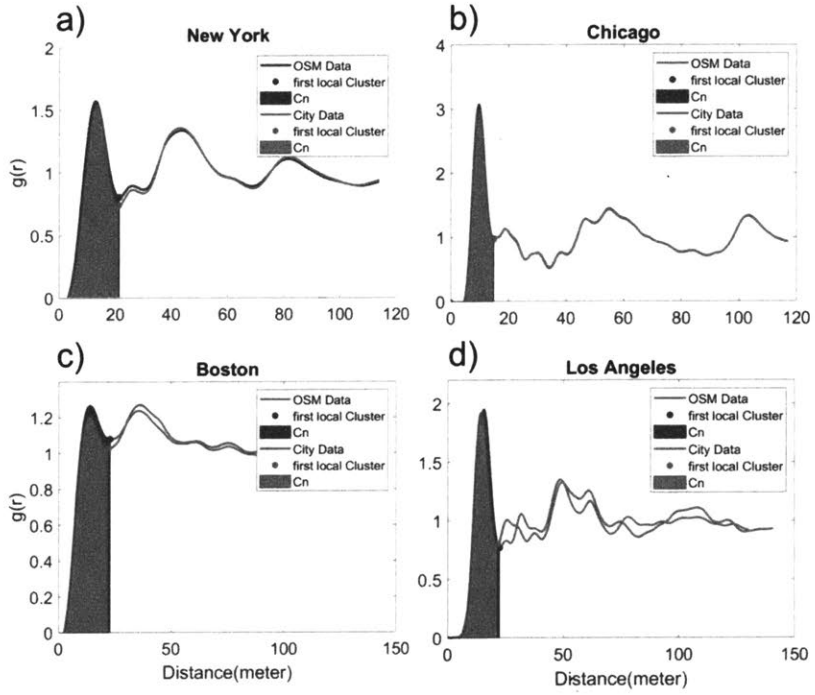

FIG.2-3. $g(r)$ distributions using OpenStreetMap and GIS data.

To quantify the error between OpenStreetMap and GIS data, we use a quadratic scoring rule that measures the average magnitude of the error, Root Mean Square Error ($RMSE$), using the following equation:

$$RMSE = \sqrt{\frac{1}{N}\sum_{i=1}^{N}\left(g(r)_i^{GIS} - g(r)_i^{OSM}\right)^2} \quad [2.2]$$

where, N = number of observations, $g(r)_i^{GIS}$ is $g(r)$ measurement obtained from GIS data, $g(r)_i^{OSM}$ is $g(r)$ measurement obtained from OpenStreetMap data.

In addition to $RMSE$, we also consider values derived from $g(r)$, which have been used to quantify city texture (*57*), namely distances associated with first peak $\left(R_{peak}^{g(r)}\right)$, and global minimum $\left(R_{min}^{g(r)}\right)$, average building size (L), local number of neighboring buildings (C_n), and order parameter (φ).

City	$RMSE$	$R_{min}^{g(r)}$ [m]	$R_{peak}^{g(r)}$ [m]	L [m]	φ	C_n
New York, NY	0.06	20.4 (20.8)	13.1 (12.4)	12.5 (11.4)	0.82 (0.44)	2.3 (2.4)
Chicago, IL	0.10	17.0 (14.2)	9.9 (9.4)	11.3 (11.7)	0.83 (0.50)	2.3 (2.0)
Boston, MA	0.12	20.4 (20.7)	14.7 (15.3)	11.3 (13.1)	0.63 (0.40)	2.7 (2.8)
Los Angeles, CA	0.19	21.2 (22.1)	14.8 (15.6)	13.4 (13.0)	0.70 (0.40)	2.3 (2.7)

Table 2-3. GIS and OSM Verification. Results showing differences between GIS and OSM results obtained using $g(r)$ analysis.

As $RMSE$ values in Table. 2-3 show for all four cities the error is relatively small. This suggests that in the context of $g(r)$, OSM data provides statistically similar results to GIS. Visualization of distributions in Fig.2-3 confirms that. To further validate the accuracy of OSM data, we compare other city texture characteristics. Except for order parameter, all values are very similar; OSM φ

values are generally lower, suggesting greater local disorder. This could be explained by the variation in $g(r)$ values, which are used as input for calculating φ. In addition, it is possible that the conversion from polygons to points would results in a slightly differ data for OSM. This is because in this study we made sure that in order to capture the most accurate location of each building, we used ArcMap's conversion tool that would make sure that each point is contained within the boundaries of a building. This is different approach to GIS data, for which points would be calculated using building's 2D center of mass. However, since majority of $g(r)$ characteristics of OSM data matches GIS data, we can confirm the validity of OpenStreetMap data acquisition.

2.4.3. OSM Cities

To understand how city texture changes across different parts of the world, we collected building footprints for major cities from different continents. However, since OSM data doesn't always provide the full extent of building footprints for a given city (building footprints may be nonexistent, especially in less economically developed countries), for OSM we adopt the same selection criterion as for GIS based on the density of buildings using Eq. (2-1). While many of the buildings have relatively small areas (i.e. garages), they remain relevant for wind flow simulations, where they might be most vulnerable structures exposed to a potential wind damage. Therefore, for OSM cities we choose to use all building in the proceeding analysis and identify 21 cities worldwide with unique city textures [Fig.2-4].

2.5. Population Change

We use population and average household size data (*134*, *135*) to estimate the total, as well as the urban number of households in each state. We convert estimated values of population for each year between 2005-2016, to urban (P_h^{urban}) and rural (P_h^{rural}) number of households by multiplying population values by appropriate urban/rural ratio and dividing it by an average household size (*135*).

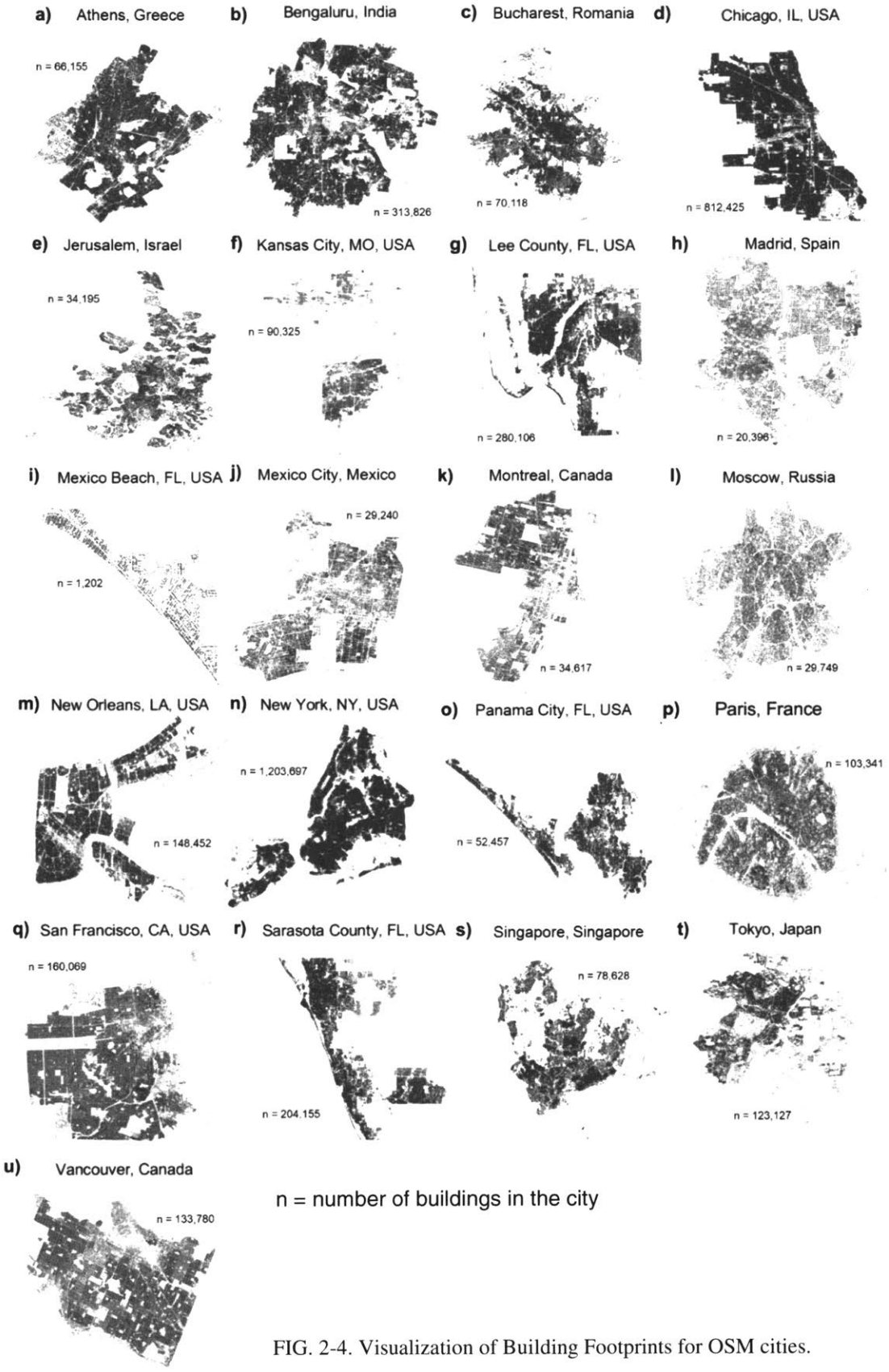

FIG. 2-4. Visualization of Building Footprints for OSM cities.

2.6. Summary

In this chapter we discussed data acquisition process required for the proceeding analyses. We presented two ways of extracting GIS data for building footprints using: online GIS databases and online mapping tools, with an example of OSM due to its user-friendly open licensing. We also showed sources for obtaining air temperature and building energy consumption data required for urban heat island and heat and cooling energy cost analysis. Lastly, we verified that OSM GIS approach, with the right limitations, provides an accurate, fast and easy method for downloading building footprints for any city in the world.

Chapter 3

3. Urban Physics: City Texture

This chapter begins with instituting the parallel between molecular physics and urban designs, an analogy which allows us to utilize tools typically seen being used only in the field of statistical physics. We explain analysis process needed to capture the unique city characteristics with just a few local city texture parameters. Next, we provide an approach for reconstruction of cities, which for the final part of this chapter, allows us to create samples of cities to be used in wind flow simulations.

3.1. Statistical Physics Approach for Texture Characterization

At the right scale, urban complexity becomes a hallmark of molecular structures that exhibits universal long- and short-range texture characteristics. Striking resemblance in texture between urban environments and molecular structure of polycrystalline material at an atomic scale is established with the help of appropriate visualization techniques. Techniques of this kind are widely used in identifying geometrical patterns in cities (*121, 122*). In such semblance, buildings are counterparts of atoms and neighborhood tesserae can be thought of as analogous to grain boundaries. To quantitatively explore this similitude, tools from statistical physics can be employed, which in a conventional sense are used to investigate the atom-scale structure of condensed matter. In order to extract statistical characteristics of short- and long- range city texture we employ radial distribution function, also known as pair correlation function. Oftentimes denoted by $g(r)$, it provides an isotropic homogenous picture of an anisotropic inhomogeneous medium by averaging the local density at time and space domains. In the context of cities and buildings, it can be thought of as a mechanism of describing density variation at a given distance from the reference building (represented by a point). As soon as local density deviates from the average density of a system, peaks in the distribution eventuate; in statistical particle physics terms applied to cities, this is explained as the probability of finding a building at distance r from the reference building relative to randomly distributed system of buildings that at long distance

converges to unity. In a closed system of homogenous particles, one would expect the average density of particles to be defined by the ratio between the number of particles and the area that they occupy. However, in the context of cities such approach may lead to an underestimation of density values, which would lead to an incorrect normalization of $g(r)$ and subsequently inaccurate values derived from it. This is because there may be regions within a city's boundaries, where buildings could not exist (i.e. water reservoirs). In addition, a variation in building sizes [Figs.2-2, 3-1] leads to further errors when calculating city average density values. On the contrary, in a random closed system of homogenous particles, points could in theory occupy any part of space and their size has no impact on density. Since this is not the case with cities, in order to quantify accurately average density of buildings, we utilize an average, ρ_{city}, from the distribution of density values as defined by:

$$\rho_{city} = exp\left(\frac{1}{N}\sum_{i=1}^{N} log\left(\frac{C_{n+1}^{R_{max}}}{\pi R_{max}^2}\right)\right) \quad [3.1]$$

where N is the total number of buildings, $C_{n+1}^{R_{max}}$ is the total number of buildings in circular area of radius R_{max}, which is the limiting radius for $g(r)$ analysis—distance at which g(r) convergences to unity—here defined to be $15L$ for OSM GIS building and $10L$ for GIS building, where L is the average building size for a city calculated using the following equation:

$$L = exp\left(\frac{1}{2N}\sum_{i=1}^{N} log(A_i)\right) \quad [3.2]$$

where N is the total number of buildings in the city and A_i is the area of building i. We find that similarly to 3-mil radius GIS samples, areas of OSM buildings follow a lognormal distribution [Fig.3-1]. However, for many cities outside the US, we identify much longer tails in city-wide distributions of areas, which is representative of the fact that in older cities there are more buildings with larger areas – indicative of terraced housing.

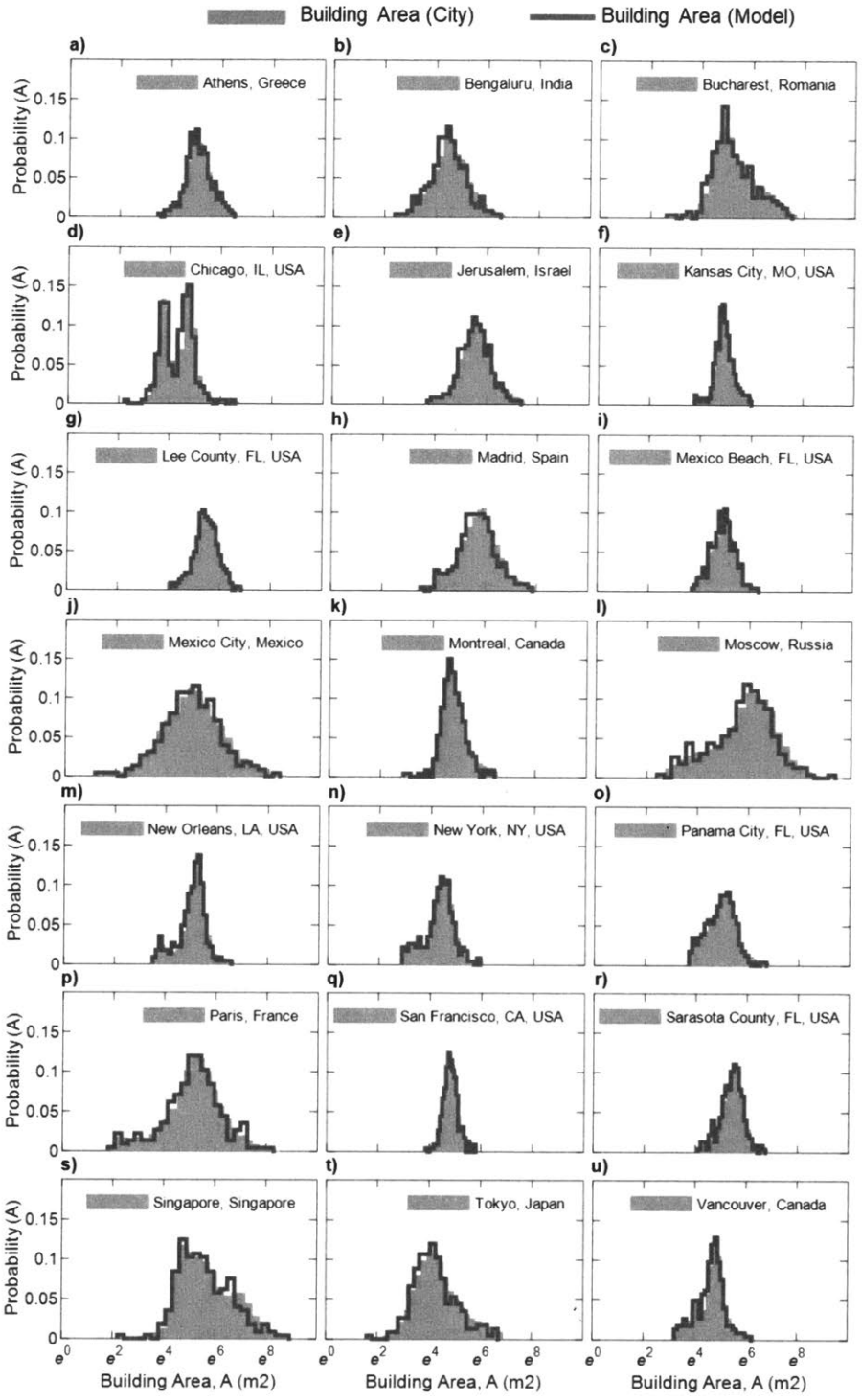

FIG.3-1. Building area probability distribution for OSM cities.

3.1.1. Radial Distribution Function, g(r)

Longer distance, R_{max} in $g(r)$ analysis for OSM buildings can be attributed to a greater local density variation before it is possible for the distribution to converge to unity. On the contrary for 3-mil radius GIS samples, there is a lower local deviation from the average density of the system. With such defined average density, $g(r)$ captures the local deviation from it in the following form:

$$g(r) = \frac{1}{N}\sum_{i=1}^{N} \frac{n_i(r+dr) - n_i(r)}{\rho_{city} 2\pi r \times dr} \quad [3.3]$$

where $n_i(r)$ denotes the number of buildings within the radial distance r from building i, and dr is distance increment, which for $g(r)$ calculations we chose to be 5% of the average building size, L:

$$dr = 0.05L \quad [3.4]$$

We found that 5% of the building size, as opposed to other percentage values, provides the optimal statistical richness in the $g(r)$ distribution; that is, lower values result in too much noise in the data, while higher values lead to too much smoothing and thus disguises the city texture form. In order to understand better the physical meaning of $g(r)$ for 22 GIS cities in the US [Table 2-2] and 21 OSM cities worldwide [Fig.2-4], we choose to create a set of idealistic cities based on regular and staggered grids [Fig.3-1]. We find that for disordered configurations resemble characteristics of most OSM cities, which suggests that most cities do not present a regular order in their city texture.

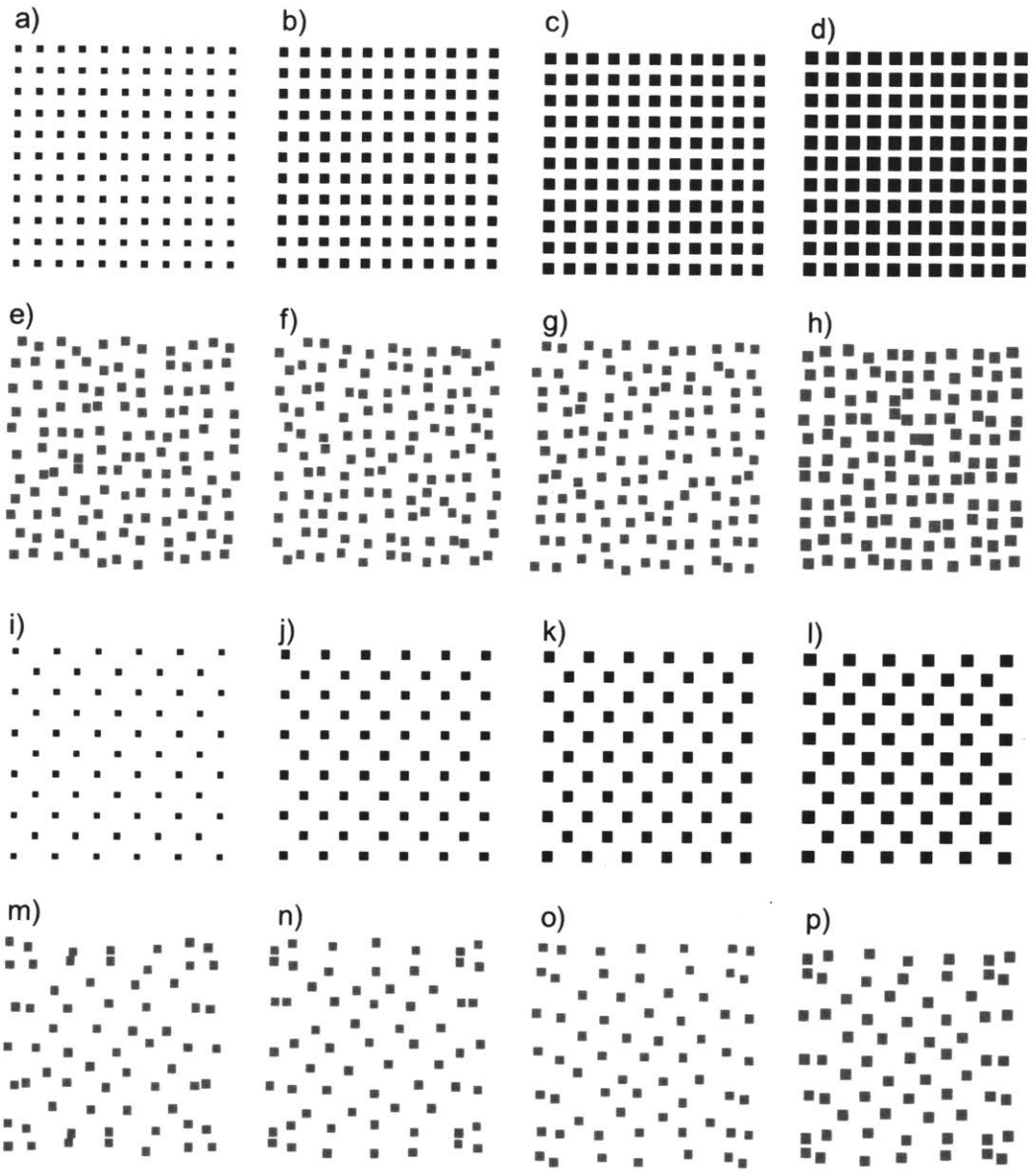

FIG.3-2. Ordered and disordered regular grid and staggered building samples.

In fig.3-3 $g(r)$s for idealistic configuration of buildings are visualized. Regular grid buildings of different densities have sharp and narrow peaks indicative the high order in the system. Similar behavior is observed in staggered grid buildings with the exception of wider distances between peaks, which are reflective of lower density of values. However, for the same density one can see that both configurations result in the same $g(r)$ [Figs.3-3.a,j,b,l]. As soon as disorder is introduced to the system and the local density begins to deviate from the average, both grid and staggered

configuration begin to look more like cities; specifically, wider and smoother peaks (in contrast to regularly ordered grid) of disordered grid configurations look similar to smooth and outspread peaks of Los Angeles, CA [Fig.3-4.k-m] resemble $g(r)$ of liquids whose particles present little structural order. Similar distributions are present in most GIS cities [Fig.3-4]. In turn, sharp and very distinctive peaks that characterize $g(r)$ of Chicago IL, New York NY, or San Francisco CA are the hallmark of highly ordered and stable crystalline materials. Although, for US cities we only identify crystal- and liquid-like textures, for many of the European cities, such as Paris in France, or Madrid in Spain, we find that $g(r)$ distributions are highly disordered with merely a single peak and a lack of local minimum, which are close of being gas-like distribution known to exhibit lack of peaks – that is local density is equal to average density.

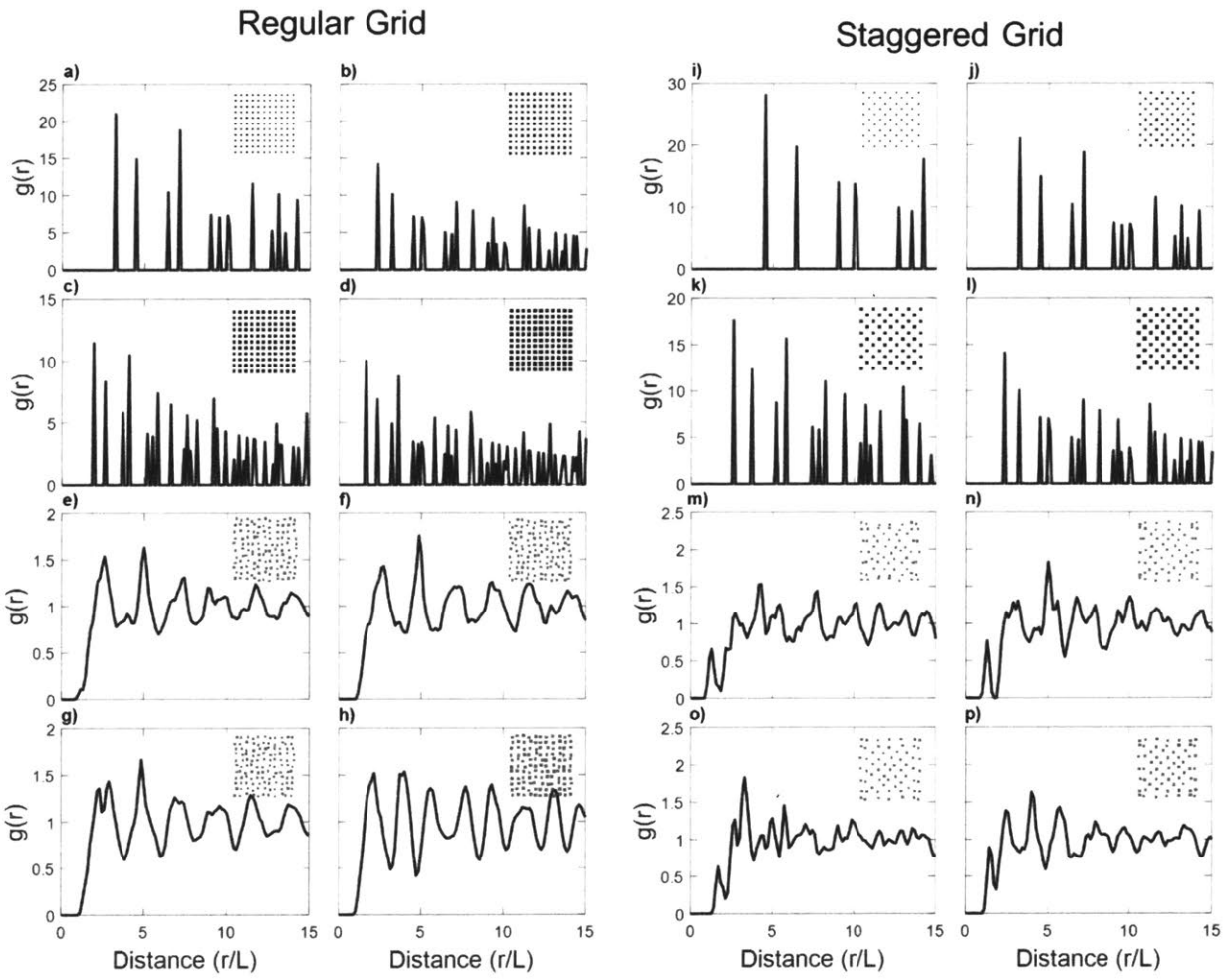

FIG.3-3.$g(r)$ distribution for grid and staggered samples.

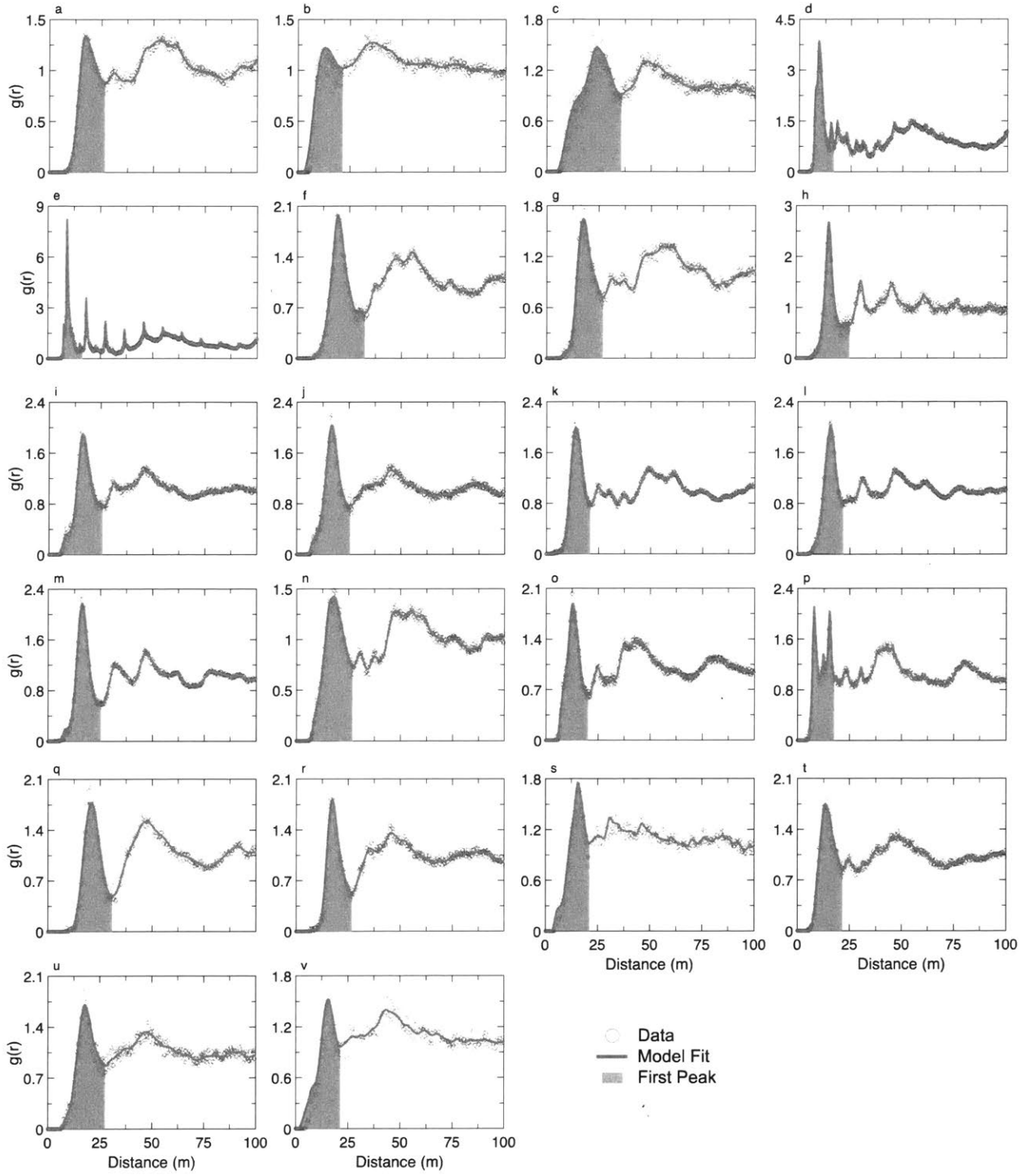

FIG.3-4. $g(r)$ distribution for GIS 3-mil cities.

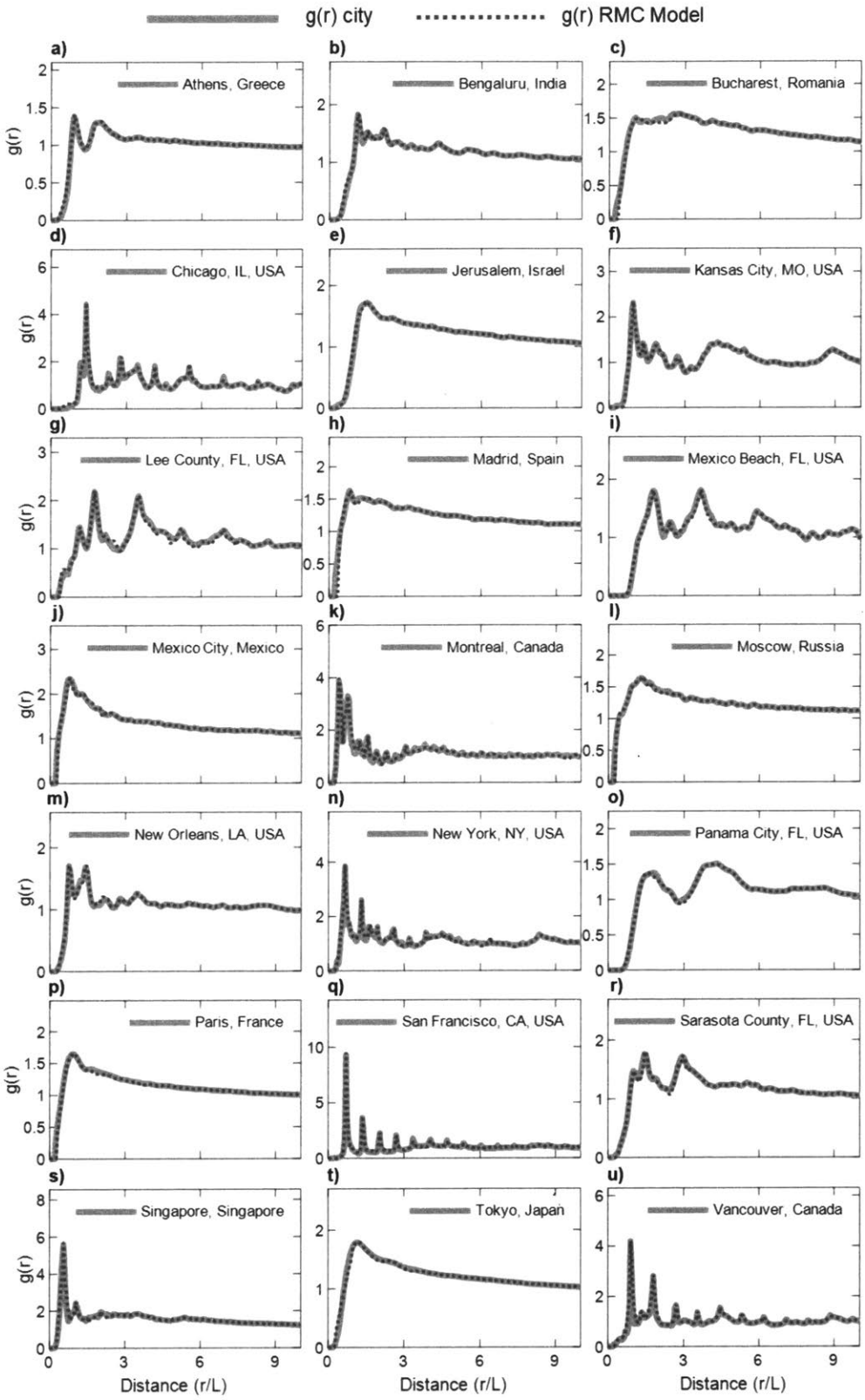

FIG.3-5. $g(r)$ distribution for GIS OSM cities.

We can conclude that much like molecular structures cities exhibit a distinct long-range texture, which varies from gas- and liquid- to crystal- like [Fig.3-6.a]. While others have argued that cities experience strong orders and patterns (*124*, *136*) vital for development and expansion (*125*, *127*, *138*), and mobility (*77*, *137*, *139*) as part of the process of smooth evolution (*115*), with our methodology we establish additional means for such categorization – by considering atomized buildings. We find that despite similar geographical location, distribution of buildings can exhibit different characteristics of local order [Fig.3-6.b].

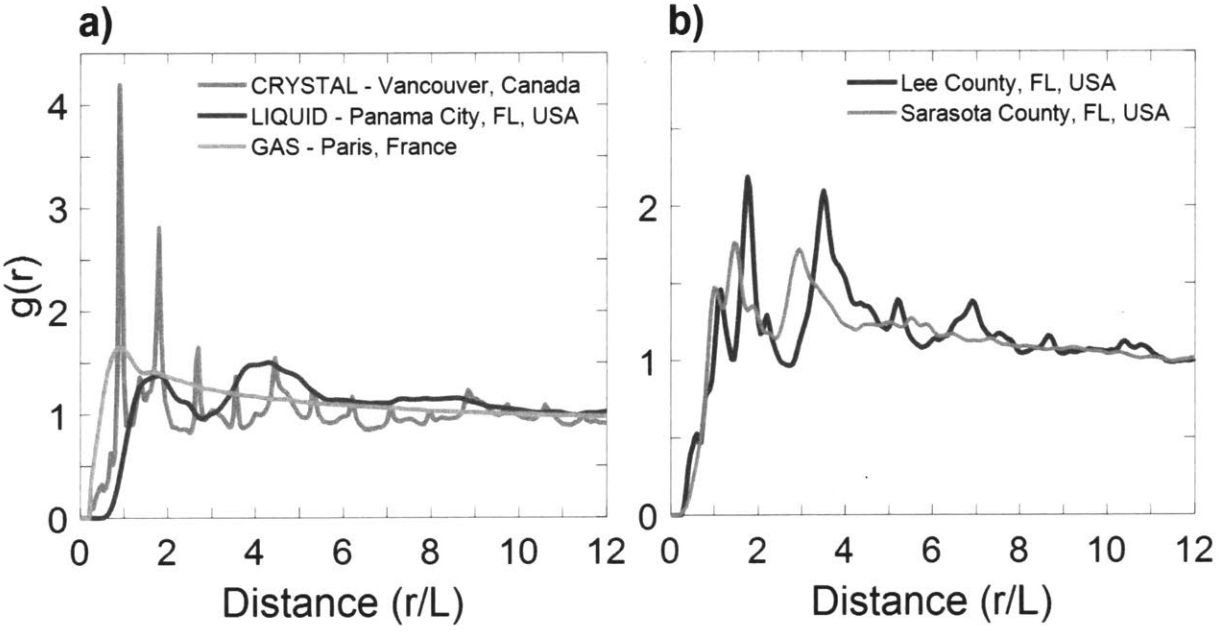

FIG.3-6.$g(r)$ comparison between cities with different city textures.

3.1.2. Local City Texture Parameters

To further quantify local texture patterns on the path of exploring meaningful ways of characterizing city texture, we employ two other quantities from the toolbox of statistical physics: 1) coordination number, $C_n^{g(r)}$, 2) average distance between local buildings, $R_{peak}^{g(r)}$, and 3) order parameter, φ. $C_n^{g(r)}$ is the number of nearest neighbors situated around the reference building. In the context of $g(r)$, it represents the area under the distribution, with the area under the first peak being representative of the first shell of neighboring buildings. Distance can be extended to derive

cumulative distribution of neighboring buildings to see that disordered configurations follow a smooth distribution, while for ordered configurations we see distinctive step increase for each $g(r)$ peak [Fig.3-7]. Applied to the two-dimensional city texture, distribution of neighboring building is generalized to:

$$C_n^{g(r)} = 2\pi\rho_{local}\int_0^{R_{min}^{g(r)}} r g(r)\, dr \qquad [3.5]$$

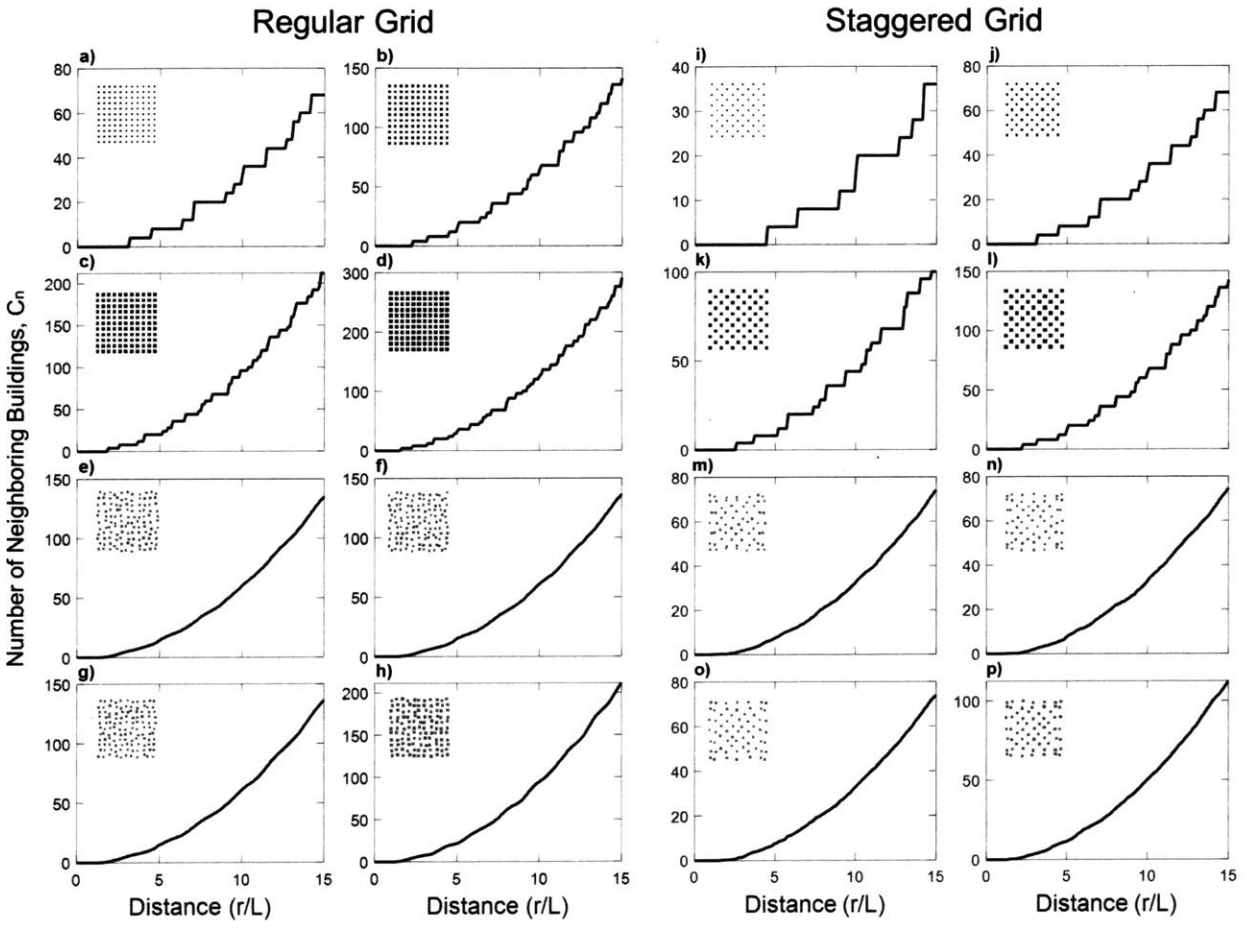

FIG.3-7.C_n distribution for grid and staggered samples.

With ρ_{local} being the local density of buildings in the circle defined by the radius, $R_{min}^{g(r)}$, which for the first shell of neighbors, is the distance where $g(r)$ reaches its first minimum, which in theory should also be a global minimum. In our analysis, however, this value does not always

befall as the global minimum. If, $C_n^{g(r)}$ obtained from the first local minimum is less than 1.5, we move onto the next minimum, until $C_n^{g(r)} \geq 1.5$ is obtained. Gas cities lack the expected $g(r)$ characteristics used to identify $C_n^{g(r)}$ and have no minima. For such cities, we must identify the distance, $R_{peak}^{g(r)}$ at which $g(r)$ reaches its first peak – a characteristic distance between one building and its nearest neighbors. This distance can be identified for all cities and correlates with $R_{min}^{g(r)}$ for cities where it is possible to identify it [Fig.3-8.a] and can be modeled using the following linear correlation:

$$R_{min}^{g(r)} = 1.35 \times R_{peak}^{g(r)} \quad [3.6]$$

Such linear correlation can be explained by the characteristic street width, which on average limits the local buildings to the nearest 2 neighbors [Fig.3-8.b]. Here, we wind that when combined with international cities, this scaling factor from Eq. (3.6) reduces from 1.5 (*57*) to 1.35 showing that street widths in the US are on average wider than for the rest of the world. With such approach, we can identify $R_{min}^{g(r)}$ for all cities, subsequently allowing us to derive coordination number for the first shell of neighbors. This is an important step, because distance $R_{min}^{g(r)}$ is a critical input for quantifying the local order parameter, φ.

The final local city texture parameter is the general Mermin 2D order parameter, designed in particle physics to quantify the deviation from symmetrical order of two-dimensional crystals with general close packing number m. Defined by:

$$\varphi_{local} = 1/N_a \left| \sum_{k=1}^{N_a} exp(im\vartheta_k) \right| \quad [3.7]$$

with m being the number of atoms in the first shell, we are looking for the m-fold orientation ordering, with N_a, the number of independent angles ϑ_k between the atom and its neighbors. For

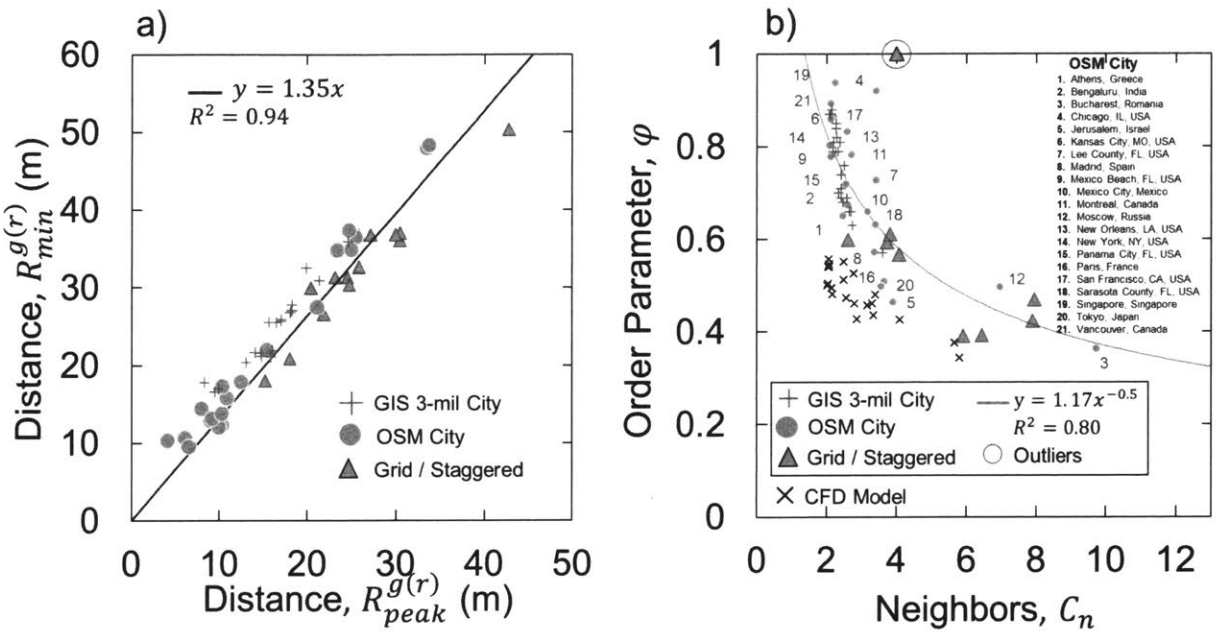

FIG.3-8. City Texture Parameters. a) Linear correlation between $R_{min}^{g(r)}$ and $R_{peak}^{g(r)}$. b) The correlation between order parameter and number of local neighbors for 21 cities obtained from OSM. CFD models and idealized grid/staggered cities are shown for comparison.

a perfectly ordered (symmetrical) system, $\varphi_{local} = 1$; and $\varphi_{local} = 0$ for a system with a perfect m-fold orientational ordering. Applied at the city scale, we utilize Mermin's two dimensional order parameter (*140*) to characterize the average angular distortion of buildings compared to a perfect angular order of a city at fixed $m = C_{N_a}$ with the first shell distance determined from $g(r)$. In the context of buildings, at the city scale order parameter, φ becomes:

$$\varphi = \frac{1}{N}\sum_{j=1}^{N}\frac{1}{N_a(j)}\left|\left(\sum_{k=1}^{N_a(j)} exp(iC_{N_a}\vartheta_k)\right)\right| \qquad [3.8]$$

where, N is the number of buildings and C_{N_a} is the actual number of neighboring buildings. So defined, φ = 1 represents a city in which all buildings at short distance have the same number of neighbors exhibiting angular periodicity, $2\pi/C_n^{g(r)}$; whereas any deviation from unity in this short-range city order parameter is representative of both local angular distortions of neighboring buildings, and local variations of number of neighbors that affects the number of independent

angles $N_a(j)$ for each building $j = 1, N$. Such approach aims at capturing short-range angular distortion at the city scale. The significance of our approach can be captured when plotting φ against C_n [Fig.3-8.b], which is calculated using the following equation:

$$C_n = \frac{1}{N}\sum_{i=1}^{N} C_{Na}^{i} \qquad [3.9]$$

where, N is the number of buildings and C_{Na}^{i} is the number of neighbors for building i. As shown in Fig.3-8.b, φ decays in a power form as city's coordination number, C_n, increases. The result is significant in several regards, starting from the observation that an increase in number of neighbors, at constant city density, is necessarily accompanied by a decrease in angular order, following $d\varphi/dC_n = -(A\,B)(C_n)^{-(B+1)}$, where A and B are power decay fitting parameters. Such relationships are abundant in statistical physics of the packing of particles close to jamming (*141*). With this analogous background in mind, we suggest that the correlation between φ and C_n provides further means of city categorization. Fixing values of C_n provides us with more effective grounds for comparison of cities' order; and establishes φ as a second texture parameter, defining a short-range order well distinct of long-range texture, or building density, or population size.

	City	$R_{peak}^{g(r)}$ [m]	$R_{min}^{g(r)}$ [m]	L [m]	C_n	φ
a	Regular Grid, $\lambda_p = 0.1$	30.4	36.1	9.5	4.00	1.00
b	Regular Grid, $\lambda_p = 0.2$	21.9	26.6	9.5	4.00	1.00
c	Regular Grid, $\lambda_p = 0.3$	18.1	20.9	9.5	4.00	1.00
d	Regular Grid, $\lambda_p = 0.4$	15.2	18.1	9.5	4.00	1.00
e	Regular Disordered Grid 1, $\lambda_p = 0.2$	24.5	31.4	9.5	5.90	0.39
f	Regular Disordered Grid 2, $\lambda_p = 0.2$	25.8	32.6	9.5	6.43	0.39
g	Regular Disordered Grid 3, $\lambda_p = 0.2$	27.2	36.8	9.5	7.90	0.42
h	Regular Disordered Grid 1, $\lambda_p = 0.3$	20.4	29.9	9.5	7.95	0.47
i	Staggered Grid, $\lambda_p = 0.05$	42.8	50.4	9.5	4.00	1.00
j	Staggered Grid, $\lambda_p = 0.1$	30.4	37.1	9.5	4.00	1.00
k	Staggered Grid, $\lambda_p = 0.15$	24.7	30.4	9.5	4.00	1.00
l	Staggered Grid, $\lambda_p = 0.2$	21.9	26.6	9.5	4.00	1.00
m	Staggered Disordered Grid 1, $\lambda_p = 0.1$	25.8	32.7	9.5	2.62	0.60
o	Staggered Disordered Grid 2, $\lambda_p = 0.1$	29.9	36.8	9.5	3.72	0.59
p	Staggered Disordered Grid 3, $\lambda_p = 0.1$	25.8	36.8	9.5	3.82	0.61
q	Stagerred Disordered Grid, $\lambda_p = 0.15$	23.1	31.4	9.5	4.06	0.57

Table 3-1. City Texture values for grid and staggered samples.

	City	ΔT_{u-r}[°C]	$R_{peak}^{g(r)}$ [m]	$R_{min}^{g(r)}$ [m]	L [m]	C_n	φ
1	Austin, TX	1.8	18.1	26.8	14.5	2.19	0.79
2	Boston, MA	2.7	14.7	21.6	11.3	2.74	0.63
3	Chesapeake, VA	1.7	24.6	35.9	12.1	3.60	0.57
4	Chicago, IL (1)	4.2	9.9	17	11.3	2.28	0.84
5	Chicago, IL (2)	3.5	9.5	16.6	10.9	2.14	0.88
6	Dallas, TX (1)	1.9	19.9	32.5	14.5	2.27	0.85
7	Dallas, TX (2)	1.9	18.3	27.1	14.6	2.25	0.79
8	Hartford, CT	2.6	15.6	25.5	11.8	2.41	0.74
9	Houston, TX (1)	2.1	17	25.9	12.1	2.70	0.66
10	Houston, TX (2)	2.7	17	25.7	11.5	2.65	0.66
11	Los Angeles, CA (1)	3.1	14.8	21.2	13.4	2.35	0.70
12	Los Angeles, CA (2)	2.9	16	21.9	13	2.47	0.68
13	Los Angeles, CA (3)	2.8	16.5	25.5	13.2	2.58	0.69
14	Luislouisville, KY	2.8	18.2	27.1	12.6	2.38	0.81
15	New York, NY (1)	3.8	13.1	20.4	12.5	2.29	0.82
16	New York, NY (2)	4.2	8.3	17.8	10.8	2.51	0.76
17	Oklahoma City, OK	1.4	21.3	30.9	15.8	2.08	0.87
18	Philadelphia, PA (1)	2.0	18.1	26.8	12.5	2.11	0.87
19	Philadelphia, PA (2)	3.0	15.8	21.1	13.9	2.33	0.79
20	Seattle, WA (1)	2.9	14.1	21.7	12.4	2.42	0.69
21	Seattle, WA (2)	2.0	18.3	27.8	12.6	2.42	0.71
22	Washington, DC	2.7	15.9	21.6	13.5	2.20	0.81

Table 3-2. City Texture values for GIS 3-mil cities.

		City	$R_{peak}^{g(r)}$ [m]	$R_{min}^{g(r)}$ [m]	L [m]	C_n	φ
1	a	Athens, Greece	10.9	15.8	12.9	2.44	0.65
2	b	Bengaluru, India	10.4	12.3	9.8	2.59	0.68
3	c	Bucharest, Romania	33.5	47.9	14.2	9.73	0.36
4	d	Chicago, IL, USA	9.4	12.8	9.0	3.41	0.92
5	e	Jerusalem, Israel	25.5	36.5	16.8	3.89	0.47
6	f	Kansas City, MO, USA	10.4	17.3	12.2	2.17	0.87
7	g	Lee County, FL, USA	24.7	37.4	15.9	3.41	0.73
8	h	Madrid, Spain	15.4	22.0	16.5	3.36	0.57
9	i	Mexico Beach, FL, USA	21.1	27.5	12.2	2.11	0.78
10	j	Mexico City, Mexico	9.0	12.9	10.4	3.17	0.66
11	k	Montreal, Canada	4.2	10.3	7.3	2.71	0.78
12	l	Moscow, Russia	33.8	48.3	18.2	6.95	0.50
13	m	New Orleans, LA, USA	10.0	12.0	9.3	2.57	0.83
14	o	New York, NY, USA	6.2	10.6	11.8	2.08	0.80
15	p	Panama City, FL, USA	23.4	34.8	12.9	2.54	0.72
16	q	Paris, France	12.5	17.9	11.4	3.64	0.51
17	r	San Francisco, CA, USA	25.0	34.9	11.8	2.11	0.86
18	s	Sarasota County, FL, USA	8.0	14.4	14.8	3.40	0.63
19	t	Singapore, Singapore	6.6	9.5	17.9	2.24	0.94
20	u	Tokyo, Japan	9.2	13.2	9.3	3.56	0.50
21	v	Vancouver, Canada	10.3	13.8	10.4	2.10	0.89

Table 3-3. City Texture values for GIS OSM cities.

3.2. Reverse Monte Carlo: Reconstruction of cities

By obtaining GIS data for any city in the world using online mapping tools and performing $g(r)$ analysis for entire cities, we established a method for quantifying city texture, which can be categorized to three distinctive groups: highly disordered gas-like, disordered liquid-like and ordered crystal-like cities. Thus far, these configurations and their local texture parameters have been correlated to the intensity of urban heat islands at nighttime (*57*, *142*, *143*). The main objective of this study, however, is to investigate the impact that city texture has on the flow of fluids with the ultimate objective to understand how it affects the pressure exerted on buildings in the environments of hurricane-like wind speeds. While, there have been models used to investigate the impact that different geometrical layouts have on drag coefficients (*94*, *103–105*, *109*, *110*), these models are limited to generic or idealistic, ordered structures, which are very different from configurations of buildings that exist in cities.

Two approaches used widely to quantify the impact of wind are wind tunnels and computational fluid dynamics simulations (*107*, *144*). Wind tunnel experiment, although is the most accurate approach to measure the impact that wind has on buildings, it is the most expensive approach. In additional, it is impractical as it requires a physical model of buildings to be built – this poses many problems when investigating the flow due to inability to quickly test any structural changes. However, since this is the most accurate approach, wind tunnel experiments are used to validate the accuracy of CFD experiments and might be used to test final design before implementing it in real life (*145*).

The complexity of networks and large quantity of the building stock in cities is a challenge that extends to CFD simulations, which require computational power that most organizations do not have access to in order to simulate flow for hundreds or even several thousands of buildings. In addition, to understand the impact that direction of the flow has, one would have to simulate flow in multiple directions (*144*, *146*, *147*), which would further increase the computational burden on the user. This creates the need for creating samples of cities that could be investigated in CFD experiments. To accomplish this task, we propose an approach based on recreating statistical characteristics of cities as captured by $g(r)$ using a Reverse Monte Carlo procedure.

3.2.1. Sample Size

Reverse Monte Carlo (RMC) procedure can be used to create realistic models of cities that could be tested in CFD simulations. RMC considers experimental constraints, herein namely $g(r)$, to construct a model that has statistical properties of a city. Density of the city, ρ_{city}, is used as an input parameter to define the area of the simulation box based on the number of particles used in the simulation. The more particles are used the more accurate the model is going to be. However, more particles would require a greater computational power and intensified time to run CDF simulations. On the contrary, a lower number of particles is going to reduce the accuracy of the RMC model. Therefore, it is imperative to identify optimal number of particles (*148*), a minimal quantity that would provide an RMC model, which can accurately reconstruct a system with 2-body interactions that have a unique link between the structure and the $g(r)$ function. Through trial and error, we have found this number of 225, which when accounting for the periodic boundary conditions [Fig.3-13], leads to a total number of particles equal to 2025. To begin the RMC procedure, 225 particles are randomly placed in a square box with the area, A_{model}:

$$A_{model} = 225/\rho_{city} \tag{3.10}$$

Then each of those particles is copied 8 times to be placed around the box in every direction to create the periodic boundary conditions. For such defined system $g(r)_{RMC}$ is calculated and compared to the $g(r)$ of the city.

3.2.2. Procedure of Error Minimization

To quantify the accuracy of the model a $g(r)$ root-mean square difference, $\chi^2_{g(r)}$ is calculated:

$$\chi^2_{g(r)} = \sum_{i=1}^{N} \frac{[g(r_i) - g(r_i)_{RMC}]^2}{\sigma(r_i)^2_{RMC}} \tag{3.11}$$

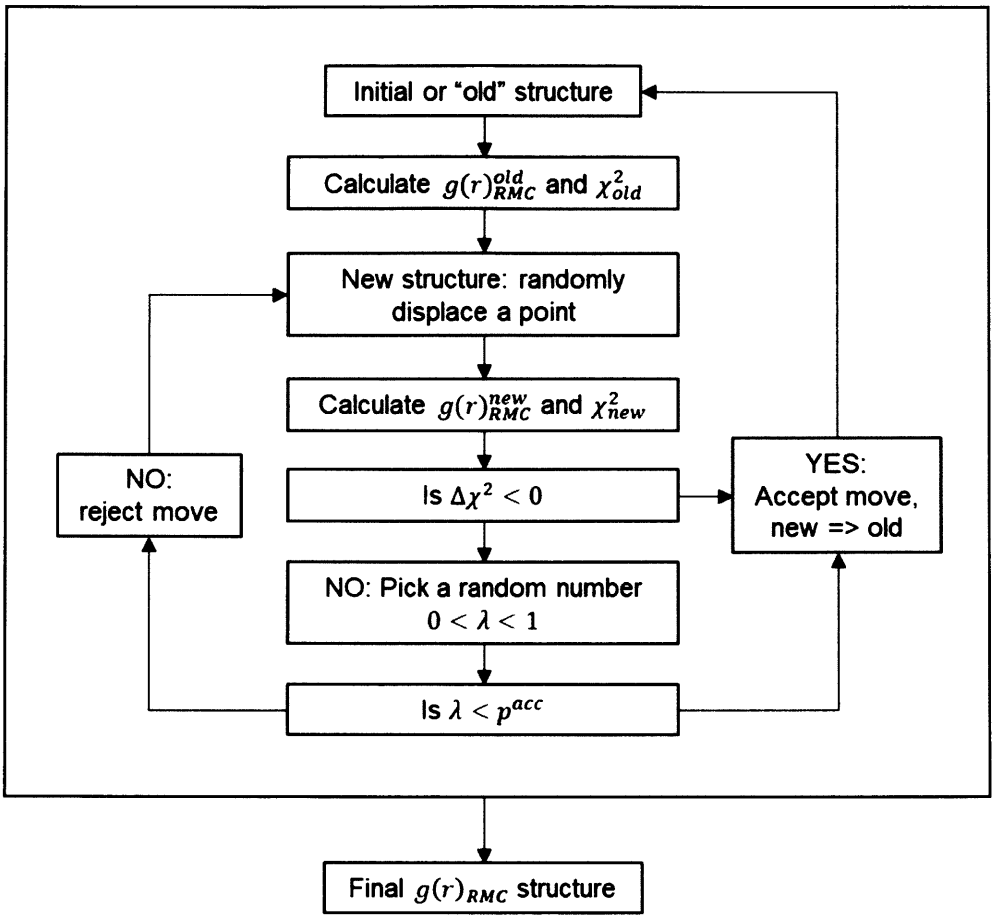

FIG.3-9. Flowchart for Reverse Monte Carlo (RMC) procedure.

where, N is the number of points, i used to derive both $g(r)$ functions, and σ is the experimental (RMC) error. The next steps, as shown in the flowchart in [Fig.3-9] are followed to identify a model with minimal χ^2. The first step is to randomly pick one from 225 particles and replace it (together with 8 surrounding particles) with a particle placed in a random position within the boundaries of the box to calculate χ^2_{new}. However, since $g(r)$ structure can have many unique configurations of local parameters, like C_n or φ, it is important to also account for these local distributions when reconstructing the city. We choose to incorporate another error parameter, $\chi^2_{C_n}$, obtained from the distribution of the first shell of neighbors:

$$\chi^2_{C_n} = \sum_{i=1}^{N} \frac{\left[pdf(C_n^i) - pdf(C_n^i)_{RMC}\right]^2}{\sigma(C_n^i)^2_{RMC}} \qquad [3.12]$$

where, N is the number of points, i used to derive both probability density function (pdf) of local neighboring buildings C_n defined by $R_{min}^{g(r)}$ for the city. The second local parameter, φ, is left to be used later to validate the model. During an RMC simulation, in order to identify if the new configuration should be accepted or rejected, we calculate to total root-mean square error difference, $\Delta\chi^2$, between old and new configurations:

$$\Delta\chi^2 = \left(\chi^2_{g(r),new} - \chi^2_{g(r),old}\right) + \left(\chi^2_{C_n,new} - \chi^2_{C_n,old}\right) \quad [3.13]$$

When $\Delta\chi^2 < 0$, a new configuration is always accepted. But, when $\Delta\chi^2 \geq 0$, we introduce weighing parameters, which may result in either acceptance or rejection of the new configuration (*149*). This is done to ensure that the final structure is independent of the initial configuration. Also, such approach allows us to explore a large set of different configurations (*150*). First, we test a single weighing parameter, T_x, so that when $\Delta\chi^2 \geq 0$, a new configuration is accepted with the probability:

$$p^{acc}_{old\rightarrow new} = min[1, exp(-T_x \times \Delta\chi^2)] \quad [3.14]$$

3.2.3. Model Weighing Parameters

We have explored a range of different T_x values and found that $\Delta\chi^2$ decreases as T_x increases [Fig.3-10.a]. However, as T_x gets large (i.e. >20) the number of accepted configurations decreases. This creates a challenge because there is not enough variability in configurations with low χ^2 values and thus, identifying an RMC model with φ distribution matching one of the city becomes not possible. Therefore, to identify a large set of RMC models with low χ^2 values, we set $T_x = 10$. However, since there are two error parameters involved in the probability acceptance criterion, we choose to investigate two additional weighing parameters (*149*), T_1 and T_2 so that a new configuration is accepted with the probability:

$$p_{old\to new}^{acc} = min\left[1, exp\left(-T_x \times \left(T_1 \Delta\chi^2_{g(r)} + T_2 \Delta\chi^2_{C_n}\right)\right)\right]$$

[3.15]

We have investigated different values for both T_1 and T_2 [Fig.3-10.b] and established that the optimal configuration for weighing parameters is: $T_x = 10, T_1 = 2$, and $T_2 = 3$.

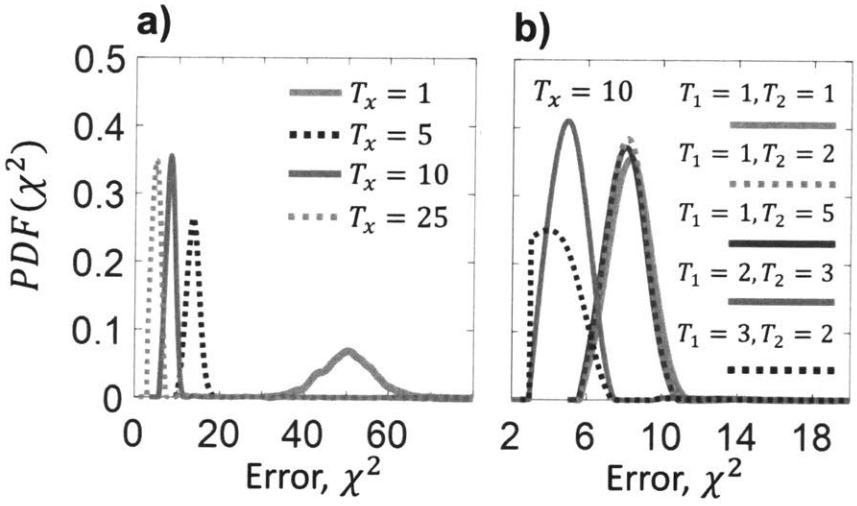

FIG.3-10. RMC Weighing Parameters. Probability density function distributions for RMC models with a varying values of a) single weighing parameter T_x and b) three weighing parameters T_1, T_2 and $T_x = 10$.

3.2.4. Validation

With such defined steps and parameters for RMC simulation, we reconstruct samples for 21 cities [Fig.3-13]. We find that in order to be able to have a large set of samples with low χ^2 values, one should generate establish an RMC simulation with at least 0.5×10^6 steps; but to identify convergence in χ^2 values for all samples we needed 1×10^6 steps. As Fig.3-11 shows, initial values for $g(r)$, C_n and φ distributions for two RMC samples are very similar, which confirms a random arrangement of particles. However, for final configuration, it is clear that RMC models resemble those of cities, whether it is crystalline structure of San Francisco, CA or gas-like structure for Paris, France. In the context of reconstruction of $g(r)$, RMC simulations at the point

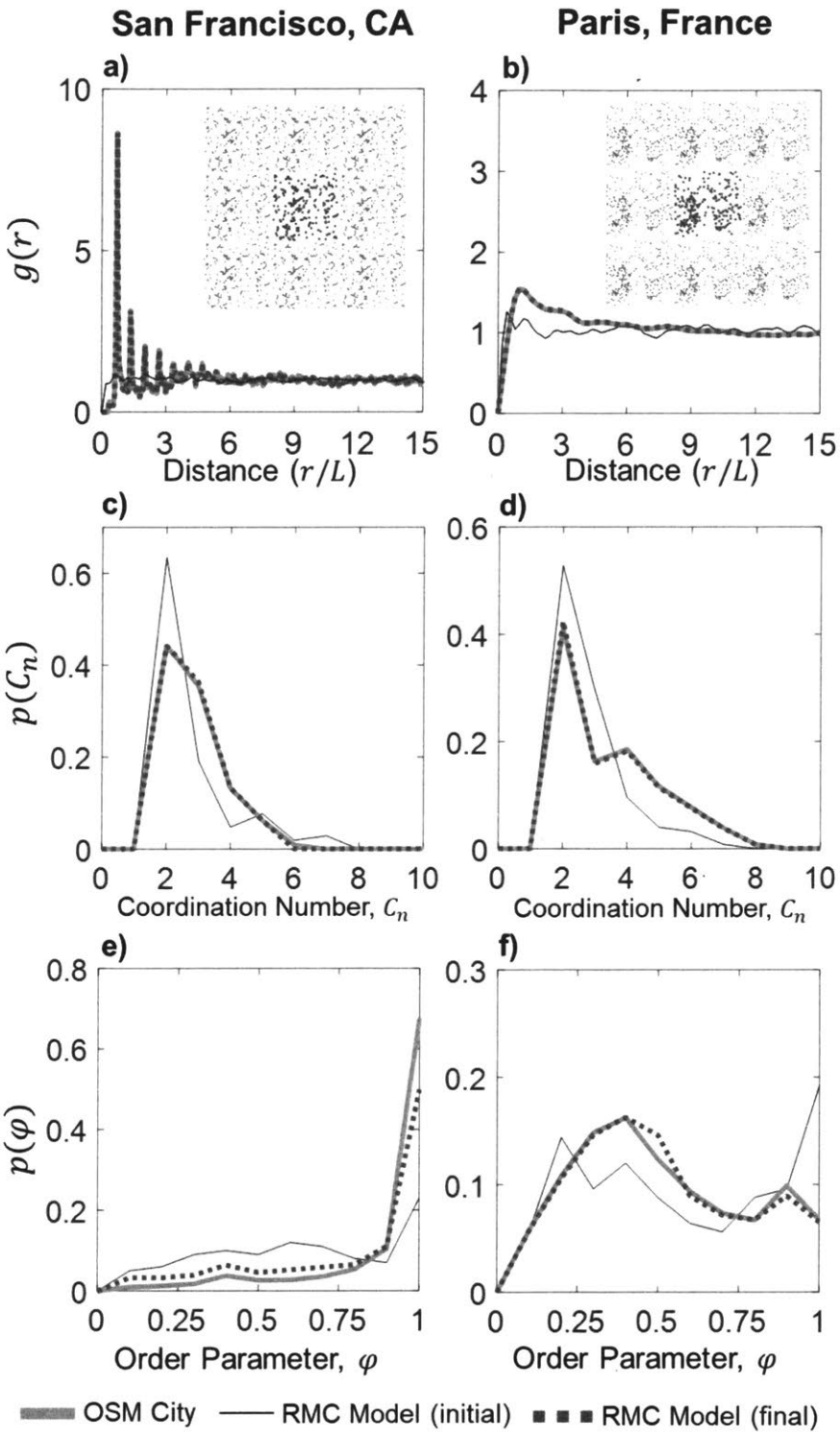

FIG.3-11. Comparison of OSM and RMC data. OSM city texture values and results of RMC simulations for $g(r)$ with final RMC configurations (inlets) for a) San Francisco, CA and b) Paris, France; probability distributions of C_n for c) San Francisco, CA and d) Paris, France; probability distributions of φ for e) San Francisco, CA and f) Paris, France.

of minimum error are expected to reach the state of maximum entropy (*151–153*), which translates to maximum disorder for the configuration of particles. This type of configuration would not result in a realistic configuration of cities, which are known to have their order decay with an increasing number of neighboring buildings [Fig.3-8.a] resulting in a lower entropy than the minimization of χ^2 errors would lead to. Therefore, to account for the right order of local neighbors, we resort to an approach where we identify a probability distribution of φ for the RMC model that most closely resembles the probability distribution of φ for an OSM city, that is the root-mean-square error between two distribution is minimal. To do so, from all possible configurations obtained during the RMC simulation, we identify the lowest 1% of χ^2 distribution, which allows us to identify textures with the lowest root-mean square differences for RMC and OSM city φ distributions. We find that as χ^2 converges, the variation in χ^2_φ also becomes minimal; we select a distribution with the lowest error, which we find resembles accurately overall distributions of $g(r)$, C_n and φ [Fig.3-11] for cities of different textures, whether gas, liquid or crystal.

3.3. Computational Fluid Dynamics Models of Cities

We have established a method for reconstructing statistical samples of cities, with points representing buildings. To be able to test these samples in wind flow experiments, we need to recreate buildings that are representative of OSM cities. Using RMC points, we establish central points around which we create building footprints using probability distribution of building areas from OSM cities [Fig.3-1], to create areas of buildings for 225 points from RMC models. We randomly assign building areas to RMC points to create square building footprints, so that each RMC building has the following x_i and y_i coordinates for building i:

$$x_i = \left[\frac{L_i}{2} - x_{i,c}, \frac{L_i}{2} + x_{i,c}, \frac{L_i}{2} + x_{i,c}, \frac{L_i}{2} - x_{i,c}\right]$$

$$y_i = \left[\frac{L_i}{2} - y_{i,c}, \frac{L_i}{2} - y_{i,c}, \frac{L_i}{2} + y_{i,c}, \frac{L_i}{2} + y_{i,c}\right] \quad [3.16]$$

where, L_i is the average building size derived from the probability distribution of areas of OSM buildings, and $x_{i,c}$, $y_{i,c}$ are x, y coordinates for RMC samples. However, random assignment of areas may result in building overlapping, which we try to minimize. If there is an overlap, we switch areas between two buildings. However, with a sample of 225 buildings and areas of buildings ranging from 3 to as much as 100m, sometimes it is not possible to prevent overlaps. However, since we identify that there are less than 20% in overlaps, we choose to accept the best possible configurations, given the above constraints.

In order to prepare samples for CFD simulations, we must assign heights to buildings. Since, we lack information about heights of buildings, we choose a fixed height, H of 9.5m, which is an average height representative of residential buildings (*57*). Thus, all buildings in our samples have the same height. In addition, to avoid issues with meshing configurations, we merge any building that are separated by a distance of 1m or less. Considering such distance translates to a very low ratio between width to building height, which in the context of our study, due to a high skimming flow (*102*, *106*) can be neglected for the purposes of hurricane flow simulations for samples with average building sizes of >10m. Because of that we merge such buildings, which in some cases would reduce the number of buildings by 50%. This creates a challenge because, if we re-calculate city texture parameters for CFD building configurations with significantly lower number of points, when compared to RMC samples, we find that $g(r)_{CFD}$s, although follow the trend of $g(r)$ for OSM cities, they do not match their unique patterns [Fig.3-14]. In addition, merging of buildings leads to a variability in the distribution of building areas that is different to the distribution of the initially assigned building sizes [Fig.3-12]. In the end, although derived using RMC samples that resemble explicitly texture of OSM cities, CFD models do not. Therefore, for the purposes of the CFD simulations, these 21 samples are treated as unique disordered configurations of buildings, as opposed to reconstructed cities.

To increase the testing sample and to understand better validity (and physical meaning) of the 21 disordered configurations of buildings, we prepare an additional set of CFD samples using the set of previously introduced idealistic cities based on regular and staggered grids [Fig.3-2]. For these models, we choose building size based on the fixed height of 9.5m, so that $L = H = W$, where W

is building's width. With such size, we create samples of varied densities, which resemble previously studied configurations using wind tunnel and CFD experiments.

As a final step, to minimize the effects of city texture at the boundaries of CFD samples, we create periodic boundary conditions for each sample of buildings by adding 2 rows of buildings for each side of the sample, which is done in a similar manner to periodic boundary conditions RMC. The approach is exemplified in the middle column of Fig.3-13. Similar periodic boundary approach is utilized for the additional 16 grid and staggered configurations.

3.4. Summary

In this chapter we established an approach that allows us to quantify city texture for any city in the world. In addition, we developed a model for reconstructing of cities using samples that have a very low number of buildings, when compared to real city. Samples of this size allow us to study the impact of city texture in computationally expensive wind flow simulations.

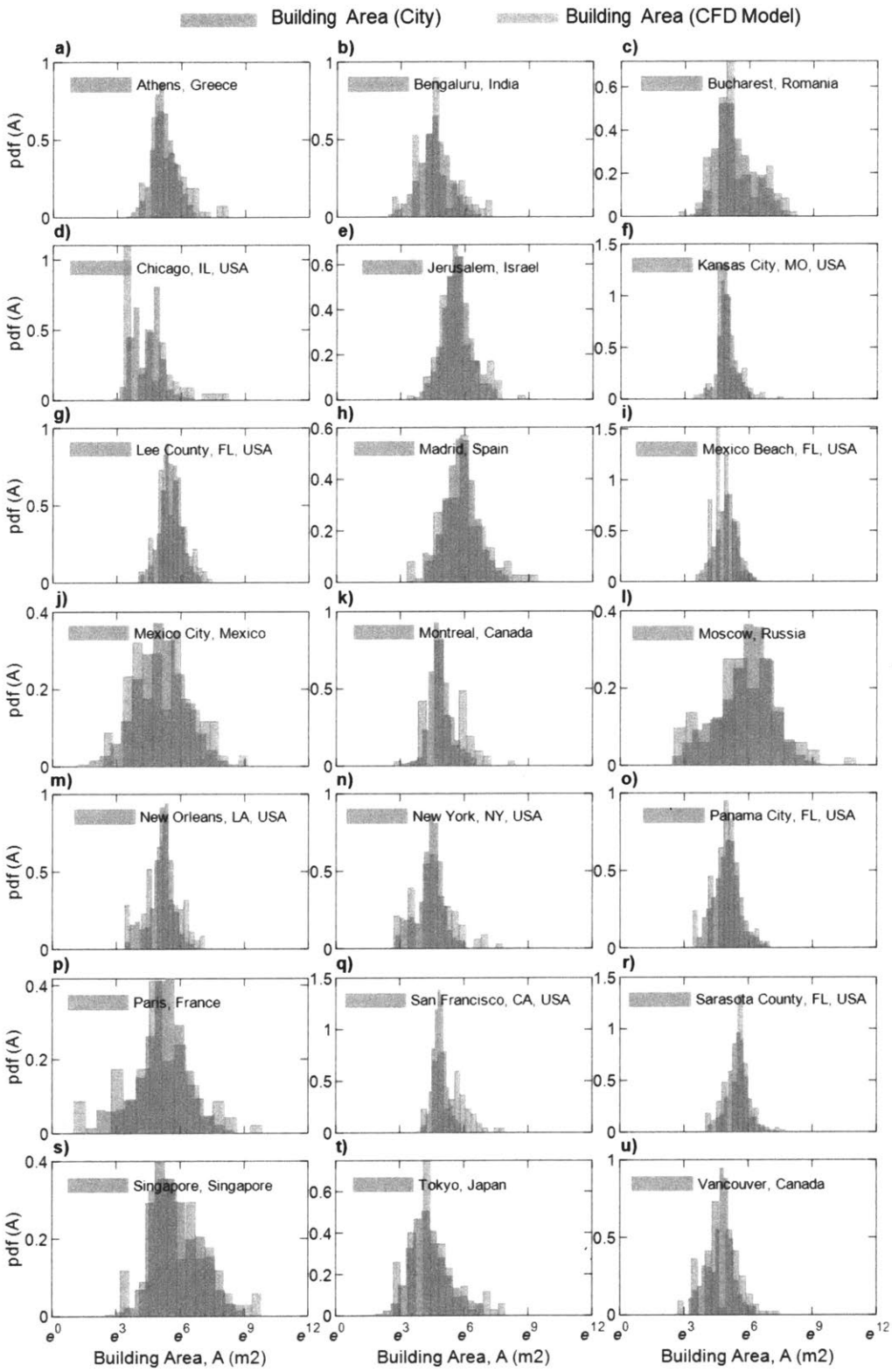

FIG.3-12. Building area probability distribution for CFD samples.

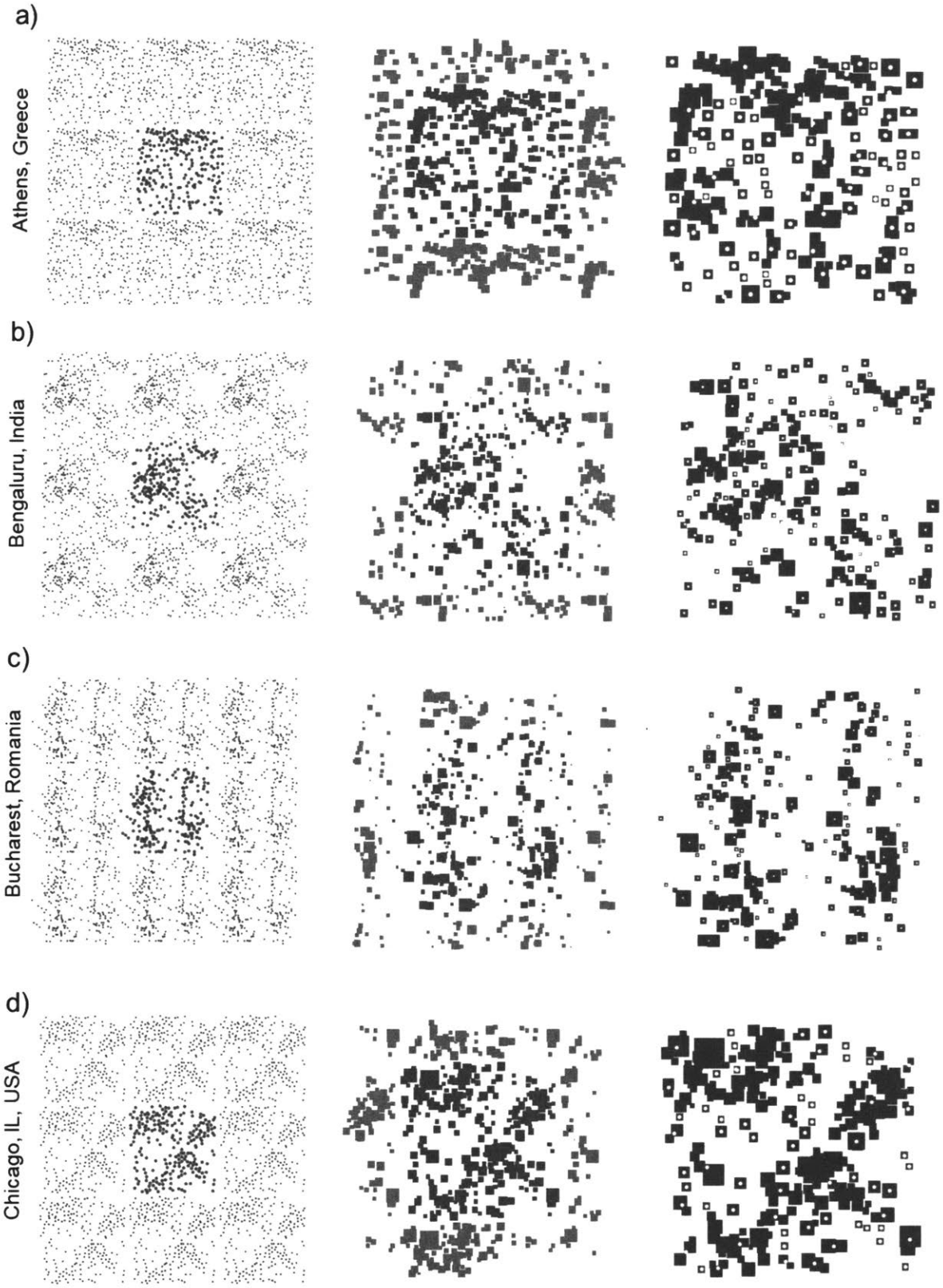
a)
Athens, Greece
b)
Bengaluru, India
c)
Bucharest, Romania
d)
Chicago, IL, USA

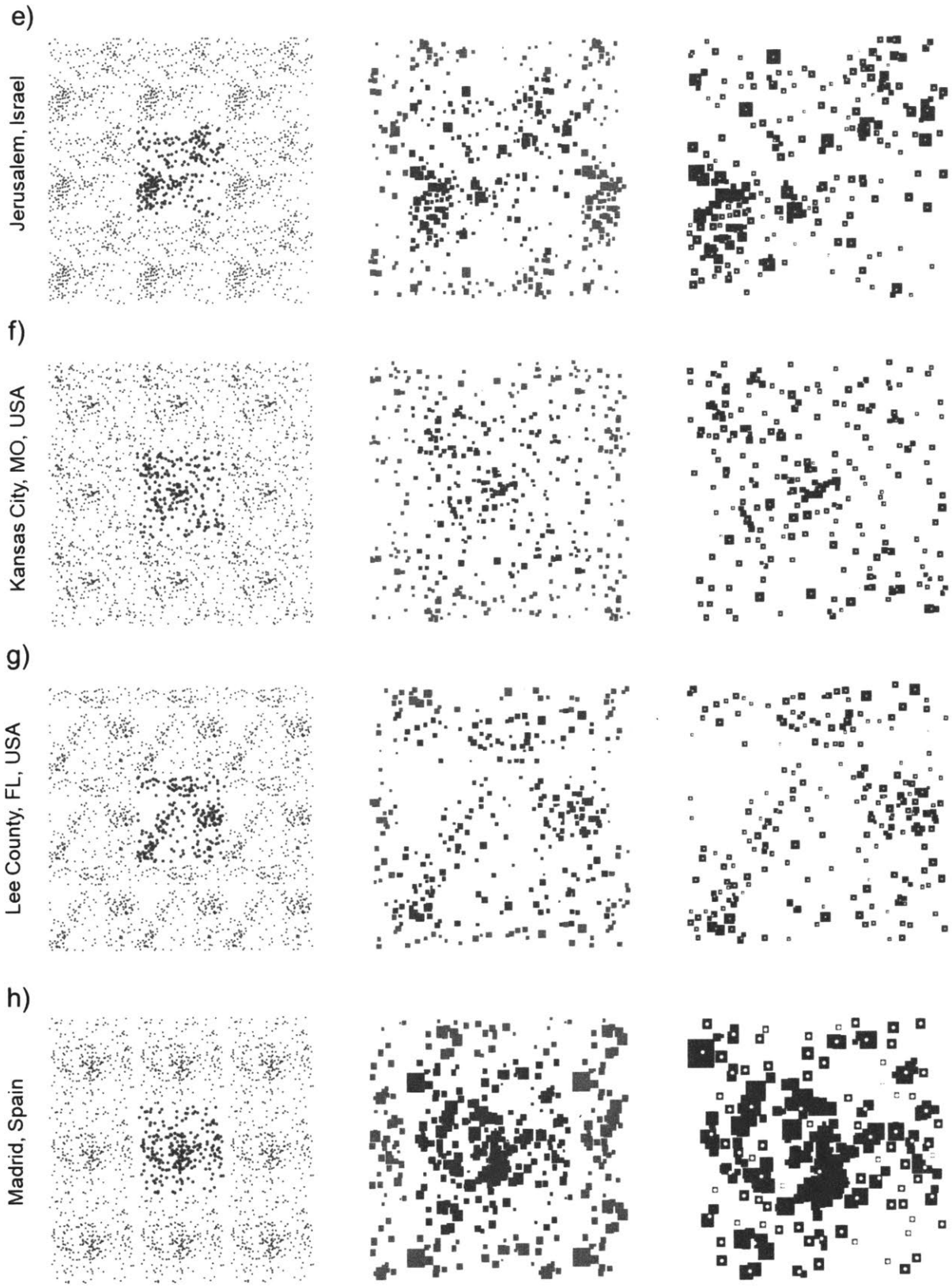
e)
Jerusalem, Israel
f)
Kansas City, MO, USA
g)
Lee County, FL, USA
h)
Madrid, Spain

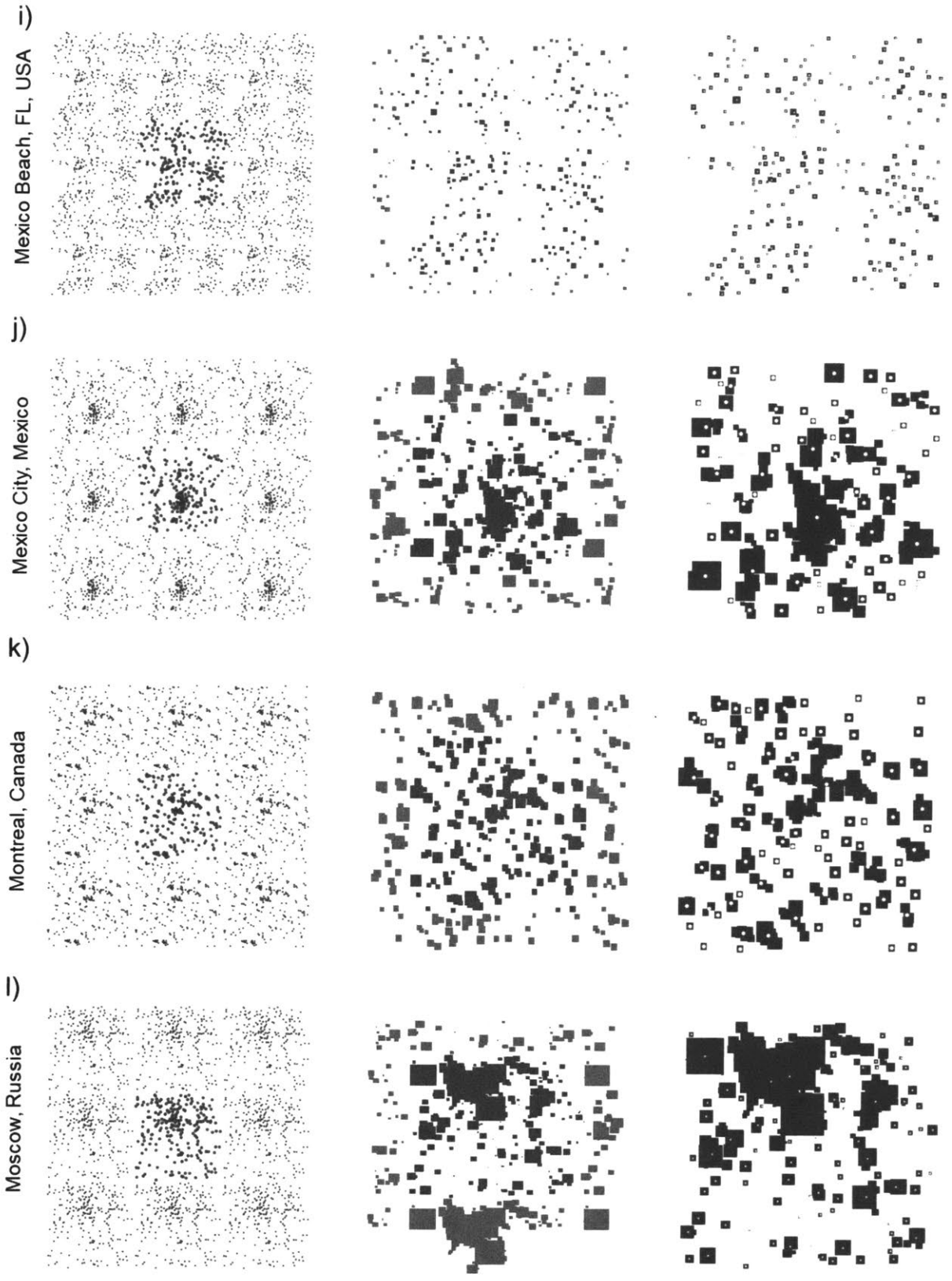
i)
Mexico Beach, FL, USA
j)
Mexico City, Mexico
k)
Montreal, Canada
l)
Moscow, Russia

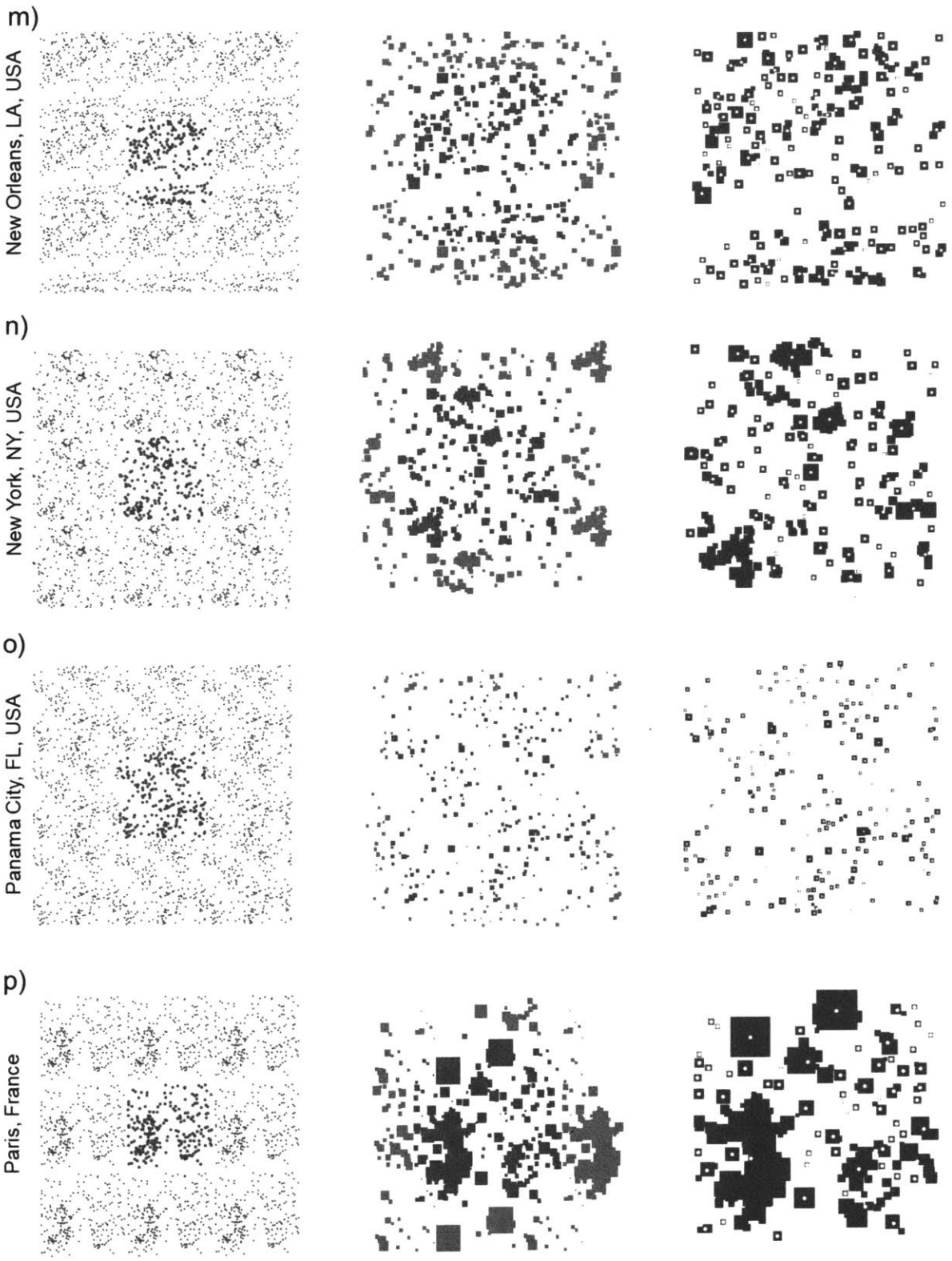
m)
New Orleans, LA, USA
n)
New York, NY, USA
o)
Panama City, FL, USA
p)
Paris, France

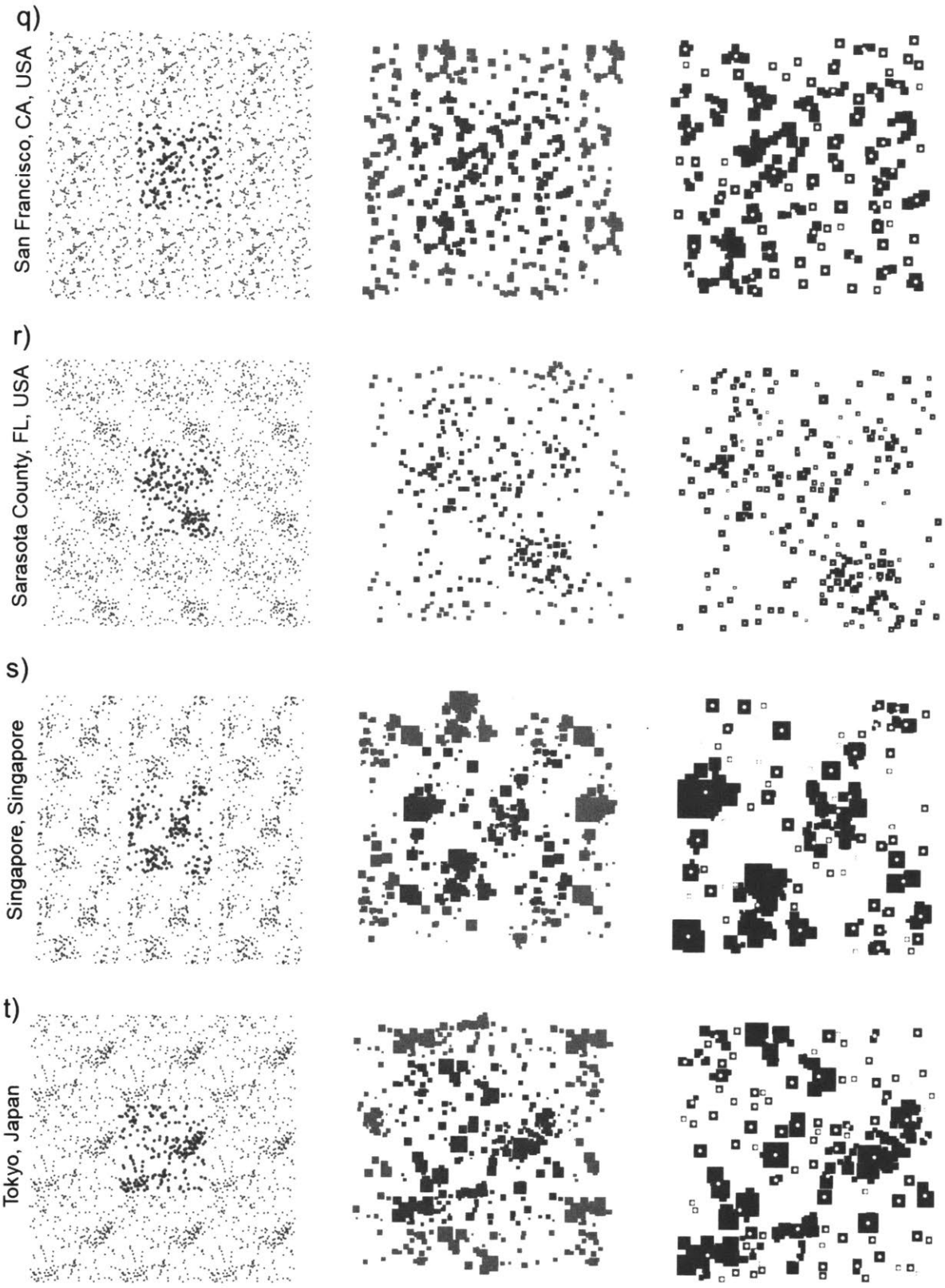
q)
San Francisco, CA, USA
r)
Sarasota County, FL, USA
s)
Singapore, Singapore
t)
Tokyo, Japan

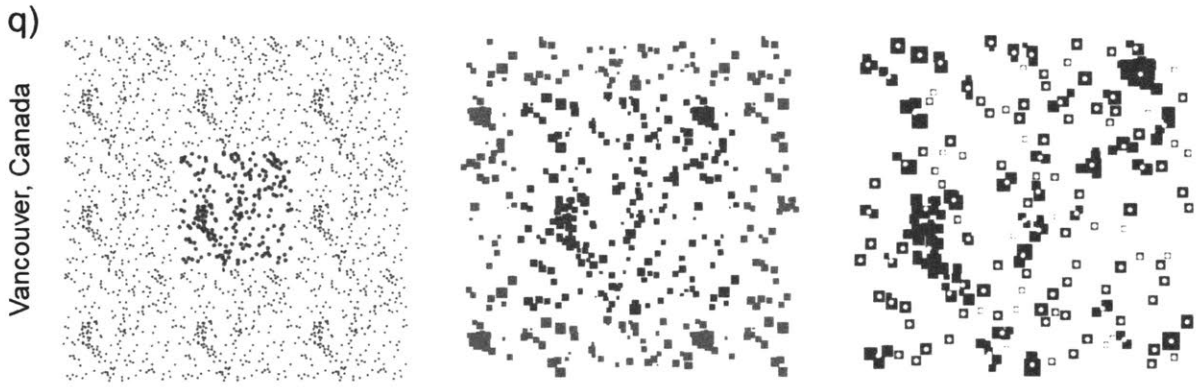

FIG.3-13. Reconstructed city CFD samples.

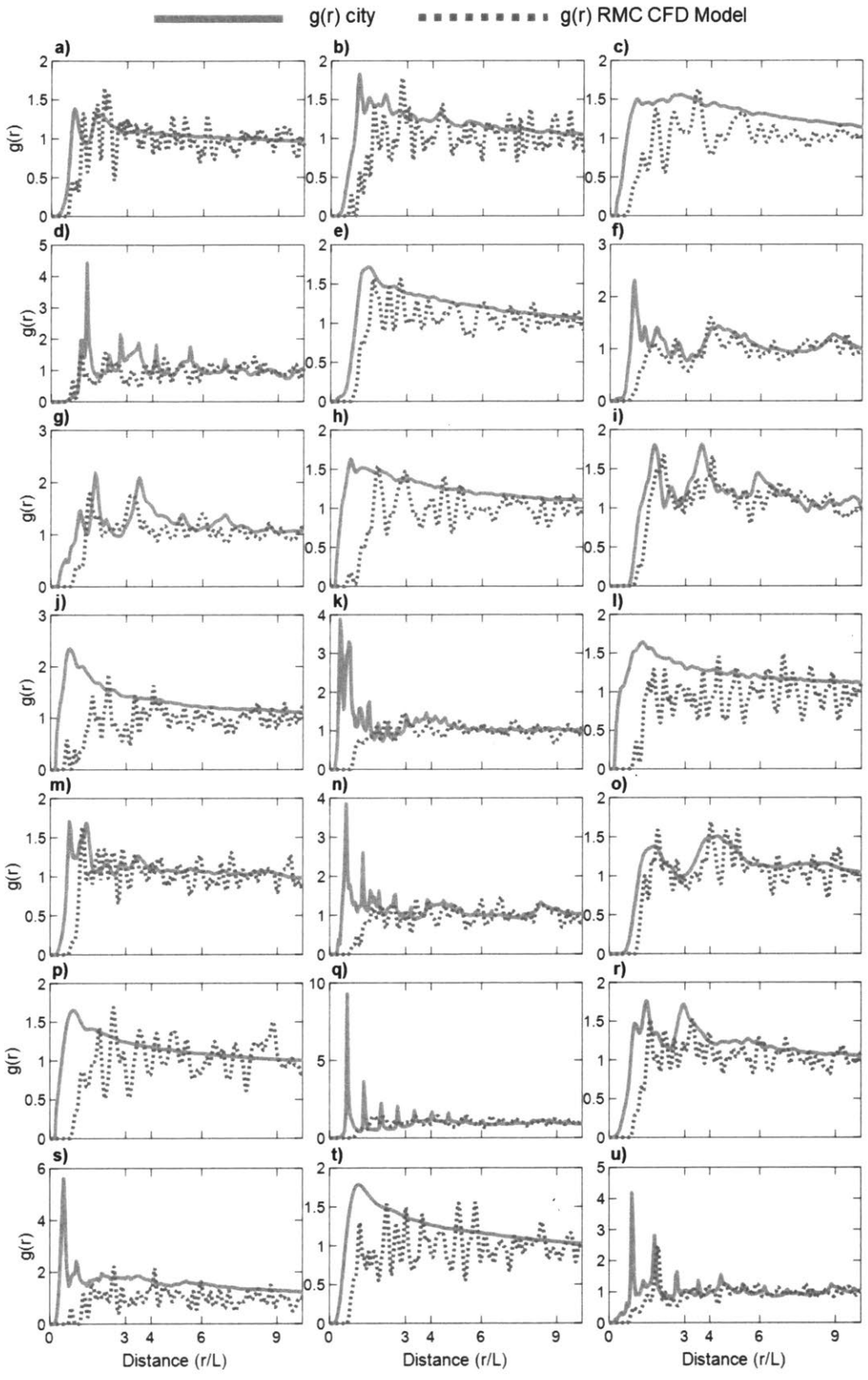

FIG.3-14. $g(r)$ distribution for CFD samples.

Chapter 4

4. Urban Heat Island (UHI): Intensity and Cost

In this chapter we address the question of what role city texture has on UHI and whether the effect has positive or negative impact on the energy consumption of buildings. We begin by explaining the methodology for quantifying UHI, values which we use to correlate with city texture for 22 US cities. In the second part we focus on the economic and environmental analysis of UHI in order to identify its impact on the residential heating and cooling energy bill and emissions associated with energy consumption at the state level.

4.1. Quantifying Urban Heat Island

In order to study the impact of city texture on Urban Heat Islands (UHI) at the city scale, we analyze hourly night-time peaks of UHI for twenty-two US urban air temperature time series [Table 2-1] for a period of multiple years– a time domain, which is large enough to provide us with statistically sufficient sample, but not too large to be influenced by global warming effects. The hourly temperature data unveil large fluctuations due to changing weather conditions that superimpose UHI. However, Fourier transformed temperature series depict distinct maximal peaks for the periods of 24 hours. These peaks when added to time-averaged temperatures constitute a reliable measure of nocturnal UHI, ΔT_{u-r}. It is imperative to emphasize that the goal of this work is to measure and model to what extent city texture alone can describe variations among ΔT_{u-r}. for different cities (all other important factors influencing nocturnal UHI are captured by a phenomenological parameter γ, which is explained in the later part of this chapter). This type of approach not only allows us to study the role of city texture in UHIs at nighttime, but it also provides grounds to estimate the significance of other parameters that influence UHI by observing discrepancies between the measured data and our model.

For urban and rural temperature datasets, we calculated the median value of temperature difference. Due to high disparity in signal of temperature variation [Fig.4-1], we concluded that

median value, which is closer to the peak of signals probability distribution, is more representative of the whole distribution than an arithmetic average. While this approach is preferred due to its intrinsic property of minimizing error in calculations, it is worth noting that the median value is

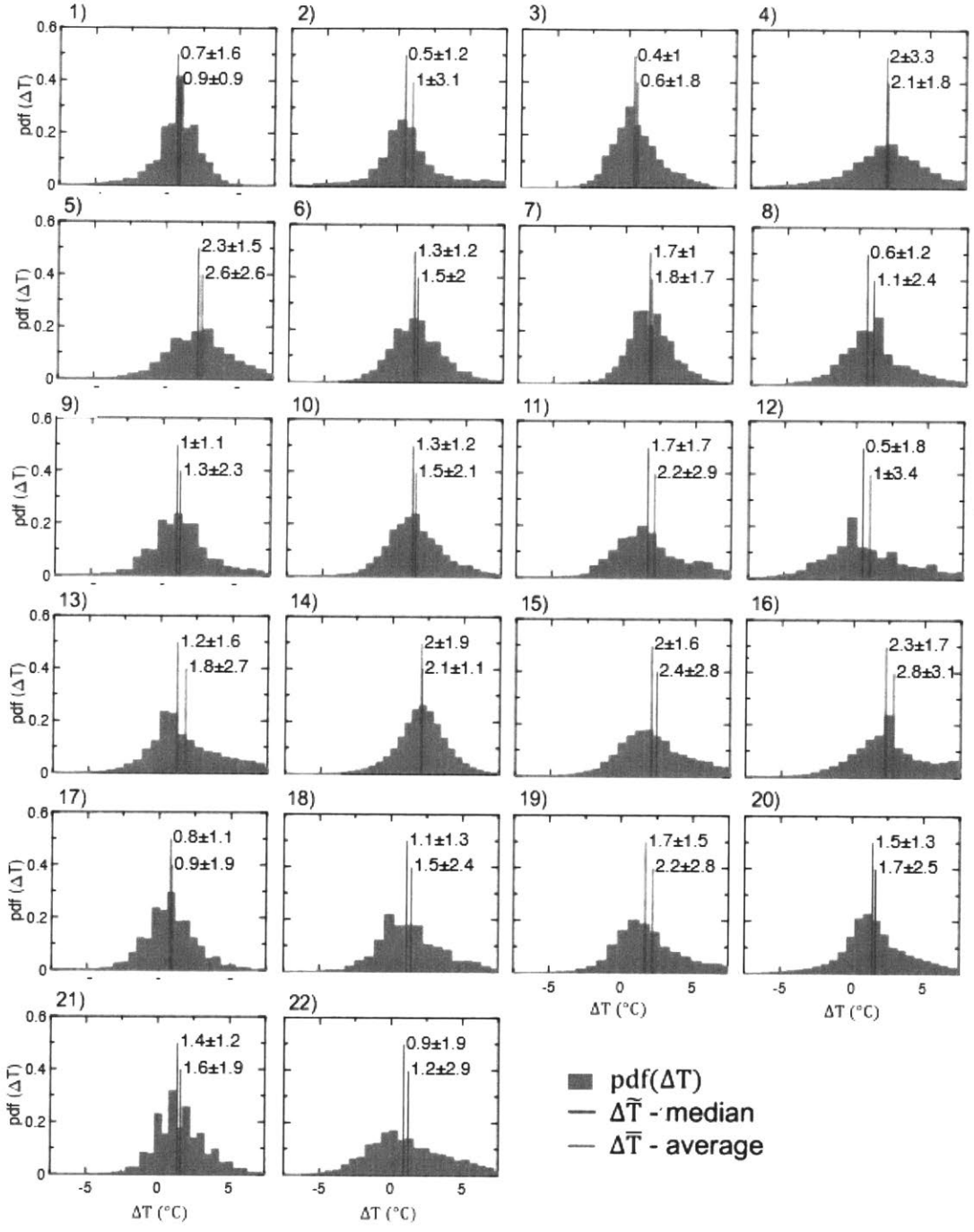

FIG.4-1. Distribution of Temperature Differences. Probability Distribution Function (pdf) for hourly temperature difference between urban and rural areas [Table 2-1] showing weak characteristics of positively skewed normal distribution

related to temperature variations obtained from maximum, minimum, and average daily UHI measuring approaches; in addition to the 4th power of the temperature difference used in radiative energy calculations [Fig.4-2]. All these methods that all have been used to measures UHI effects (*130*). For multiple health and energy related applications, UHI intensity (also known as maximum UHI) poses a greater concern than the daily, or night-time averages.

We have already established that the maximum UHI is correlated to median UHI [Fig.4-2]; however, a simple arithmetic average of maximum hourly temperature difference during 24h periods imposes a significant error due to high disparity in the signal wave.

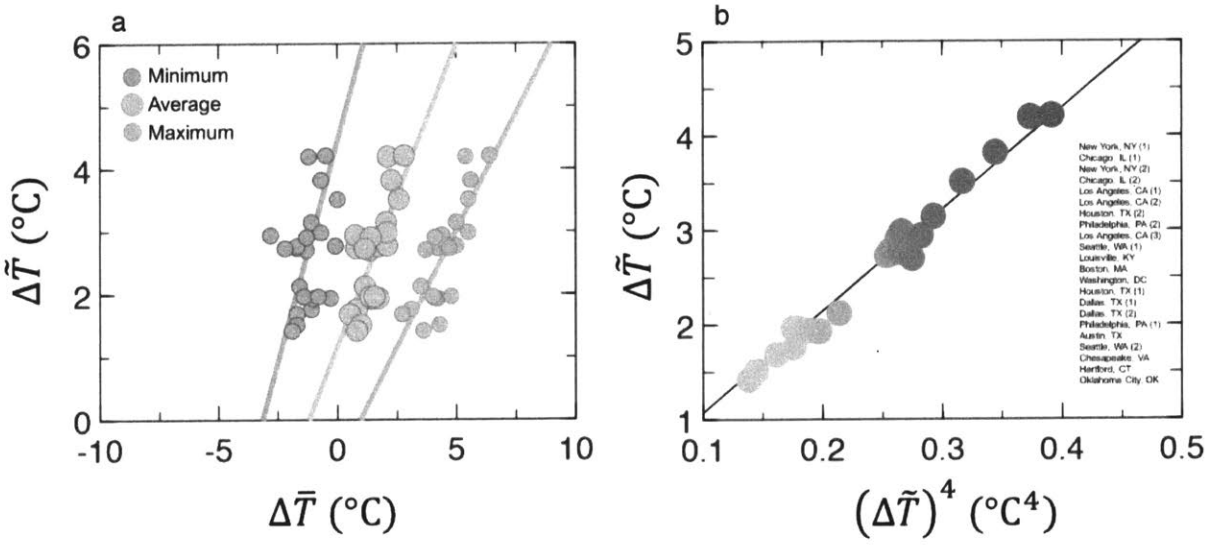

FIG. 4-2. Comparison of Temperature Differences.

Various modes for quantifying temperature difference, ΔTs between cities and their rural surroundings, showing that regardless of the method, various ΔTs are correlated in a linear manner. In a) median $\Delta\tilde{T}$ is compared with daily average, minimum and maximum $\Delta\bar{T}$, while in b) $\Delta\tilde{T}$ is juxtaposed to the median of fourth power of temperature difference, $(\Delta\tilde{T})^4$, which would be used to calculate radiative heat transfer.

4.1.1. Fourier Transform

In order to reduce statistical error severity in temperature calculations, we have utilized Fourier Transform, a function that is widely used in the analysis of signal waves. The function can be

employed to study time and frequency domains of the signal. For periodic signals where values are repeated in regular intervals, the Fourier Transform can be applied to simplify the analysis to a set of Fourier series coefficients, which is represented by the amplitude spectrum in the frequency domain. The temperature Fourier Transform can be written as an integral of the temperature difference, ΔT signal function:

$$\tilde{T}(2\pi/t) = \int_0^{t_f} \Delta T(t) e^{-2\pi i t x} dt \qquad [4.1]$$

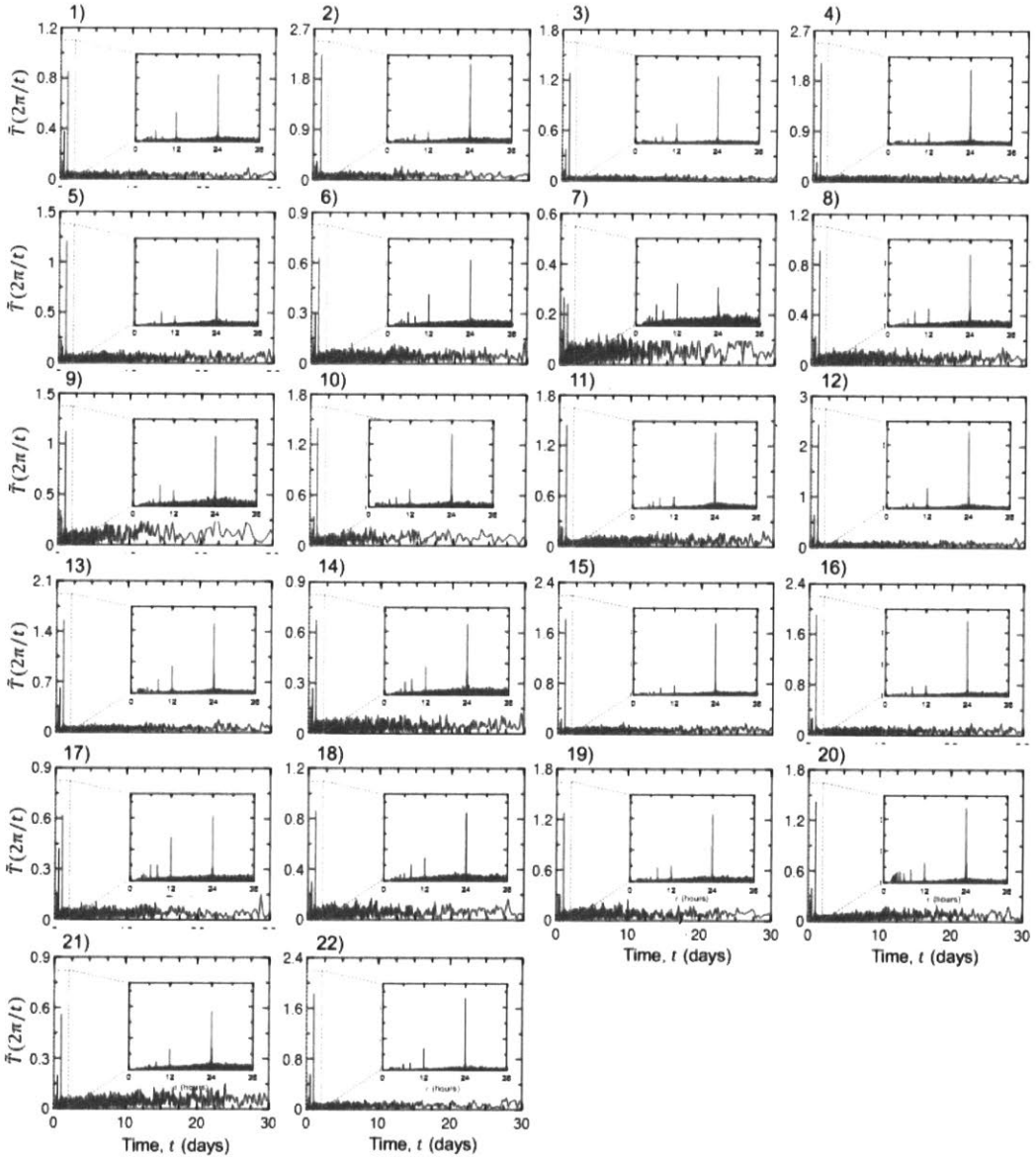

FIG. 4-3. Fourier transformed times series of urban–rural temperature difference [Table 2-1]

where t is corresponding time, x is frequency of the function and π and i are constants. The major advantage of using Fourier Transform to analyze temperature signal is its intrinsic ability to extract the characteristic sinusoidal wave properties from a noisy set of data. We would expect that due to UHI cities are on average warmer than areas outside the city meaning that on average $\Delta T_{u-r} > 0$. In addition, it is reasonable to conclude that the distribution of $\tilde{T}(2\pi/t)$ resembles a periodic wave, which remains constant, since global warming effects may be neglected for a short period of few years. Using the entire distribution of temperature differences as inputs for Fourier calculations, we obtained spectral distributions, $\tilde{T}(2\pi/t)$ in time domain t; we found that period of 24 hours (h) is most exemplary of the signal presenting highest amplitude [Fig.4-3]. Establishing that daily temperature difference does indeed coincide with the sinusoidal wave allowed us to proceed with the analysis of the nighttime UHI temperature difference [Fig.4-4], which we defined as the sum of Fourier transform [Fig.4-3] and median value of hourly temperature difference [Fig.4-1]:

$$\Delta T_{u-r} = \tilde{T}(2\pi/t_{24}) + \Delta\tilde{T} \qquad [4.2]$$

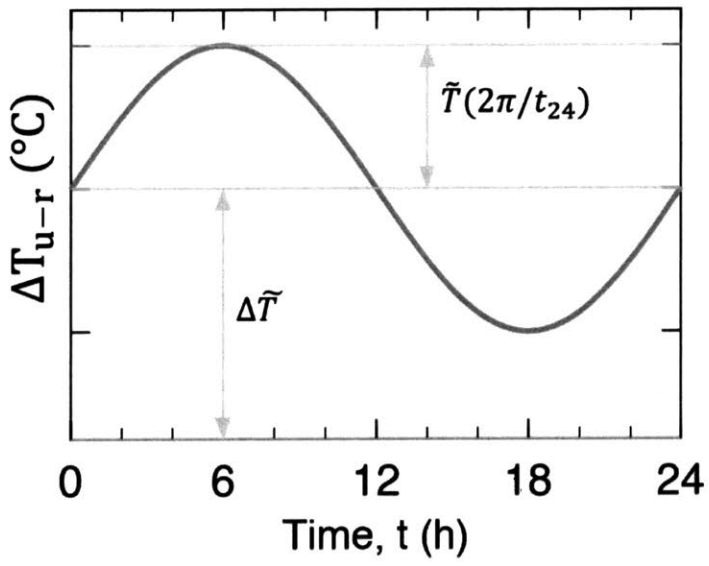

FIG. 4-4. Quantifying Urban Heat Island. Exemplary visualization of daily temperature difference, ΔT signal. Urban Heat Island effect is quantified by adding $\Delta\tilde{T}$ to the amplitude of the 24-hour period temperature difference wave obtained using the Fourier Transform, $\tilde{T}(2\pi/t_{24})$

4.2. Role of City Texture in UHI at nighttime

Early UHI studies have established empirically a scaling of UHI with population (*55*) - a common hypothesis for the nocturnal UHI (*60*). While our obtained values for ΔT_{u-r} are indeed correlated with the population [Fig.4-5], we find that with the urban geometry encoded in $g(r)$, the correlation is more evident. A relationship of this kind is consistent with the notion of reduced efficiency at which street canyons release heat at night (*142*). However, our detailed analysis of building footprints supports a more complex dependence of UHI on city texture. When compared to the ratio of $\Delta T_{u-r}/(R_{min}^{g(r)})^2$ we find that this cluster size, $R_{min}^{g(r)}$ scales according to a power law [Fig.4-6]. To reconcile this type of scaling with the previously established correlation between UHI and the sky view factor, we utilize a simple heat radiation model.

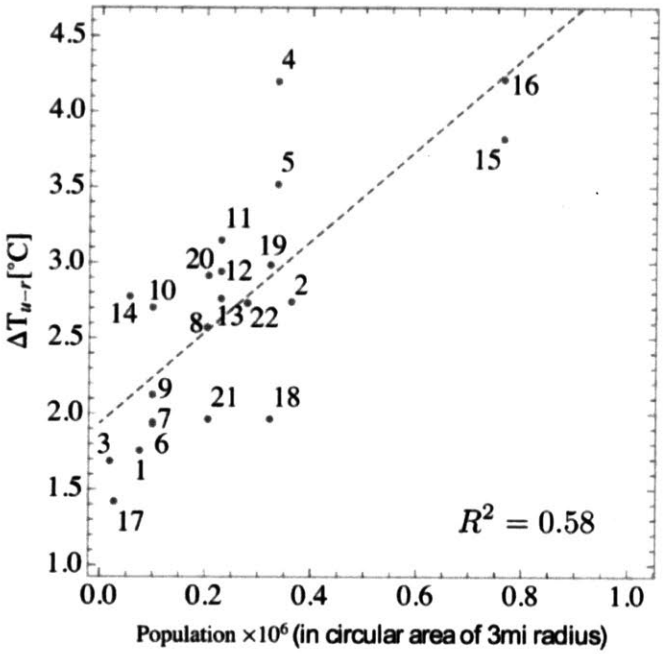

FIG. 4-5. Relationship between UHI and Population Density

Relationship between $\Delta T_{u-r}s$ and the population within a 3-mile radius from urban weather stations for GIS cities [Table 2-1].

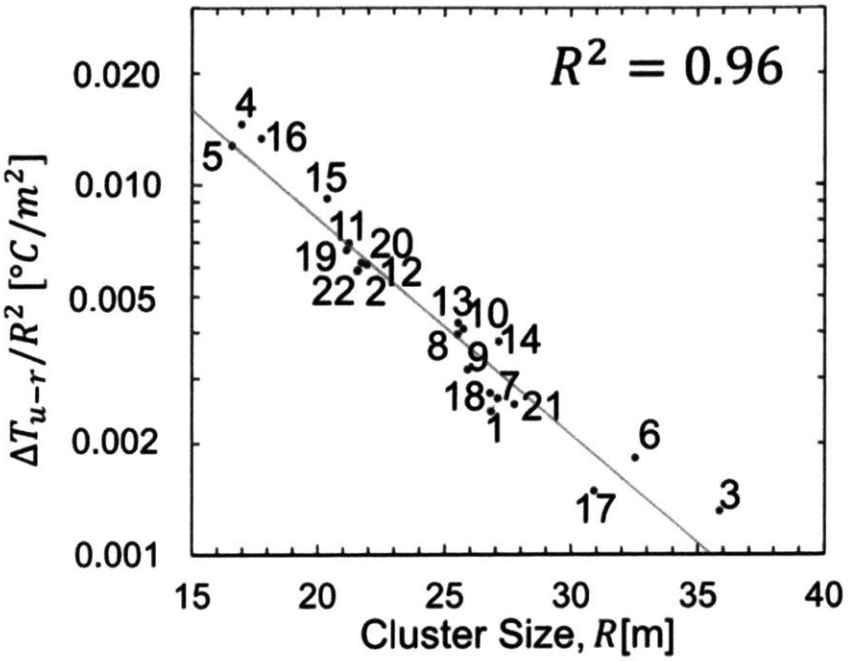

FIG. 4-6. Relationship between ΔT_{u-r} and the cluster size $R = R_{min}^{g(r)}$. Measured and model-predicted relationship of city texture [Table 2-1], obtained from the upper limit of the integral of the first peak of $g(r)$, shows a strong negative correlation captured with a power law.

4.2.1. Heat Radiation Model

We employed a scaling approach to model the dependence of the urban-rural temperature difference ΔT_{u-r} on urban texture, described by the characteristic length scales of $g(r)$. We denote the average temperature of at urban surfaces by $T_{u,flat}$ and the usually different average temperature of at rural surfaces by T_r. The difference between these two temperatures is due to material and climate induced processes, which are summarized in the relation:

$$T_{u,flat} = \gamma T_r \qquad [4.3]$$

with a phenomenological coefficient γ. Please note that this relation applies to at surfaces and does not account for urban geometry, i.e., the size, height and shape of buildings and their separation. The coefficient γ hence depends on the difference between thermal admittance and evapotranspiration properties in the rural and urban areas. To describe the effect of city texture, we resort to the device of an effective temperature that is often used for a body as an estimate of its surface temperature when the emissivity is not known (*154*). The effective temperature T_{eff}, defined as the temperature of a black body with the same power P radiated as the original body so that, according to the Stefan-Boltzmann law:

$$P = \sigma A T_{eff}^4 \qquad [4.4]$$

where, A is the surface area of the body and σ is the Stefan-Boltzmann constant. The city texture can be considered as a rough surface on the length scale of buildings with its effective emissivity not known. We expect that the effective temperature for the infrared heat radiation of city texture is mainly determined by the increase in its surface area due to building surfaces (assuming that multiple reflections of heat radiation between surfaces can be neglected). Following the above definition of an effective temperature, the effective urban temperature T_u is given by the relation:

$$A_{ground} T_u^4 = T_{actual} T_{u,flat}^4 \qquad [4.5]$$

where A_{ground} is surface area of the ground covered by city texture and A_{actual} its actual surface area including buildings surfaces like walls and roofs. The scaling of the surface area ratio $A_{ground} = A_{actual}$ can be estimated from the typical distance $d = R_{peak}^{g(r)}$ between buildings, and their mean linear size L and mean height H. The building wall area is approximately $4LH$ and the number of buildings scaling as:

$$A_{ground} = (d + L)^2 \qquad [4.6]$$

where $(d + L)^2$ is the typical area of an elementary urban block consisting of a building and the adjacent open space. Hence the actual urban surface area becomes:

$$A_{actual} = \left[1 + \frac{4LH}{(d+L)^2}\right] A_{ground} \equiv \delta(L, H, d) A_{ground} \quad [4.7]$$

so that the effective urban temperature scales as $T_u = T_{u,flat}\delta^{1/4}$ and the amplitude of the UHI, i.e., the rural-urban temperature difference is given by:

$$\Delta T_{u-r} = T_u - T_r = T_r\left(\gamma\delta^{1/4} - 1\right) \quad [4.8]$$

The main assumption of this model is that at nighttime, only long wavelength infrared (IR) radiation emitted from urban surfaces contributes to UHI (*154*). Of course, the surface temperature at night is also partially influenced by the absorption of short wavelength radiation during the day. However, this day-time absorption is also influenced by the city texture (*57*, *155*). In order to demonstrate that a simple scaling theory accounts for UHI variations with city texture measured by g(r), we separate contributions of non-geometric origin from ΔT_{u-r}. To do that, we assume that flat urban surfaces have an average temperature $T_{u,flat}$, which is different from the corresponding temperature of rural surfaces, T_r. This is due to increased sensible heat storage, decreased evapotranspiration, moisture and increased absorption of ultra-violet (UV) radiation in the daytime (*156*). The cumulative effect of the urban-rural difference between the latter processes is summarized by Eq. (4.3) for flat surfaces. For a quantitative description of the reduced nocturnal heat release from urban areas (due to their increased "roughness"), we resort to the device of an effective temperature T_{eff} – an approach that is frequently used to estimate surface temperature of a body when the emissivity is unknown (*154*). T_{eff} is defined as the temperature of a perfect black body that radiates the same power P as the actual body according to Eq. (4.4). By analogy, we can apply this concept to cities. Since the wavelength of IR radiation is much shorter than all relevant urban length scales, diffraction effects can be neglected and an increase in surface area attributed

to buildings (when compared to rural areas) determines T_{eff}. Assuming buildings of size L and mean height H, separated by an average distance d, our model predicts that:

$$\Delta T_{u-r} = T_r \left[\gamma \left(1 + \frac{4LH}{(d+L)^2} \right)^{1/4} - 1 \right] \qquad [4.9]$$

This prediction can be probed by field data in different ways, which is important since the availability of geometric data for most cities are either incomplete (i.e. building heights are missing), or only sky view factors are available. For GIS 3-mil cities, there is no information on building heights, but there is detailed data on building footprints. Therefore, for each city we are able to compute L and d. We compare these values to our theoretical model by minimizing (with respect to T_r, γ, and H) the squared deviations between the data for T_{u-r} of all twenty-two cities [Table 2-1] and the corresponding predictions from Eq. (4.9) with obtained values for L and d (which are related to the Mermin order parameter φ, density ρ and R). In the end, we find a convincing agreement yielding a coefficient of determination, $R^2 = 0.77$ [Fig.4-7.b] for the following parameters: $T_r = 20.5°C$, $\gamma = 1$ and $H = 9.5m$. Since most of the analyzed urban areas are mainly residential, we can conclude that the result for the mean building height H is reasonable. However, we have estimated correction factors for the mean buildings' heights that would yield an ideal agreement with our model. The relationship suggests that corrections of only ±30% of H would be needed for a perfect agreement with Eq. (4.9). Information on the building heights would allow to estimate the volume of built environment and consequently the thermal mass which could account for these corrections. Knowing the mean height H, building size L, and distances R and d for all GIS 3-mil cities, Eq. (1) yields a function $\Delta T_{u-r}/R^2$ that can be compared to the measured relation between ΔT_{u-r} and the cluster size $R_{min}^{g(r)}$ [Fig.4-6]. Using T_r as the sole fitting parameter, we find a convincing agreement with $R^2 = 0.96$ for $T_r = 24.4°C$, which is consistent with the solar irradiance values (*154*).

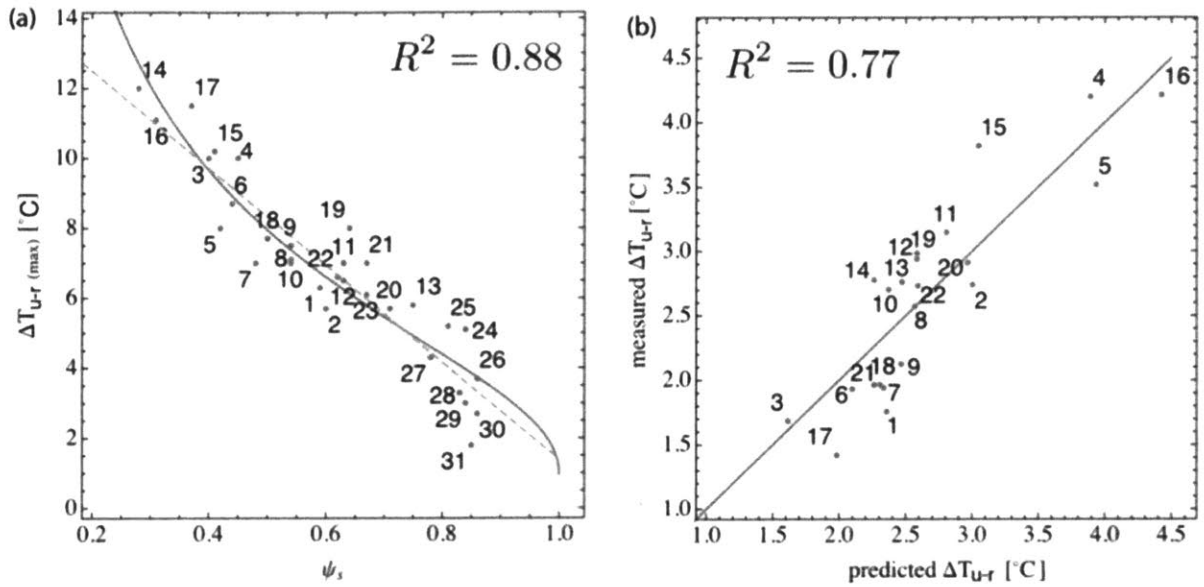

FIG.4-7. Relationship between measured and model-predicted ΔT_{u-r}. (a) maximal ΔT of cities as a function of the sky view factor ψ_s from Oke (*157*) together with the linear fit of Oke (dashed line) and the fit to our model (solid curve), from Eq. (4.10). Numbers in the figure correspond to cities analyzed by Oke (*157*). (b) Comparison of measured and predicted ΔT_{u-r} for GIS 3-mil cities using Eq. (4.9)

Further credibility of our model is obtained by its application to the previously collected data of cities (*157*), providing an insight into ΔT_{u-r} dependence on building height. We express the ratio H/d in terms of the sky view, ψ_s, assuming a canyon geometry (*143*, *157*), which leads to $H/d = \frac{1}{2}\tan[\arccos(\psi_s)]$. Our model then predicts:

$$\Delta T_{u-r}(\psi_s) = T_r\left[\gamma\left(1 + \frac{2\frac{\mathrm{L}}{\mathrm{d}}\tan[\arccos(\psi_s)]}{(1 + L/d)^2}\right)^{1/4} - 1\right] \qquad [4.10]$$

where T_r, γ, and L/d are determined from field data. Contrary to the empirical linear relation between ΔT_{u-r} and ψ_s, Eq. (4.10), our model provides an expression that is derived from the fundamental principles of heat radiation. Comparison to the measured field data results in fitting parameters $T_r = 40.4°C$, $\gamma = 1.024$ and $L/d = 1$ (Fig.4-7.b), which yield a coefficient of determination of $R^2 = 0.88$, similar to what has been observed for a linear relation.

4.2.2. Urban Surface Temperature from Solar Radiance

The surface temperature $T_u = T_{u,flat}$ obtained from the fit of Eq. (4.9) in the main text with $\gamma = 1$ to the data shown in Fig.4-6 can be estimated from a simple radiation balance model. A flat surface is characterized by an emissivity ϵ, a thickness s, and thermal conductivity κ. On the inside of the surface an equilibrium temperature is maintained. Assuming that the surface receives a homogeneous solar radiant flux L_0 from the outside, we can estimate the equilibrium temperatures T_{out} on the outside of the surfaces by equating the internal and external net flux densities. The internal net flux is obtained from the stationary heat conduction equation:

$$q_{int} = -\kappa \partial_n T \qquad [4.11]$$

integrated across the surface thickness s yielding:

$$q_{int} = (T_{out} - T_{in})\kappa/s \qquad [4.12]$$

The external net flux q_{ext} is obtained as the sum of the incoming solar flux L_0 and the heat flux $\epsilon\sigma T_{out}^4$ radiated by the surface where σ is the Stefan-Boltzmann constant. The condition $q_{ext} = q_{int}$ then yields:

$$(T_{out} - T_{in})\kappa/s = \epsilon(L_0 - \sigma T_{out}^4) \qquad [4.13]$$

which determines the outside surface temperature T_{out} of the surface that can be identified with T_r. The result $T_r = 24.4°C$ obtained from the fit to our model is reproduced by the typical parameters $\epsilon = 0.92$, $\kappa = 1W/mk$, and $s = 20cm$ for an interior building temperature of $T_{int} = 22°C$ and a solar radiance of $L_0 = 458W/m^2$.

4.3. UHI Cost

To be able to understand the influence that local temperature variations (i.e. UHI) have on energy consumption, we must employ the correlation between temperature and degree days. We find that the concept of degree days can be generalized to the set of equations based on the correlation between historical average monthly temperatures, T_m and the number of HDD_m and CDD_m with the data obtained from NOAA/NCDC Climate Division for the period between 2005 and 2016. They can be modeled using the following equations:

$$HDD_m = \begin{cases} -29.54 \times T_m + 1941 & , \quad T_m \leq 60°F \\ 1.43 \times 10^{25} \times T_m^{-12.85} & , \quad T_m > 60°F \end{cases}$$

$$CDD_m = \begin{cases} 29.58 \times T_m - 1905 & , \quad T_m \geq 70°F \\ 1.07 \times 10^{-18} \times T_m^{10.96} & , \quad T_m < 70°F \end{cases}$$

[4.14]

4.3.1. Energy Consumption and Degree Days

Energy responsiveness of buildings due to changes in outdoor temperature is dependent on multiple factors, such as thermal comfort of residents, efficiency of the buildings, which measures how much energy is lost through building's envelope, size of the building, number of household members, or presence and type (i.e. central, window) of air conditioning. However, their contribution to the overall building energy consumption varies significantly and the outdoor temperature is considered to be the driving factor (*52*, *86*). Therefore, using just a single input of outdoor temperature it should be possible to predict the space heating and cooling energy consumption of residential buildings. The correlations obtained using Eq. (4.14) allow us to confirm that notion, that changing temperature (i.e. due to global warming or UHI) affects the number of degree days, which are directly related to state-wide annual residential heating and cooling energy consumption. More specifically, we find that using a linear regression model, it is possible to correlate annual state residential heating energy consumption with annual HDD, which

is captured with the heating energy response of a residential buildings, m_h, equal to 2.20 kWh per HDD [95% CI: 2.05, 2.35] [Fig.4-8.a]. Similarly, annual state residential cooling energy consumption scales linearly with the annual CDD, which is captured with the cooling energy response of a residential building, m_c, equal to 1.80 kWh per CDD [95% CI: 1.62, 1.98] [Fig.4-8.b]. While neither of these correlations offers a robust relationship that would predict accurately heat or cooling energy demand with just a single input of temperature or degree days, they both offer meaningful, statistically significant—with coefficients of correlation, R^2 equal to 0.66 and 0.73 for heating and cooling energies, respectively— positive correlations, which we can utilize to estimate values for heating and cooling energy consumptions.

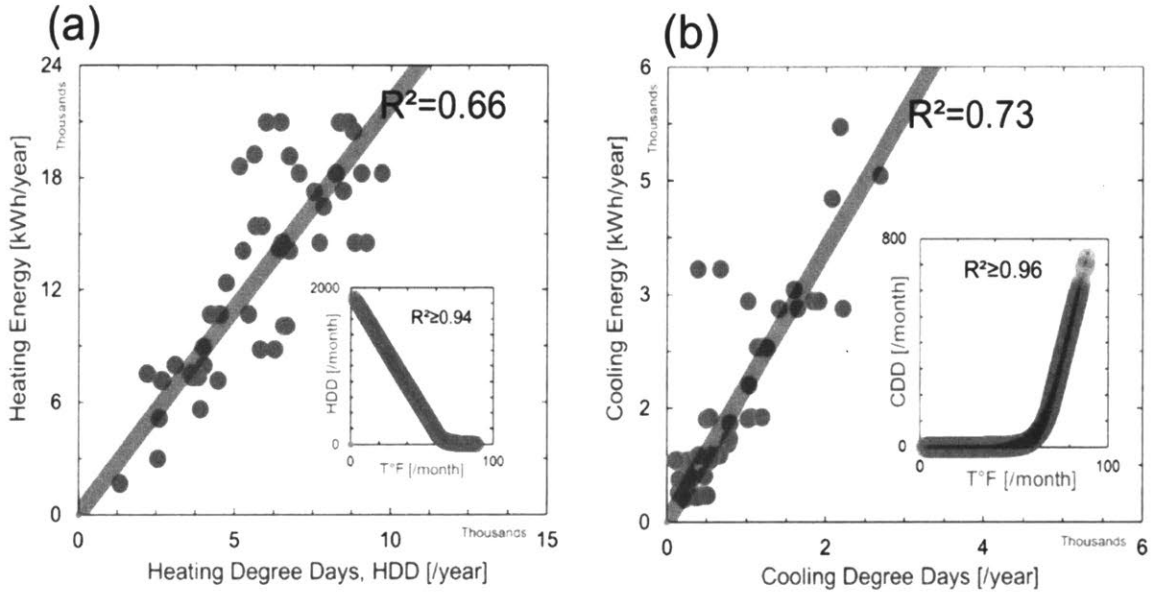

FIG.4-8: Residential Energy Consumption. Residential Household Heating and Cooling Energy Consumption showing (a) linear relationship between annual heating energy consumption and HDD. The inlet shows the fitting model between monthly HDD and temperature (b) linear relationship between annual cooling energy consumption and CDD. The inlet shows the fitting model between monthly CDD and temperature. Monthly Degree Days and Temperature for 2005-2016 were obtained from NOAA/NCDC Climate Division.

4.3.2. Energy Expenditure

To estimate residential space heating and cooling costs, we resort to EIA's annual average retail residential user prices for non-renewable energy fuels used in the US. Using EIA's guidance for

residential fuel sources, we limited electricity, natural gas, propane, and heating oil as the only heating source fuels. Due to availability of data, we assume that fractions of the heating fuel sources remain unchanged for each of the states within the boundaries of these energy regions: west, midwest, northeast, south. Due to lack of prices, we disregarded wood and due to their minimal contribution, we did not include kerosene or any of the renewable sources. For space cooling, we assumed that all energy is supplied with electricity (due to their minimal contribution renewable resources were ignored). Lastly, any variables that could influence energy responsiveness of buildings to changes to outdoor air temperature remain constant over the time. Electricity and natural gas prices are annual residential averages for each state. For heating oil and propane, we used weekly prices, which we converted to annual averages. For states with missing values, we used (when available) regional or national averages.

Space heating and cooling in residential buildings requires a mixture of various energy sources. While on-site energy usage is an important measure in evaluating performance of a building and understanding its sustainability rank, it is not representative of how much energy must be generated to deliver each unit of energy to a building. Therefore, to account for any losses and inefficiencies

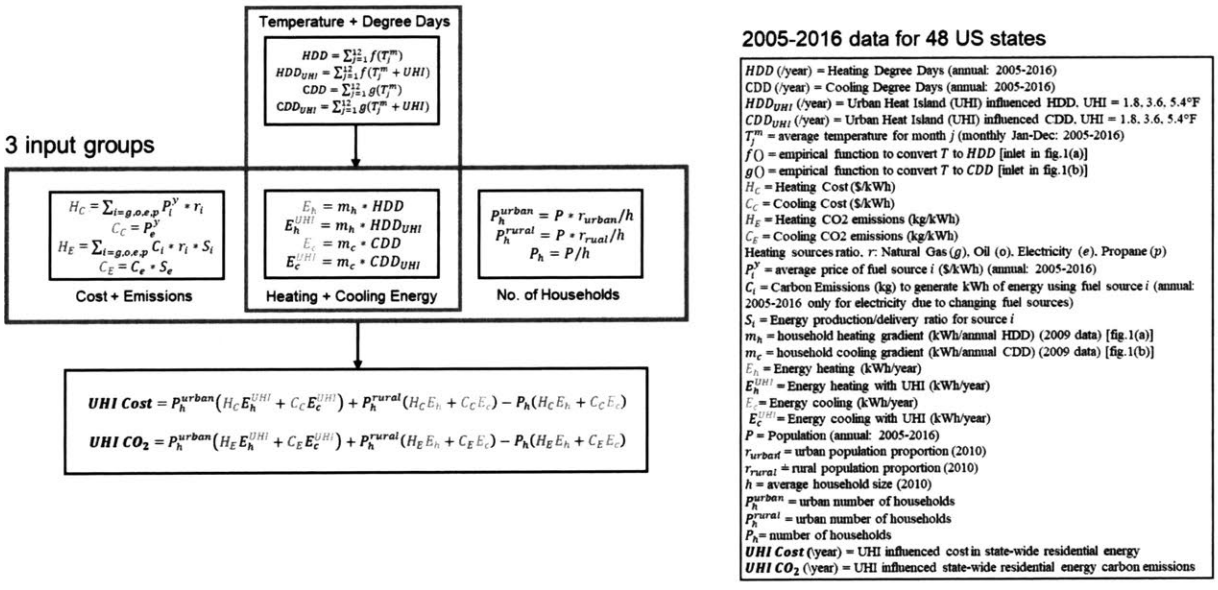

FIG.4-9. UHI Costs + Emissions Flowchart: Visual representation of the methodology employed to calculate annual UHI state residential heating and cooling energy cost and carbon emissions.

during the production and delivery processes of energy, we adopted a source energy measure (S_i) from Energy Star Portfolio Manager Technical Reference (*158*), which traces the on-site energy back to its raw fuel input, thereby enabling a complete thermodynamics assessment. For US buildings, to deliver a single unit of energy on-site the following ratios of fuels need to be produced: electricity (3.14), natural gas (1.05), heating oil (1.01), and propane (1.01). To exemplify this implies that on-average for each 1 kWh of end-use electricity, 3.14 kWh must be generated. One or even 5% fuel losses may seem insignificant when compared to 3.14 ratio for electricity. Although, these statistics are appropriately reflected in higher electricity prices when compared to other fuels—which on average are 2-2.5 higher— we want to establish how they affect the amount of carbon dioxide generated to supply residential space heating and cooling energy across the US. The next step is to quantify the amount of CO_2 for each kWh of energy (C_i). To quantify CO_2 emissions associated with heating and cooling energy consumption, we obtain national source values for raw fuels used in electricity generation by year while disregarding any renewable resources. For residential energy production in the US, there are only three non-renewable fuels that contribute to most electricity generation (used for space heating and cooling), while for space heating there are four sources. For natural gas (0.18 kg per kWh), heating oil (0.25 kg per kWh), propane (0.22 kg per kWh) emission levels are assumed to be constant for the 12-year period. However, for electricity we utilize net generation energy sources (coal, hydroelectric conventional, natural gas, nuclear, other, other biomass, other gases, petroleum, wood and wood derived fuels, geothermal, pumped storage, thermal and wind) used for annual total electric power industry production also obtained from EIA. Based on the ratio of different sources, we obtain average CO_2 kg per kWh of electricity for each state for each year.

We utilized preceding steps to establish a methodology to quantify the impact that UHI has on residential space heating and cooling energy consumption. The flowchart of this methodology is depicted in Fig.4-9. To derive the equation for state-wide environmental and energy costs associated with the of impact of UHI three inputs are necessary: 1) residential heating and cooling energy consumption per building for temperatures with and without UHI [Fig.4-8], 2) heating and cooling costs and emission levels and 3) the number of households in each state. While, EIA provides total state energy expenditure values in conjunction with the household ones, but they come with an error imposed by the averaging approach used for low population states. To depress

this error, we use population and average household size data (*134*, *135*) to estimate the total, as well as the urban number of households in each state. We convert estimated values of population for each year between 2005-2016, to urban (P_h^{urban}) and rural (P_h^{rural}) number of households by multiplying population values by appropriate urban/rural ratio and dividing it by an average household size (*135*). With three inputs obtained in such way we were able to quantify for annual UHI influenced heating and cooling costs ($UHI\ Cost$) and CO_2 emissions ($UHI\ CO_2$) for 48 individual US states using the following equations [Fig.4-9]:

$$UHI\ Cost = P_h^{urban}(H_C E_h^{UHI} + C_C E_c^{UHI}) + P_h^{rural}(H_C E_h + C_C E_c) - P_h(H_C E_h + C_C E_c) \quad [4.15]$$

where, H_C stands for heating cost, E_h^{UHI} is UHI influenced heating energy, C_C is cooling cost, E_C^{UHI} is UHI influenced cooling energy, P_h is state's household population, E_h is the heating energy and E_C is the cooling energy.

$$UHI\ CO_2 = P_h^{urban}(H_E E_h^{UHI} + C_E E_c^{UHI}) + P_h^{rural}(H_E E_h + C_E E_c) - P_h(H_E E_h + C_E E_c) \quad [4.16]$$

where, H_E stands for heating CO_2 emissions, C_E is cooling CO_2 emissions. Using average monthly air temperature values for each state, we calculated the annual number of degree days for temperatures with no UHI effect, as well as three increments of UHI [1°C (1.8°F), 2°C (3.6°F) and 3°C (5.4°F)]. To understand what the absolute state-wide residential energy cost without UHI effect is, we combined annual energy prices with modeled heating and cooling energy usage [Fig.4-9] to obtain average heating and cooling residential energy cost per year (averages for years 2005-2016) for each of the US states [Fig.4-10.a]. For UHI calculations, we assume the UHI effect to be 2°C (3.6°F). Although we restrict our calculations to that average UHI of 2°C, we find that the impact on cost and CO_2 of the other two increments of UHI equal to 1°C (1.8°F) and 3°C (5.4°F) that prevail in the US (*65*), are linearly correlated with each other [Fig.4-10 inlets]. This shows that regardless of the magnitude of UHI, for state-wide residential sector in the US, we can generalize the UHI influence to be either positive or negative. Moreover, we find that increasing

UHI temperature by 1°C, on average intensifies UHI percentage energy costs by 40%, while reduction of 1°C translates to UHI percentage energy cost reduction by 46%. Moreover, we identified UHI influenced excess total and percentage costs and savings (UHI expenses) relative to the total residential heating and cooling energy expenditure. We categorized US states in terms of their UHI saving potential starting with regions where UHI of 2°C leads to the greatest absolute residential energy cost savings. It is worth noting that while absolute savings for a given state may appear large and significant when compared to the other states, the percentage UHI expense may act as a more appropriate metric for a evaluating the UHI impact on the residential space heating and cooling as it conveys more information about the distribution of energy expenditure within a state.

4.3.3. Carbon Emissions

Energy cost is one of the metrics of evaluating the impact of UHI on the residential sector. However, because heating fuel sources are different to the fuel sources needed for cooling energy, higher energy cost does not necessarily imply a proportional change in the levels of emitted carbon dioxide. This is mainly due to the fact that while energy prices fluctuate, the emissions associated with a particular source of fuel remain the same. Therefore, for as long as the efficiency of energy generation and its delivery do not change, while its supply prices do, it is expected that CO_2 emissions will not explicitly follow the pattern of UHI energy costs. This indeed is depicted by the middle inlet in Fig.4-10, which shows the slight disparity between UHI carbon emissions and UHI cost. Further, the variation in heating and cooling fuel sources across different states reflects in the order of states with the highest UHI CO_2 emission savings [Fig.4-10.b], which differs from the order of UHI energy cost savings. However, a linear regression fitting model shows that for the US states, on average the UHI cost translates to 4.64 times higher emissions of carbon dioxide. This means that knowledge of UHI cost allows one to identify associated UHI CO_2 emissions and vice versa. In other words, knowing UHI impact on state's residential energy bill allows us to approximate alteration in state's residential carbon emissions.

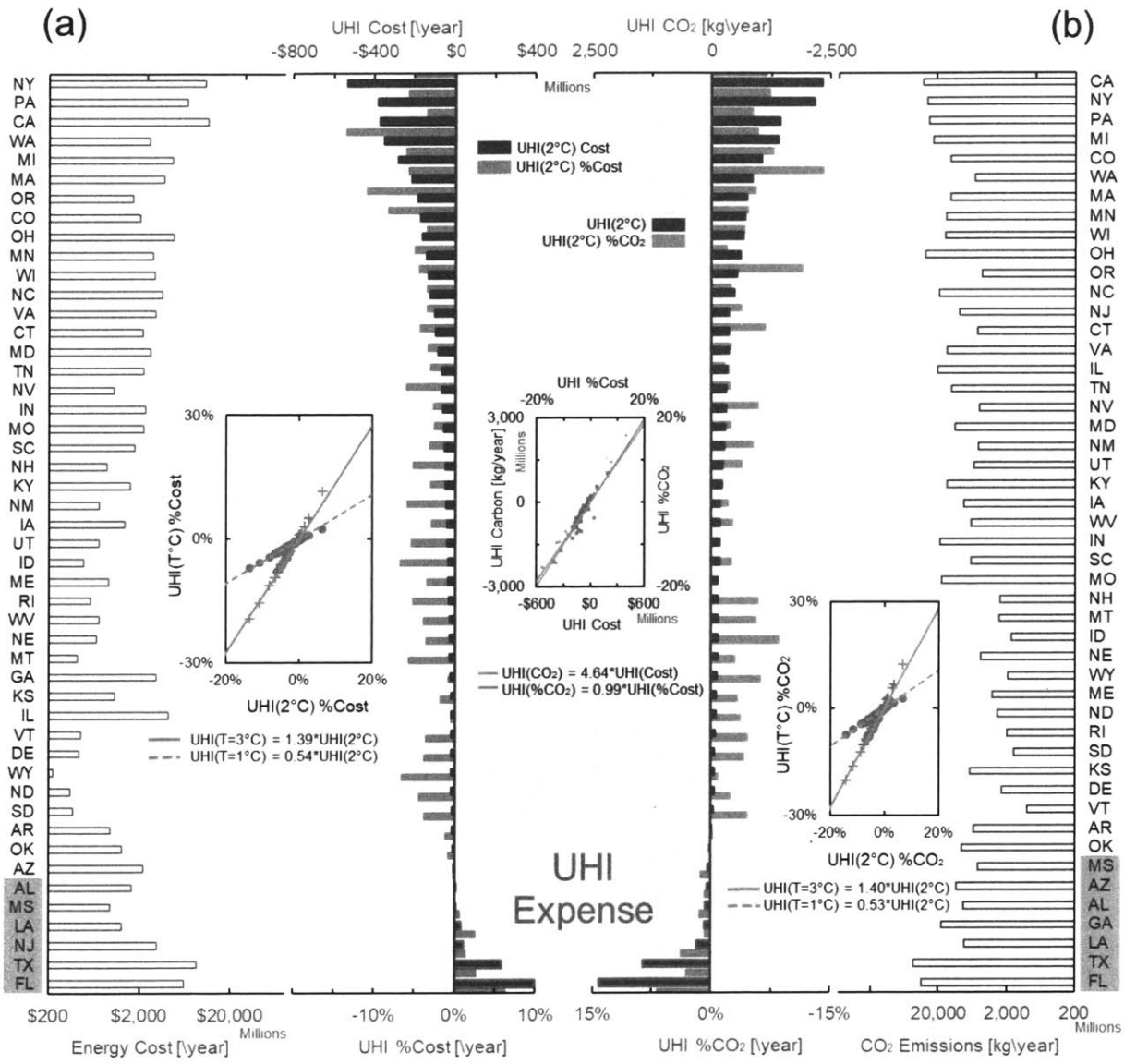

FIG.4-10. Residential heating and cooling energy cost and CO_2 emissions for 48 US states.

(a) on the left average annual non-UHI heating and cooling cost and on the right UHI=2°C annual cost and % differences relative to non-UHI total cost. The inlet shows linear relationships between different magnitude UHI % cost differences. (b) on the right average annual non-UHI heating and cooling CO_2 emissions on the right UHI=2°C annual CO_2 and % emissions differences relative to non-UHI emissions. The inlet shows linear relationships between different magnitude UHI % CO_2 emissions differences. The middle inlet figure represents linear scaling between UHI cost and CO_2 emissions.

The most critical and perhaps impactful part of this analysis, however, is obtained from the visual depiction of the UHI cost and CO_2 analyses captured in Fig.4-11 showing the varying effects of UHI across the US. The maps provide visual representation of parts of the US that are most

negatively affected by UHI = 2°C (red color states) as well as those where UHI has positive effects (green color states) and areas where UHI has marginal impact on the annual residential energy cost and emissions (yellow color states). Since there is a linear relationship between different magnitudes of UHI [Fig.4-10 inlets], with appropriate outdoor air temperature measurements for cities across a given region, the state-wide results can easily be transformed to more accurate values.

4.4. UHI impact on the US Residential Energy Cost and Emissions

UHI intensifies air temperature regardless of the season. Therefore, increase in cooling energy would correspond to decrease in heating energy for states that experience months with temperatures below 65°F. In fact, more than 80% of US states are located in areas with significant space heating energy bills suggesting that depending on energy fuels, UHI could have a positive impact—the reduction in annual residential energy bill cost and carbon emissions—on the overall energy consumption of the residential sector. Higher contribution of heating over cooling to the UHI energy bill occurs because energy response of buildings to changes in temperature is about 20% higher for heating than it is cooling, as depicted by Fig.4-8. This can be explained by the fact that while most heating systems are centralized, air conditioning systems for many US households are usually restricted to bedrooms and living spaces. We compared impacts of 1°C and 3°C UHIs with the reference base UHI equal to 2°C. As it is depicted in Fig.4-10, the various magnitudes of UHI are correlated in a linear fashion, where 1°C UHI depresses and 3°C UHI intensifies the percentage effect on residential state heating and cooling cost and carbon emissions of UHI = 2°C by factors of approximately 50% in both instances. In the context of this study, heating and cooling energy costs at the household level are affected mainly by regional variations in energy prices and emission levels by various types of heating and cooling energy generation sources. However, at the state level variations in energy cost and emissions are predominantly driven by population density. This is reflected in non-UHI residential energy cost and CO_2 emissions among the US states, where the highly populated states such as New York, California, or Texas, each year spend four times more than the US average, which translates to about $10B on residential heating and cooling and about 40M metric tons of CO_2 emissions each year [Fig.4-10]. While total energy costs and emissions for the residential sector are important metrics to consider, they alone should

not be regarded as the prioritizing factor for UHI mitigation strategies. By incorporating changing HDD and CDD due to various levels of UHI, we found that regional climate has a great influence on the percentage change in UHI driven cost and emissions levels, where states with high $HDD:CDD$ ratio, such as Washington, Oregon or Colorado experience between 9-12% reduction in the overall residential heating and cooling energy bill with UHI = 2°C.

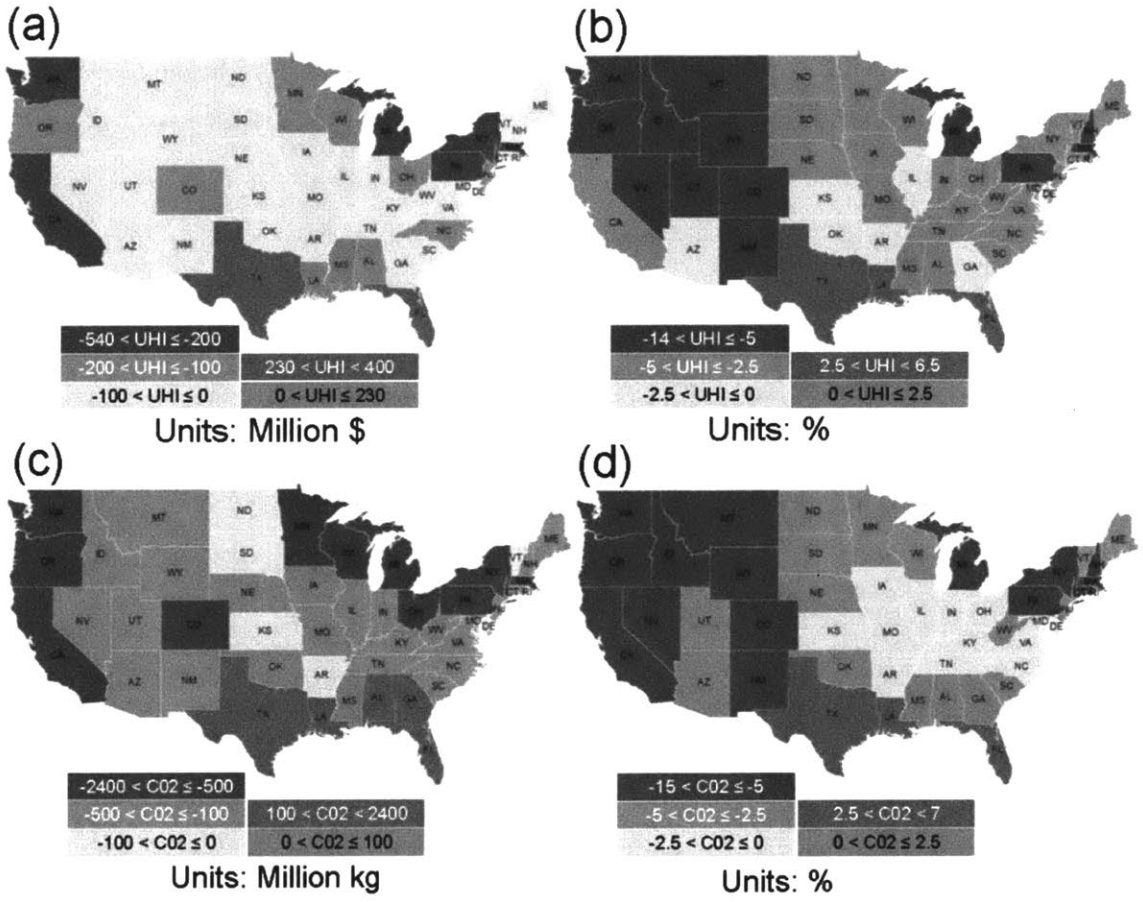

FIG.4-11. UHI Impact US Map. 12-year average annual state residential heating and cooling expenditure (a-b) and CO_2 emissions (c-d) for UHI=2°C.

To account for climate and energy price calculations, we analyzed data for a 12-year period between 2005-2016 and extracted averages. We argue that the impact of UHI should not be generalized as having solely negative impact on the environment and cost of energy. This is because it is an outcome of three variables: (1) climate, which constitutes HDD and CDD, (2)

energy prices, (3) types of fuels used for heating and cooling. Using annual averages, we found that there are only several states across the US that experience negative effects of UHI in terms of residential energy consumption. While for most US states UHI has marginal impact on energy costs and emissions (less than 5%), there are few states where UHI imposes a strenuous impact on the residential market energy and there are some where UHI offers a major benefit. For cities in the parts of the US that experience winter seasons, UHI may have a positive impact on residential buildings, as exemplified for UHI = 2°C in Figs.4-10 and 4-11. At the local level, a typical average household could save between $75-150 on their annual energy bill, while at the same time making contribution to reduction of carbon emissions of about 400-500kg, which approximately is equivalent to emissions produced by a 30mpg vehicle that has travelled 1750 miles. While these values may seem insignificant, in highly populated states such as New York, Illinois or Massachusetts they translate to UHI offering a substantial reduction in economic and environmental burdens with over $200M and as much $500M in annual heating savings and reduction of approximately 2M tons in CO_2 emissions. However, for states located in warm southern parts of the US, regions with high ratio of $CDD:HDD$ would on average increase annual energy bill by about $50-100, while creating an addition of about 300-600 kg to carbon emissions from a single household. For highly populated states such as Texas or Florida, these values translate the UHI equal 2°C to contribution of approximately $400M and 2M tons of CO_2 in additional energy costs and emissions. It is important to emphasize that while these values account for fluctuating climate and seasonality changes averaged out for a 12-year period, these values are still state-wide averages. However, due to linear relationship between different magnitudes of UHI it is possible to enhance them with local air temperature measurements for cities. This is especially relevant for states like California or Nevada whose boundaries extend across different climates with mountain and dessert regions that impose large errors in average temperature values.

This UHI analysis has been focused on the current state of the US stock of residential buildings, which neglects building and neighborhood designs as the potential mitigation strategies for ameliorating energy bill and carbon emissions. However, if we take into consideration changes in population that are expected to occur by 2030 (*134*), we can prioritize states for UHI controls and regulations based on their expected growth of urban number of households. Shown in Fig.4-12, we find that for most states we should expect at least 100,000 of new residences to be built in

urban areas, but for the few extreme cases, states such as Arizona, Texas, California and Florida, we can expect to see an urban household increase in excess of 1 million. Consequently, these are the states that should examine sustainable building design measures to reduce the environmental impact of residential buildings.

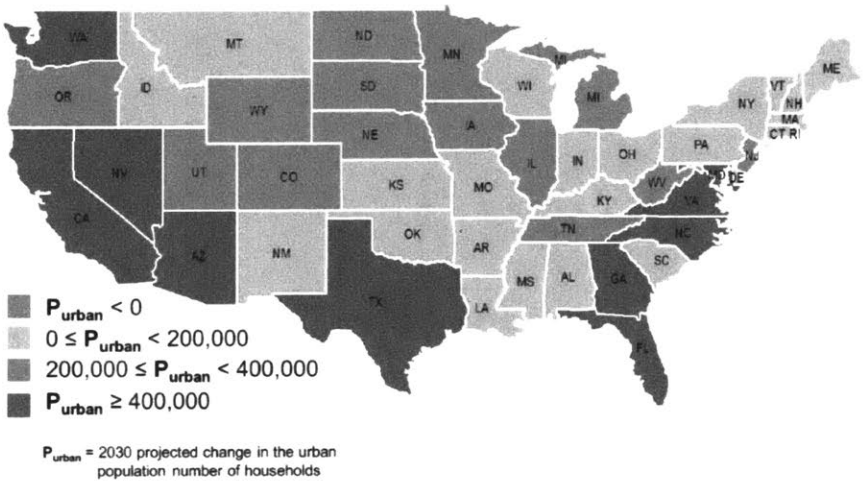

FIG.4-12. Urban Household Growth Projections in the US.

Projections of changes in the number of urban households between 2010 and 2030 visualized as a map categorized into four groups with blue color being representative of expected decline in the urban population number of household, P_{urban}, while three different shades of red showing projections for increase in P_{urban}.

4.5. Summary

Using a radiative heat model, we demonstrated that UHI scales according to a parameter derived from a city texture model. We identified that ordered, crystal-like cities experience higher UHI effects than disordered, liquid cities. We also demonstrated that the financial and environmental cost of Urban Heat Island effect is closely related to the regional temperature variations making the cost being either positive or negative. Providing a good overview of the scale of importance of UHI, when linked with urban population changes this analysis can be applied for prioritizing policies and regulations for UHI controls.

Chapter 5

5. Drag Coefficients and Hurricane Damage

In this chapter, we discuss the impact that city texture in magnifying drag coefficients used in deriving building safety design codes. We begin with a detailed description of building design codes, different flow regimes in cities and how they impact wind pressure loads. Next, we discuss the theory of fluid flow and how computational simulations can be used to solve it. In the second part of this chapter we apply the theory to create CFD simulations using models developed in chapter 3. We study the results to show that city texture enhanced drag coefficients can be used to predict more accurately wind loads under extreme wind conditions and ultimately used to create risk maps for areas prone to hurricane damage.

5.1. Building Design Codes

It is widely known that natural hazards, like hurricanes, cause tremendous levels of damage and that hazard mitigation can significantly curb natural hazard-induced losses, some of the costliest in the American history with damages totaling in excess of trillion US dollars during the course of past 2-3 decades. Moreover, with the predicted increased quantity and intensity of storms accompanied by hurricanes (*2*, *17*) and thousands of new properties being built in hurricane prone areas such as Texas or Florida [Fig.4-12], in the upcoming years this damage is expected to only magnify. To keep buildings safe from wind hazards they must be designed to a specific structural safety standard, a metric known as a building design code. According to FEMA, *"Building codes are sets of regulations governing the design, construction, alteration, and maintenance of structures."* One of their purposes is to protect the inhabitants of a building from natural disasters by specifying the strength of that building. During such extreme wind weather events, buildings may fail structurally, which occurs when pressure loads acting on a building exceed the norms to which that building has been build. There are specific guidelines for deriving this pressure standards, which are obtained using a random-vibration gust loading factor approach (*95*, *159*).

Different countries use different parameters to define these standards (*95*), but ultimately, they all rely on the fundamental pressure load, P_{wind}, equation:

$$P_{wind} = q \times C_g \times C_p \times C_e \times C_t \times C_{dir} \times C_i \times C_{other} \quad [5.1]$$

where, C_g is a gust factor, C_p is a pressure coefficient, C_e is an exposure coefficient, C_t is a topography coefficient, C_{dir} is a directional coefficient, C_i is an importance factor, C_{other} is a factor accounting for other effects such as hurricane zone shielding or return period, and q is a dynamic pressure obtained using:

$$q = \frac{1}{2}\rho v^2 \quad [5.2]$$

where, ρ is a density of air and v is the far field velocity obtained from the wind maps. Design codes stipulate how a building must interact with the wind, based on different environments that it is in for a set of probabilistic wind speeds, which may change depending on the selection of coefficient factors. However, the most impactful variable in Eq. (5.1) comes from the dynamic pressure in Eq. (5.2), specifically the wind speed, v. The American Society of Civil Engineers' (ASCE) minimum design loads for buildings (*93*) derive this speed using various probabilistic climatic models, which aim to predict development and dispersion of hurricanes based on average historic wind speeds data [Fig.5-1]. Due to this averaging approach and the probability of the same extreme event occurring in the same region on two occasions leads to an infrequent update of these maps. In fact, after one of the most devastating hurricanes of the last decade of the 20th century, hurricane Andrew in 1992, it took the state of Florida almost a decade to revive the ASCE minimum design codes. However, the problem also lies beneath the selection of adequate coefficient for Eq. (5.1). ASCE minimum safety design codes distinguish between low and high rise buildings with much more emphasis given to understand wind loads for tall buildings (*95*, *99*, *160*, *161*) and the impact that might have on the surrounding environments of lower rise buildings (*159*). For low rise buildings, to identify the right set of coefficients, ASCE codes distinguish between different types of flow regimes, which can be found in cities, suburban and rural areas

(*93*, *94*, *159*, *162*). They also account for different characteristic building sizes, shapes, and heights. Lastly, depending on the purpose and occupancy of the building, the wind load limits may be higher or lower; for example, warehouses have lower C_i than residential houses, which have lower C_i than condo/apartment buildings. In the end, the code standards work well for lower and mid-range category hurricanes, but for the upper range, historical damage data in the US (*40*) has showed that for residential houses, recorded hurricane speed measurements, do not always translate to the damage that hurricane's wind speed should lead to with the ASCE standards. An example would be 2018 category 4 hurricane Michael that struck the town of Mexico Beach in Florida leaving many of the low rise, residential detached houses demolished, which is the type of damage that one would be expect for category 5 hurricane.

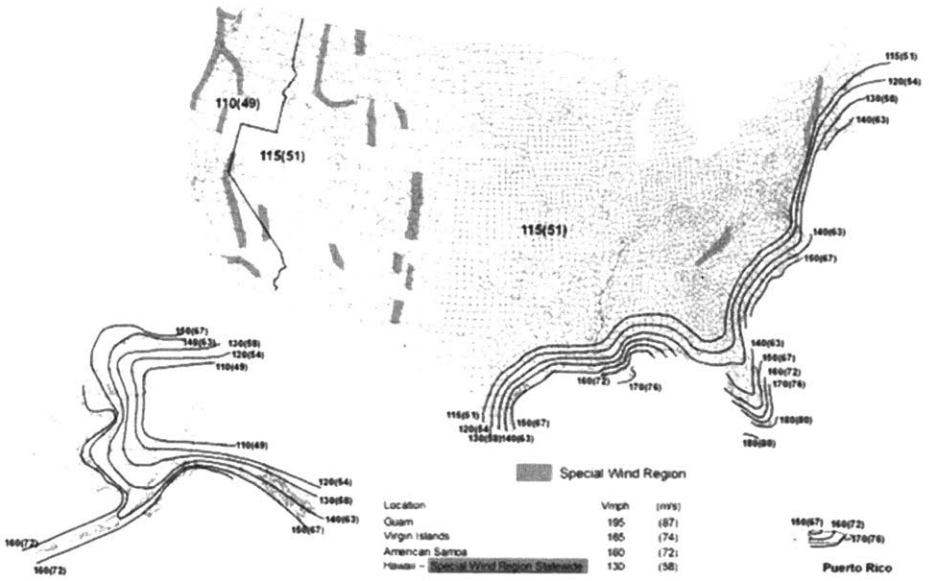

FIG.5-1 US ASCE Building Design Code Wind Speed Map (*93*)

5.1.1. Categories of Hurricanes

Saffir-Simpson Hurricane Wind Scale is used to define hurricane categories (*163*), which are ranked from 1 to 5:

- Category 1 has wind speeds 119-153 km/h, which results in damaged roofs, shingles, vinyl siding and gutters.
- Category 2 has wind speeds 154-177 km/h, which results in major roof and siding damage.

- Category 3 has wind speeds 178-208 km/h, which results in major damage or removal of roof decking and gable ends.
- Category 4 has wind speeds 209-251 km/h, which results in severe damage with loss of most of the roof structure and/or some exterior walls.
- Category 5 has wind speeds higher than 252 km/h, which results in total roof failure and wall collapse.

Residential damage in Mexico Beach, FL exceeds damage expected with Category 4 hurricane, despite the fact that far field wind speeds were below 251 km/h. This suggests that locally those wind speeds must have been higher and that current coefficient factors are not adequate for low-rise residential buildings, which for failure simulations are assumed to have a maximum fixed value of 2 (*93*).

5.1.2. Flow Regimes in Cities

The impact of local urban texture on wind flow has been studies for decades with the earliest work going back to 1970s (*101*). It is a known phenomenon that different size of urban canyons—defined by the ratio of building height, H to street width, W—result in different types of flows, which have been categorized to 3 main ones (*101*, *102*, *106*):

- Isolated roughness flow ($H/W \leq 0.3$), which assumes to neglect the impact of neighboring buildings
- Wake interface flow ($0.3 < H/W < 0.7$), which results in chaotic and unpredictable turbulent flow in between the buildings.
- Skimming flow ($H/W \geq 0.7$), which results in a somewhat predictable turbulent flow with a dominating primary vortex in between the buildings.

However, urban canyons have another dimension along the street, which can significantly increase the speed of wind flow for higher ratios of H/W. The local wind flow, although may be very complex, has been correlated to the impact on the flow has been correlated with 2D planar density, λ_p of buildings (*104*, *105*), defined as the ratio between area of building footprints and the total area of land they occupy. Most cities are known to have $0.1 < \lambda_p < 0.63$ (*106*), where the upper limit seems to be a natural limit for the packing density of buildings; once that limit is reached the

city's growth is forced in the vertical direction. To account for the vertical impact on the flow, instead of λ_p, which omits the impact of H, it is possible to correlate wind flow with frontal density, λ_f (*104*, *107*, *112*), which is defined as the ratio between exposed to the flow area of the building's wall and the area of the land it occupies. Although, wind flow is also known to vary depending on its direction (*109*, *164*), or variability in heights (*103*, *109*, *165*), most of the work in the field has been associated with studying densities of buildings, whether planar or frontal.

5.1.3. Wind Pressure Loads

These densities are known to influence the flow, which can be quantified using a single flow coefficient, C_d, which is part of the drag pressure equation:

$$P_{wind} = \frac{1}{2}\rho v^2 \times C_d \qquad [5.3]$$

When compared to Eq. (5.1), the drag coefficient thus becomes:

$$C_d = C_g \times C_p \times C_e \times C_t \times C_{dir} \qquad [5.4]$$

where, C_i and C_{other} are ignored as they are dependent on building's purpose and thus independent of its structure. Drag coefficients are fixed, dimensionless values which capture object's resistance to a fluid passing around it. Highly aerodynamic objects, streamlined bodies, such as modern cars or planes have very low C_d values, typically below 0.5. On the contrary, boxy objects with large frontal surfaces, such cubic buildings, have drag coefficients as much as 1.2. These values, although may change as the speed of the flow increases, under stable flow conditions generally do not vary significantly (*100*). However, they have been found to vary with λ_p (*104*) or λ_f (*110*) in the range from 0.5 to as much as 20 (*166*) for cubes, which resemble the characteristic shape of buildings, which neglect the impact of roofs, which would make the object more aerodynamic resulting in a lower C_d. However, most of the models tested in wind tunnel experiments or using

Computational Fluid Dynamics (CFD) simulations, models used to derive the correlations between C_d and different density parameters, rely on regular or staggered grid configurations of buildings (*103–105*, *167*), which do not resemble complex, disordered configurations of buildings in real cities [Figs.2-1 and 2-4]. Although, some work has been done to study flow in realistic city-like environments (*99*, *147*), they have been focused on specific parts of cities with low quantities of buildings insufficient to be able to derive quantitative guidelines that could be applied to predict drag coefficients of buildings in any city-like environment.

5.2. Fluid Dynamics of Flow

To model flow of air in city-like environments, to understand the flow of air around buildings and its impact on P_{wind}, wind flow experiments with scaled realistic structures is going to provide the most accurate results. However, changes to the direction, shapes, distances between buildings makes this method inadequate for modeling multiple types of flow in different environments. Moreover, wind-tunnel experiments are costly and time consuming. However, due to their high accuracy, wind-tunnel experiments have been widely used to verify the accuracy of numerical simulations, which in the context of flow of fluids, herein wind, utilize computational fluid dynamics simulations to solve Navier-Stokes equations.

The Navier-Stokes equations describe the motion of fluid by describing the 3D relationship between velocity, temperature, pressure, and density through a set of continuity, momentum and energy equations (*168*). Continuity equations with the conversation of mass states that:

$$\frac{\partial \rho}{\partial t} = -\nabla \cdot (\rho \mathbf{u}) = -\mathbf{u} \cdot \nabla \rho - \rho \nabla \cdot \mathbf{u} \qquad [5.5]$$

where, ρ is the density of the fluid, t is time, vector $\mathbf{u} = (u, v, w)$, and ∇ is divergence. For an incompressible fluid, Eq. (5.5) can be reduced to:

$$\frac{\partial \rho}{\partial t} = -\rho \nabla \cdot \mathbf{u} \qquad [5.6]$$

Conservation of momentum is defined as:

$$\frac{\partial \mathbf{u}}{\partial t} = (\mathbf{u} \cdot \nabla)\mathbf{u} - \frac{1}{\rho}\nabla P + \frac{F}{\rho} + \nu \nabla^2 \mathbf{u}$$

[5.7]

where, P is pressure, F is the body force, and ν is the kinematic viscosity defined as the ratio between dynamic viscosity, μ, and density:

$$\nu = \frac{\mu}{\rho}$$

[5.8]

When expanded for x, y and z directions conservation of momentum Eq. (5.7) becomes:

$$\rho\left(\frac{\partial u}{\partial t} + \frac{\partial u^2}{\partial x} + \frac{\partial uv}{\partial y} + \frac{\partial uw}{\partial z}\right) = -\frac{\partial P}{\partial x} + F_x + \mu\left(\frac{\partial^2 u}{\partial x^2} + \frac{\partial^2 u}{\partial y^2} + \frac{\partial^2 u}{\partial z^2}\right)$$

[5.7.1]

$$\rho\left(\frac{\partial v}{\partial t} + \frac{\partial uv}{\partial x} + \frac{\partial v^2}{\partial y} + \frac{\partial vw}{\partial z}\right) = -\frac{\partial P}{\partial y} + F_y + \mu\left(\frac{\partial^2 v}{\partial x^2} + \frac{\partial^2 v}{\partial y^2} + \frac{\partial^2 v}{\partial z^2}\right)$$

[5.7.2]

$$\rho\left(\frac{\partial w}{\partial t} + \frac{\partial uw}{\partial x} + \frac{\partial vw}{\partial y} + \frac{\partial w^2}{\partial z}\right) = -\frac{\partial P}{\partial z} + F_z + \mu\left(\frac{\partial^2 w}{\partial x^2} + \frac{\partial^2 w}{\partial y^2} + \frac{\partial^2 w}{\partial z^2}\right)$$

[5.7.3]

Conservation of energy equation states that:

$$\frac{\partial s}{\partial t} = -\mathbf{u} \cdot \nabla s + \frac{Q}{T}$$

[5.9]

where, T is temperature, Q is the heat transferred and s is the entropy per unit of mass. In practice these equations are solved using finite difference, element, or volume methods using CFD

simulations. In order to solve the Navier-Stokes equations, an equation of state is coupled with them. In addition, stress tensor values must be defined, which depending on the selected approach, generally are approximated with a CFD turbulence model. To distinguish between different types of flow: laminar and turbulent, we resort to utilizing a Reynolds number:

$$\mathrm{Re} = \frac{\rho u L}{\mu} \qquad [5.10]$$

where L is characteristic length scale of the object inside the fluid and u is the velocity of fluid with respect to the object. $\mathrm{Re} < 2100$ is characteristic of the laminar flow, and $\mathrm{Re} > 4000$ is generally considered to be turbulent, but for a fully turbulent flow one would expect to see $\mathrm{Re} > 10^4$. Transient flow occurs when Re number is between those characteristics of laminar and turbulent flows. In the context of flow of fluid in cities, specifically hurricanes, we identify that $\mathrm{Re} \gg 10^4$ leading to a highly unsteady and turbulent flow. Therefore, for proceeding CFD simulations we resort to using a turbulent model.

5.2.1. Computational Fluid Dynamics of Flow (*168*)

There are 3 approaches for solving turbulent flow Navier-Stokes equations using CFD simulation:

- Direct Numerical Simulations (DNS) numerically solve the full set of unsteady fluid flow equations. Being the most computationally expensive out of the three, this method rarely finds a practical application.
- Scale Resolving Simulations (SRS) resolve large eddies in time-dependent simulations using filtered Navier-Stokes equations, where filter is intended to remove eddies smaller the mesh size. Filter equations vary between different CFD packages. SRS include Large Eddy simulations (LES) models and after DNS offer the highest level of accuracy (*144*). This approach, although not as computationally expensive as DNS, is still too expensive for most practical applications.
- Reynolds-Averaged Navier-Stokes Simulations (RANS) (*144*) solve time-average Navier-Stokes equations with the whole range of the scales of turbulence being modeled. Unlike,

DNS or SRS, due to its averaging modeling approach RANS can provide steady state solutions. This leads to less accurate results than SRS, however, it greatly reduces the required computational resource and therefore, is widely adopted for most practical engineering applications. The models range from one equation and various two equation models to a most complete classical turbulence Reynolds Stress model. The main difference between different RANS models is how they model the Reynolds Stress tensor, which can be done using an eddy viscosity (very reasonable and highly utilized approach for simple turbulent shear flows), or through transport equations, which although increase the computational time, lead to more accurate turbulent modeling. For many general applications, with an appropriate size of CFD mesh/grid, a method with increased computational cost is likely to lead to greater accuracy of results.

SRS and RANS models are offered by many CFD software packages, which can be categorized into four major groups: (1) open-source that allow users to modify the code, (2) CAD CFD-add-ons, (3) specialty packages focused on specific applications, and (4) comprehensive packages that have been the industrial standard for CFD simulations, such as Fluent, Star-CCM+, or COMSOL. While some of the packages may be suited better for specific applications, here, we resort to a well-established ANSYS Fluent package by obtaining an academic license.

5.3. City Texture Wind Simulation

In preparation for CFD simulations, we adopt an envelope simulation configuration based on height of buildings (*103*, *109*, *110*), which offers sufficient distances between inlet and building, building and outlet, and buildings and top of the envelope, to allow the turbulent flow to fully develop and establish its characteristic unique patterns. The approach is exemplified in Fig.5-2. With defined geometry for buildings, envelope, inlet and outlet, we proceed to create mesh for the simulation. We use ANSYS Mesh tool to generate an appropriate mesh configuration. To avoid any issues when generating mesh for a system with buildings that have neighboring buildings at distances <5m, we use virtual topology with "high" behavior with simplified faces and merged face edges. However, this still may create overlapping and conflicting regions, which we can eliminate manually by checking for overlapping regions. Then we can select mesh specifications.

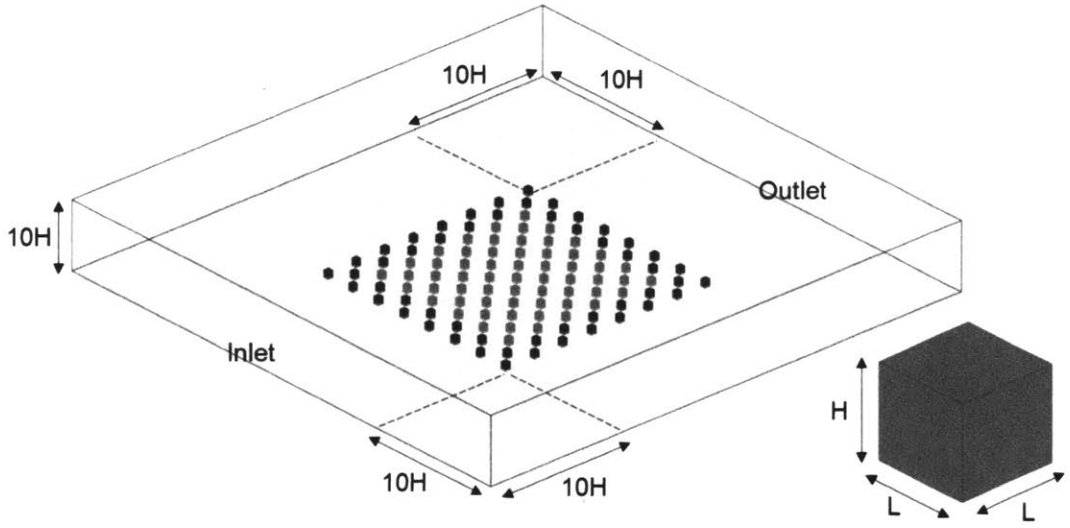

FIG.5-2. CFD model set up. Diagram of the simulation envelope adopted for CFD simulations.

First, we choose the default CFD physics preference and Fluent for solver preference. Element order is selected to be linear with the default size. We use "mesh defeaturing", "capture curvature", and "capture proximity" options, all with default sizes, in order to create enough nodes around edges of the system for the CFD solver to provide accurate results. We use double precision solver and select a standard ANSYS Fluent viscous turbulent model.

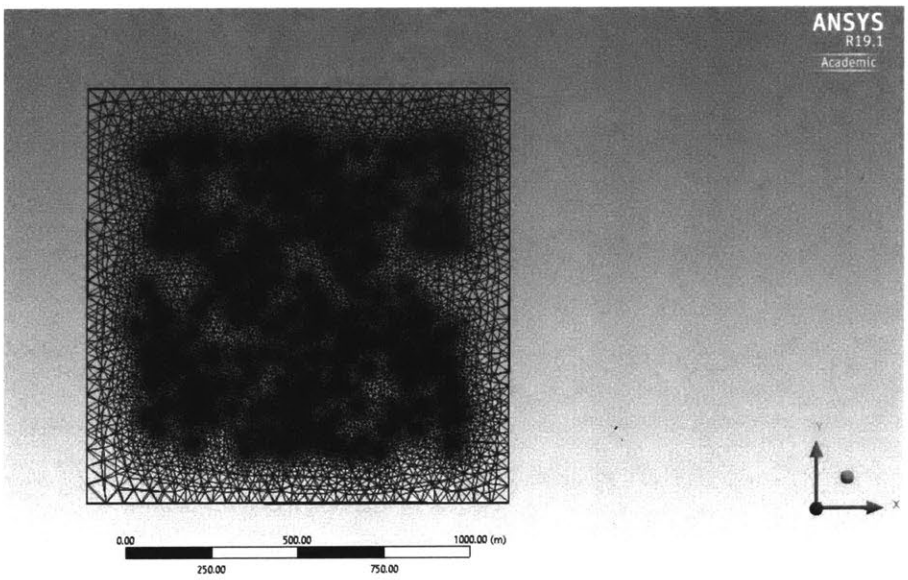

FIG.5-3. CFD Mesh. Visualization of example mesh configuration adopted for CFD simulations.

5.3.1 CFD Model set-up

As previously explained for Large Eddy Simulation (LES) models provide the most accurate results from CFD simulations (*144*, *146*, *161*), however, it is the most computationally expensive model. In fact, LES can be orders of magnitude longer than other turbulent CFD models. Therefore, when conducting hundreds of simulations, it might be better to choose a less accurate model, but one that would still provide adequate results. Yet, in this study because we are using relatively simple structures with cuboids of different sizes and relatively small number of buildings, it is worth investigating performance of an LES model and comparing it to a most accurate RANS approach, that is one with the Reynolds Stress Model for turbulence.

In ANSYS Fluent, for LES we choose a subscript-scale Kinetic-Energy Transport model treatment, wall boundary conditions and reflection effects for Reynolds-Stress options. We use default ANSYS Fluent parameters for model constant. We choose SIMPLE pressure-velocity coupling solution method with the following specifications for the special discretization: least square cell-based gradient, second order pressure, bounded central differencing momentum and the second order upwind subgrid kinetic energy. For transient formulation we choose the second order implicit option.
We choose a Reynolds Stress Quadratic Pressure-Strain Model with enhanced wall treatment and wall reflection and boundary conditions effects for the RANS model. We use default ANSYS Fluent parameters for model constant. A SIMPLE pressure-velocity coupling solution method with the following specifications for the special discretization is selected: least square cell-based gradient, second order pressure and second order upwind momentum turbulent kinetic energy, turbulent dissipation rate and Reynolds Stresses.

For the inlet zone, we select standard turbulent intensity of 5% with 10% viscosity ratios for the turbulence generation in order to generate turbulent flow within the inlet region. Inlet is investigated on each side of the envelope to allow us to understand the impact that direction of the flow has pressure and wind speed for different city textures. Outlet is defined to be always positioned opposite to the inlet. We run the simulation until error residuals are $< e^{-2}$ and converge to a uniform value, which for set of samples is < 10,000 iterations. With average sizes between 9-

15m building retain the scale of their real size. Therefore, to model high speed hurricane, we select dynamic viscosity of air, $\mu_{air} = 1.825 \times 10^{-5}$, density of air, $\rho_{air} = 1.225\, kg/m^3$ and inlet velocity to be 70 m/s (cat. 5 hurricane), which translates to realistic high Reynold numbers, Re equal to approximately 6×10^7 characteristic of turbulent flows.

5.3.2. CFD Model set-up validation

We test both configurations for a regular grid model that has been previously tested in a wind-tunnel experiment (*113*) and using other CFD experiments (*103*). We compare the results from LES and RANS simulations m and find that they resemble results from previous studies [Fig.5-4]. In particular, we find that streamwise velocity for both LES and RANS follow closely the distribution obtained from wind tunnel experiments [Fig.5-4.a]. Above building height, vertical velocities are also close to wind tunnel experiments, but below the building height (z/H<1), both LES and RANS deviate slight from wind tunnel measurements, which suggests that mesh configuration could be improved (*144*, *147*, *167*), however, overall both flows lead to the distributions that follow the correct trend. On the contrary, for the turbulent kinetic energy (TKE), below the building height herein tested LES model captures well turbulent energy fluctuations like those in a wind tunnel experiment, but above the building height decreases when compared to them. This can be explained by the mesh defeaturing option, which optimizes the mesh inside the envelope by increasing the space between nodes where there are object around, thus averaging out TKE values. Here, however, the focus is on capturing high accuracy of the flow between buildings to derive pressure and velocity for z/H<1, which the current LES model does sufficiently. For the RANS simulation, we identify that TKE distribution is underestimated when compared to LES for z/H<1, while for the heights above the building, it matches LES distribution. Although, LES resembles more closely wind tunnel experiment, RANS model provides sufficient accuracy for the purposes of this work, which aims to identify average wind pressure loads acting on buildings in different city-like environments. Finer mesh, or different mesh model, could improve the accuracy of results for both LES and RANS, it would significantly intensify the computational time (6-10 times) for 148 simulations (37 configurations with 4 separate locations of inlets/outlets) we choose to continue with the previously explained methodology.

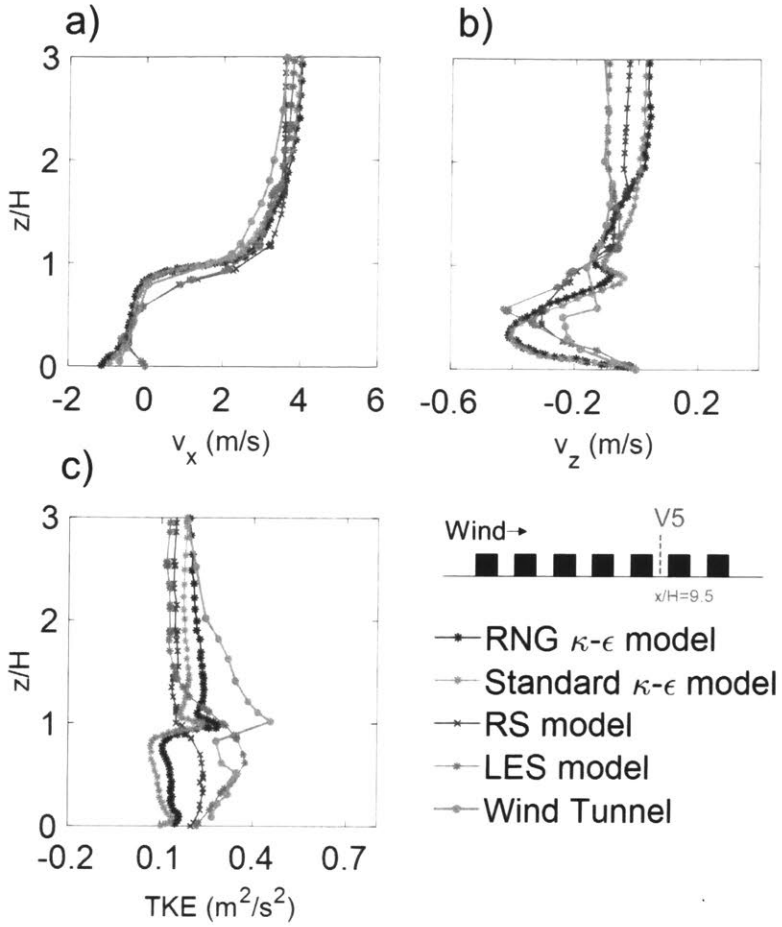

FIG. 5-4. CFD Approach Verification. Comparison of CFD ANSYS Fluent (*169*) LES and RANS Reynolds Stress (RS) Method setup with a Wind Tunnel experiment (*113*) and RANS RNG κ-ϵ and Standard κ-ϵ (*103*) CFD simulations for a) streamwise and b) vertical velocities, as well as c) turbulent kinetic energy.

5.4. City Texture influenced Drag Coefficients

We export CFD pressure and velocity values to calculate drag coefficients for buildings. For each building we calculate average velocity of air surrounding that building using each value obtained from the simulation by using scaled by a factor of 2 area of that building, excluding velocity values for that building (*103*, *164*, *166*). We limit our sample to the heights of building, that is values for heights $\leq H$, as depicted in Fig.5-5 and average all the time-spatial values for velocity, extracted directly from simulation results (*169*). Then we proceed to calculate average pressure difference, Δp_{f-b}, between the upwind and downwind surfaces of the buildings where, p_f and p_b are average pressure on the frontal and back walls [Fig.5-5], respectively, of the building, extracted from CFD

simulation results. We calculate these values for each of the buildings in each simulation to derive drag coefficients C_d (*166*) using the drag force, F_d equation:

$$F_d = \frac{\rho_{air} C_d v^2}{2A} \qquad [5.11]$$

where, ρ_{air} is the density of air assumed to be 1.225 kg/m^3, A is the frontal area of the object exposed to the flow, as v is the velocity of fluid around the object of reference (*107*, *166*). In order to account for the directional impact of the flow on the local building pressure, we define C_d to be the maximum from all tested sides [Fig.5-6]. Such defined C_d is captured using the following equation:

$$C_d = \max_{1:4} \left[\frac{2\Delta p}{\rho_{air} \times v^2} \right] \qquad [5.12]$$

where, C_d is selected to be the maximum value from a sample of 4 measurements, each one with different inlet direction: north, south, west, east.

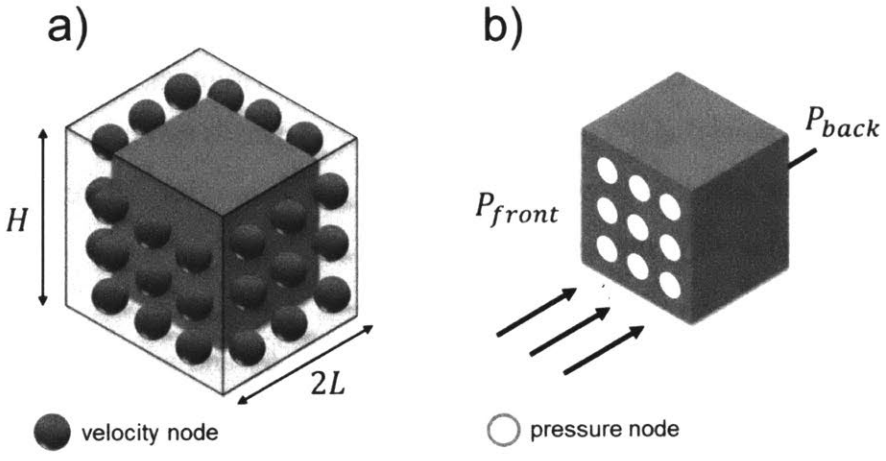

FIG.5-5. Drag Coefficient Data. Diagram of simulation results for a) velocity and b) pressure nodes used in derivation of drag coefficients.

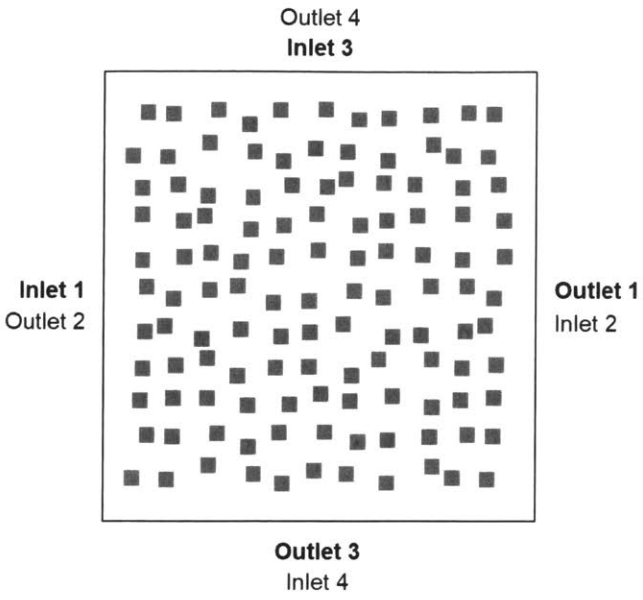

FIG.5-6. CFD Inlets and Outlets. Visual depiction of directional flow simulations.

In order to be able to identify if there is the local order captured by the local parameter, φ, has any influence on individual drag coefficients, C_d, we look at CFD samples with fixed average area densities for grid and staggered configurations [Fig.5-7]. We find that there is no direct relationship between φ and C_d neither for regular grid disordered configurations with $\rho_{CFD}^{area} = 0.2$, nor staggered grid configurations with $\rho_{CFD}^{area} = 0.1$ for fixed building sizes. It appears, however, that is a correlation between the peaks in φ distributions [Fig.5-7.c] and peaks in the C_d distributions [Fig.5-7.d], where higher proportion of φ values leads to a higher proportion of C_d values. While it is difficult to obtain similar conclusion for the regular grid disruption, it is noticeable that two peaks in the φ distributions [Fig.5-7.a, models 1 and 3] translate to two peaks in the distribution of C_d [Fig.5-7.b, models 1 and 3]. However, more CFD simulations for different φ are needed in order to be able to conclusively correlate C_d with φ.

We are unable to identify any type of relationship between C_d and area density for individual buildings, as in previous studies that would correlate average C_d with average area density of the sample (*107*, *166*). However, we are able to recover previously studied relationships between C_d and frontal density, λ_f, but in the format the incorporates local texture parameters:

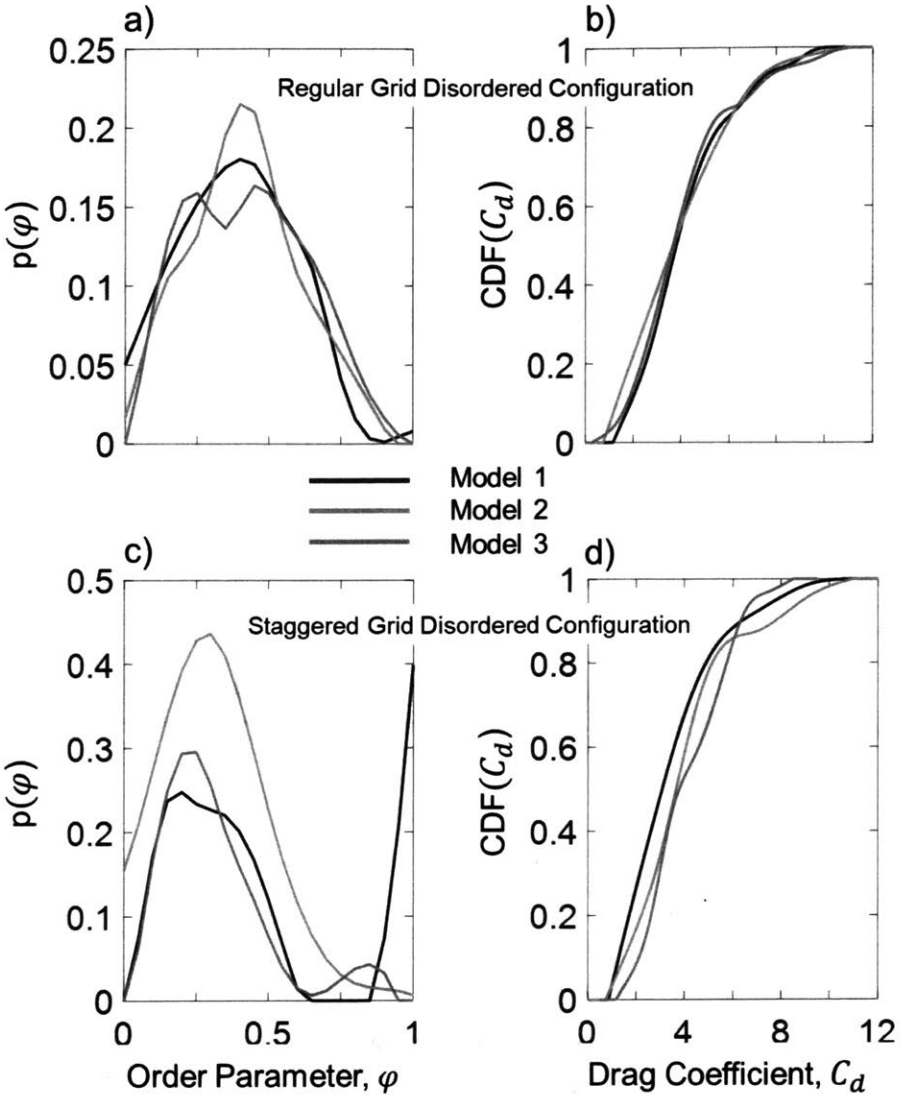

FIG.5-7. CFD Order Parameter Results. Diagram of simulation results for a) velocity and b) pressure nodes used in derivation of drag coefficients.

$$C_d = C_n \lambda_f^{1/2} + C_{d,0}$$

[5.13]

where, $C_{d,0}$ is a drag coefficient of a cubic box (*100*), assumed to be 1 and λ_f is calculated using the following equation:

$$\lambda_f = \frac{(C_n + 1) \times L_{local} \times H}{\pi R^2}$$

[5.14]

where, L_{local} is the local building size averaged for all building found within distance R from the center point of the building of reference; R is the radius obtained using $g(r)$, specifically using Eq. (3.6). Thus, for fixed building size, drag coefficient for individual buildings becomes:

$$C_d = C_n \lambda_f^{1/2} + C_{d,0} = C_n \times \left(\frac{(C_n + 1) \times L_{local} \times H}{\pi \left(1.35 \times R_{peak}^{g(r)}\right)^2} \right)^{1/2} + C_{d,0} \quad [5.15]$$

But, using the integral of the first peak of $g(r)$ disturibiton we can approximate C_n and subsequently derive an average $\bar{C}_d$ for a city using in the following form:

$$\bar{C}_d = 2\pi\rho_{city} \int_0^{R_{min}} r g(r)\, dr \times \left(\frac{\left[2\pi\rho_{city} \int_0^{R_{min}} r g(r)\, dr + 1\right] \times L \times H}{\pi {R_{min}}^2} \right)^{1/2} + C_{d,0} \quad [5.16]$$

where, L is average building size derived using Eqs. (3.2) and (3.6). However, in these forms Eqs. (5.15) and (5.16) the correlation only holds true for configurations with fixed building sizes. For CFD samples with log normally distributed building sizes, we find that using the first peak to identify R_{min} and ultimately C_d does not work. This is because R_{min} for samples with different building sizes leads to average $C_n < 4$ (the expected value for the first shell of neighboring buildings for an ordered configuration of buildings [Fig.3-7]), leading to underapproximating values for C_d due to incorrect local texture parameters. To overcome this challenge, instead of using R_{min} to obtain R, we use a 3.5 multiplication factor of L (which leads to average $C_n = 4$) to obtain:

$$\lambda_f = \frac{(C_n + 1) \times L_{local} \times H}{\pi (3.5L)^2} \quad [5.17]$$

We incorporate this to the modeled drag coefficient equation to derive:

$$C_d = C_n \lambda_f^{1/2} + C_{d,0} = C_n \times \left(\frac{(C_n + 1) \times L \times H}{\pi (3.5L)^2}\right)^{1/2} + C_{d,0} = \alpha C_n \times \left((C_n + 1) \times \frac{H}{L}\right)^{1/2} + C_{d,0}$$

[5.18]

where, $\alpha = 3.5^{-1}\pi^{-1/2} = 0.16$. At the city scale this translates to an average $\bar{C}_d$ equal to:

$$\bar{C}_d = 2\pi\rho_{city} \int_0^{3.5L} rg(r)\, dr \times \left(\frac{\left[2\pi\rho_{city} \int_0^{3.5L} rg(r)\, dr + 1\right] \times L \times H}{\pi (3.5L)^2}\right)^{1/2} + C_{d,0}$$

[5.19]

Using the scaling relationship between C_n and φ [Fig.3-8], we could replace the coordination number with the local order parameter. Since φ decreases as C_n increases, we would expect that for more disordered cities with lower φ, we would expect to see higher C_d values. However, at the same time, for a highly ordered sample of buildings, we find that more neighboring buildings can be found for a fixed R_{min}. This suggests that higher ordered cities, due to their higher local packing density of neighboring buildings, we would expect to see higher C_d values.

Using the city texture drag coefficient model captured with Eq. (5.13), we can re-define the wind pressure drag equation:

$$P_{wind} = \frac{1}{2}\rho_{air} v^2 \left(C_n \lambda_f^{1/2} + C_{d,0}\right)$$

[5.20]

where the C_n component of $C_n\lambda_f^{1/2}$ of the equation is obtained using local city texture parameters of neighboring buildings that are within a specific distance to the reference building; if there are none neighboring buildings, $C_n\lambda_f^{1/2} = 0$ and $C_{d,0}$ is the sole, single building drag coefficient.

Using a sample size of 2,935 buildings, we identify that using Eqs. (5-15) and (5-18), we derive modeled drag coefficients C_d' and compare them to measured C_d using CFD experiments [Fig.5-8]. We find that the model has many outliers, which are lognormally distributed. Using the distribution [Fig.5-8 inlet], we identify points outside the zone defined by the distance of one standard deviation, σ from the mean of the distribution, to find that 2,012 (68% of data) measured and modeled points have the coefficient of correlation of $R^2 = 0.65$ for the direct relationship of $C_d = C_d'$. If we increase the range to 1.5σ away from the mean, we increase the sample size to 2,534 (86% of data), we find that the correlation reduces to $R^2 = 0.42$.

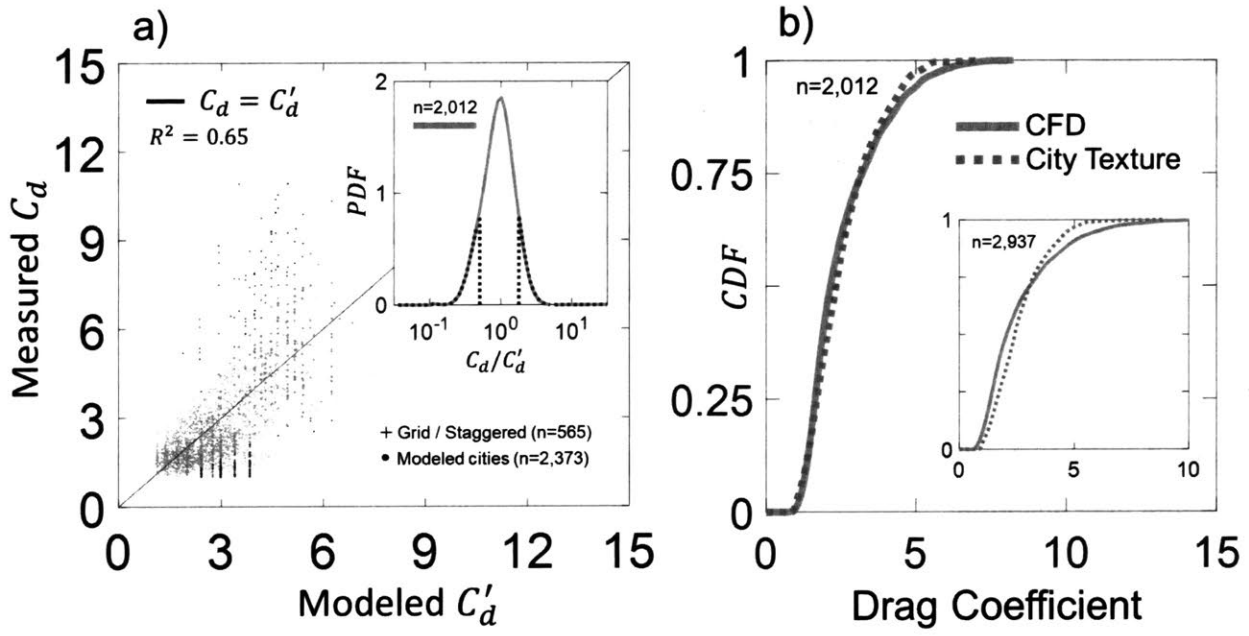

FIG.5-8. Drag Coefficient CFD Results. Results showing a) linear correlation between measured and modeled drag coefficients with an inlet showing the distribution used to identify the correlation; b) comparison between distributions of CFD measured and city texture modeled drag coefficients.

The variability in modeled and measured results can be explained for several reasons. First, there is a significant variation in the distribution of building sizes, L, density, ρ and number of neighbors

C_n, which for tails of the distributions [Fig.5-9] leads to inaccurate C_d' values. Furthermore, due to the simplicity of the model, normalization area needed to obtain λ_f on occasions may be underestimating the real area with averaged L extending buildings—assumed to have a square footprint—to be outside of boundaries of the circle imposed by the radius R_{min}. On the other hand, a specific R_{min} may also have parts of buildings present, without them being counted as neighboring buildings, since their center of mass wouldn't be inside the circle. However, there is another challenge, which is the accuracy of the mesh. Although, for most buildings CFD simulations provide (almost) symmetrical mesh, for some cases issues non-symmetrical mesh may lead to inaccurate values and thus increased C_d values (Eq. (5.12) wouldn't lead to lower values).

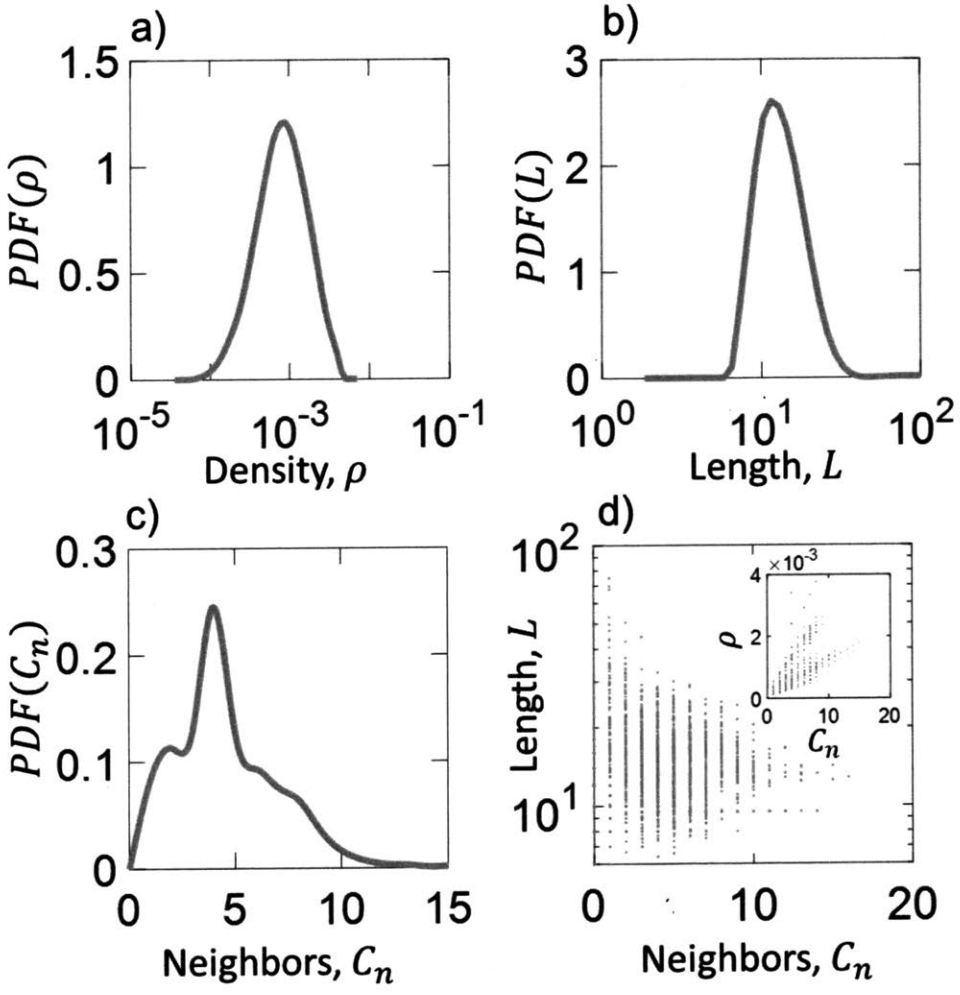

FIG.5-9. Drag Coefficient City Texture Statistics. Derived model parameters for 2,935 buildings showing probability density functions for a) density, b) building length, c) number of neighbors and d) the relationship between building length and number of neighbors, and density and number of neighbors (inlet).

Results visualized in Fig.5-9 can be analyzed further to recognize that the characteristic cluster size of 4 neighbors [Fig.5-10] can be used to define the city texture effect for building C_d values. Density and building length values act as limits for the model, for which it has been validated. We find that building length L and neighboring buildings C_n are independent variables by quantifying their covariance:

$$\mathrm{cov}(L, C_n) = E[(L - E[L])(C_n - E[C_n])] \qquad [5.21]$$

which for 2,935 values is very low, equal to -2.9. With two independent variables that are needed to quantify λ_f, we can conclude that Eqs. (5-16) and (5-19) can be derived with solely $g(r)$.

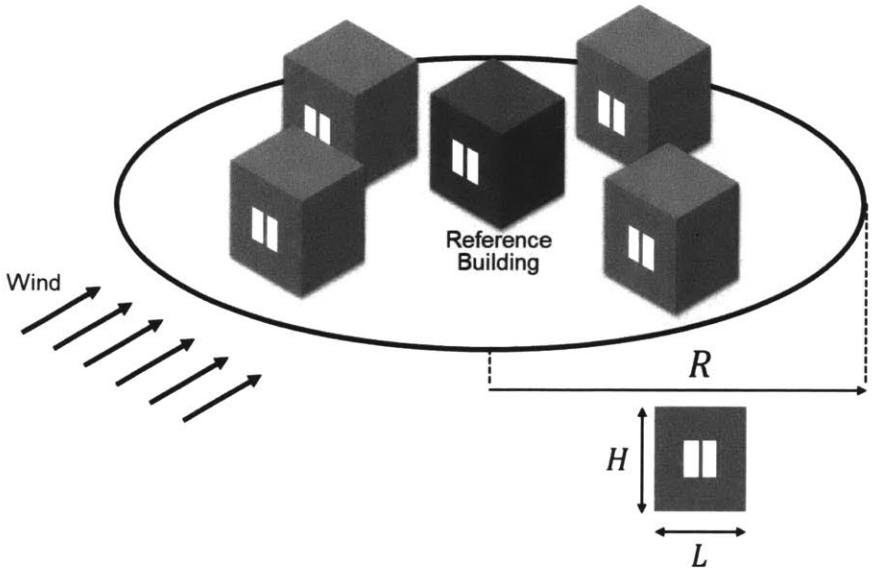

FIG.5-10. Characteristic City Texture.
Visualization of a typical local cluster of 4 neighbors for modeled buildings.

5.4.1. Validation

The validation process, first and foremost begins by identifying the relationship between modeled and measured drag coefficients. We find that a simplistic statistical model that accounts for local geometries can accurately predict drag coefficients obtained using a comprehensive ANSYS

Fluent CFD software package by adopting previously established tools in quantifying drag coefficients C_d, frontal densities λ_f, as well as the local number of neighboring buildings C_n. In addition, both modeled and measured values of C_d in their range are comparable to previously established drag coefficients for buildings in different grid configurations, which on average are 1.8-2, but can reach as much as 20 (*107*, *166*), which is within the same range as herein obtained values derived using CFD simulations [Fig.5-8.b].

5.4.2. Case Study: Mexico Beach, FL

To identify the accuracy of the model in a physical setting, we utilize damage data from 2018 Hurricane Michael for 416 buildings at Mexico Beach in Florida. We study the distribution of C_d' modeled using local city texture parameters, to identify that more than 55-70% of buildings in Mexico Beach had higher than the expected drag coefficients [Fig.5-11]. 77% of buildings have been severally damaged or destroyed, while 23% of building experienced minimal or no damage. Using the city texture model, we are able to identify damage with 67% accuracy by using a single parameter, C_d', derived with approximated building sizes, uniform heights and the quantity of local neighboring buildings (on average equal to 4 [Fig.5-11 inlet]), without any information about building heights, roof types, materials or landscape. We assume that building with $C_d' > 2$ are under the risk of city texture local pressure magnification effect and thus experience a severe damage.

This approach can be extended to predicting damage over time as the local city texture is changing, which may be done so by removing the building with the highest drag coefficient and recalculating the local city texture. We would repeat this process until every remaining building no longer has any local neighbors and thus all buildings have the same drag coefficients. However, beyond the necessity to incorporate building materials into the model (for more accurate wind load failure limitations), we would need to redefine Eq. (5-12) in order not to account for maximum drag coefficient values, but rather for average values not to overestimate the directional impact of the flow.

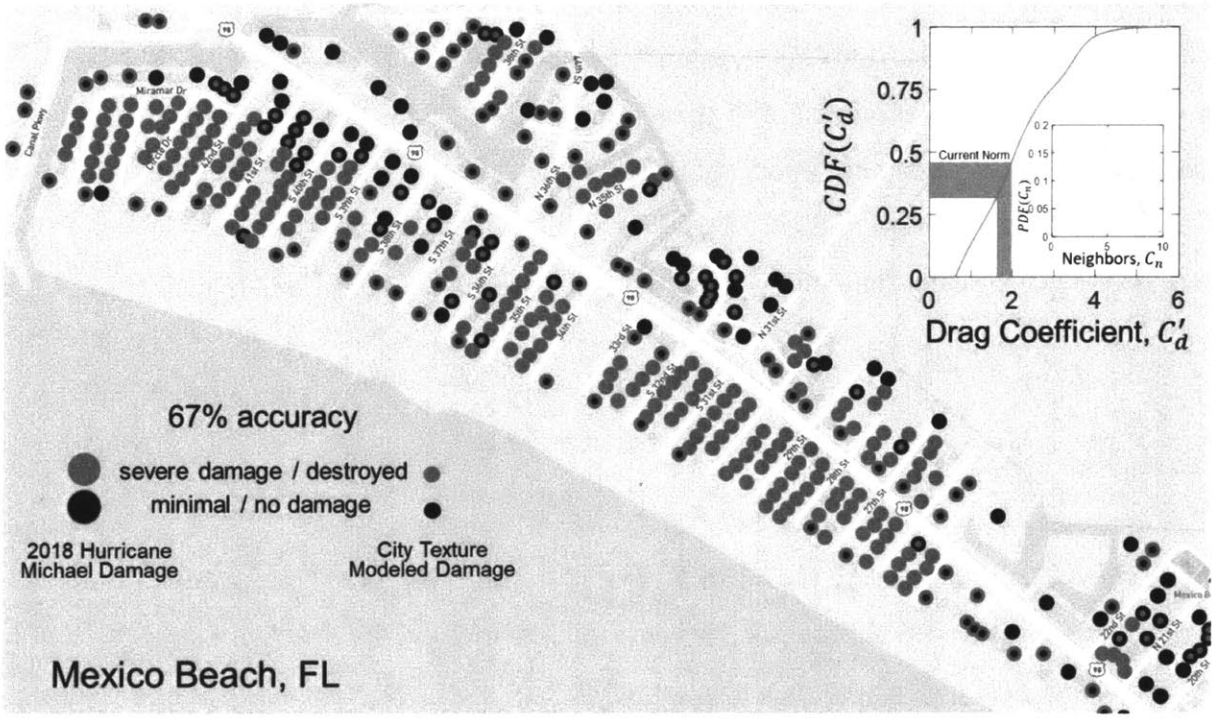

FIG.5-11. Mexico Beach Damage Map with inlets showing cumulative distribution function of modeled drag coefficients and probability distribution function of local number of neighbors.

5.4.3. Risk Assessment of Hurricane Failure

In order to create a method for assessing vulnerability of building failure during hurricane for any city, we need to make sure that we incorporate the right limits for selecting appropriate limits for two variables, which can influence the magnitude of drag coefficients. Due to relatively low number of buildings, CFD samples have much lower absolute (not relative) variability in two critical parameters L and λ_p. Average L is used to derive R_{min}, but for a city with 100s of thousands of buildings, the distribution of L is going to vary between suburban and more urban parts of the region, which could make selection of fixed R_{min} inaccurate for different neighborhoods in the same city. Thus, we propose a dynamic selection of R_{min} based on the limits of $g(r)$ equal to $15L$, where we define R_{min} for each building based only on the sizes of local buildings. In addition, we adopt a density limit for $\lambda_p < 0.63$ (*106*), to minimize overestimation of drag coefficient values with building sizes estimated based on their areas and assumptions that buildings have square area

footprints. In addition, due to unavailability of building heights data, we assume a fixed roof height equal to 9.5m as for CFD samples. With such approach we quantify drag coefficients for 21 OSM cities worldwide [Fig.5-12] and find that depending on the variability in density there are significant differences between different city textures. On average, we find that higher density cities, have average drag coefficients above the ASCE minimum design norms (if all buildings are treated as residential buildings). More interestingly, we identify that in the sample of 21 cities, the only 5 cities that have clear crystalline characteristics based on their $g(r)$ distributions are ranked in the top 8 greatest upper range C_d distributions and thus would have the highest risk of hurricane damage assuming that their buildings were built to the same norms and exposed to the same potential wind speeds. While these assumptions would not translate to real-life conditions, herein we present the theoretical model that quantifies the impact that city texture has on hurricane damage.

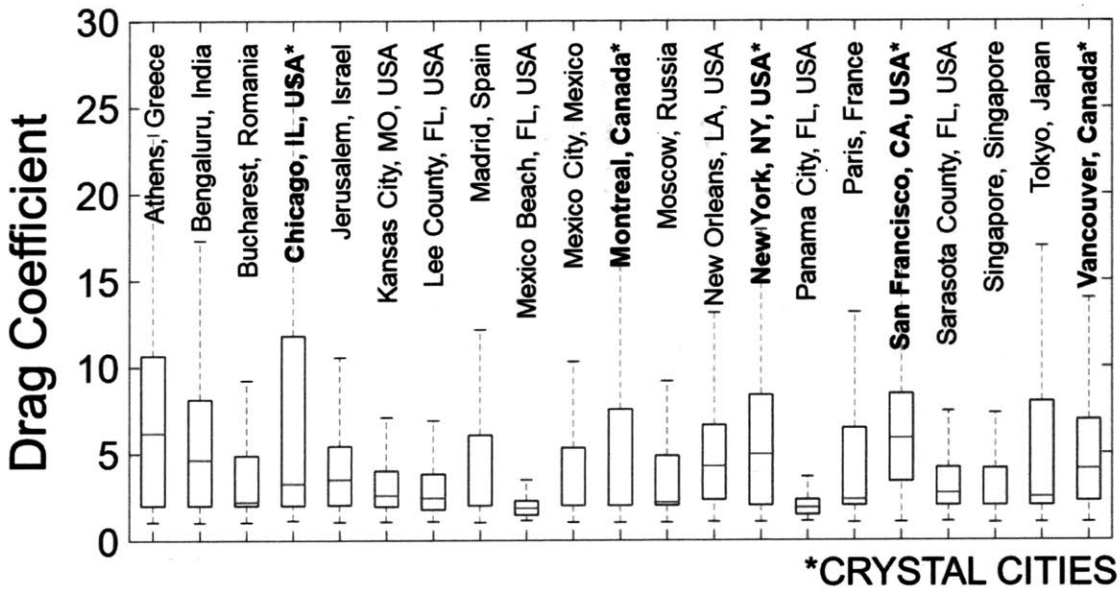

FIG.5-12. Modeled Drag Coefficients for GIS OSM cities.

To identify potential risk factors for residential buildings in areas with high risks of hurricane occurrence we use the same approach as for 21 OSM cities to identify drag coefficients for 5,970,242 buildings in the state of Florida [Fig.5-13]. We assess a maximum damage risk level, which accounts for any wind direction, by using 3 levels:

- Low: $C_d' \leq 2$
- Moderate: $2 < C_d' \leq 3$
- High: $C_d' > 3$

The risk assessment of this kind leads to over 40% of buildings in the entire state with drag coefficients exceeding current safety design norms using various coefficients [Eq. (5.1)] of residential buildings (*93*). This offers an easy and fast tool for people not only to identify buildings with the highest risk of failure, but also to build more resilient infrastructure by accounting for impacts of city texture locally with a standard safer than the current ASCE residential norms currently require.

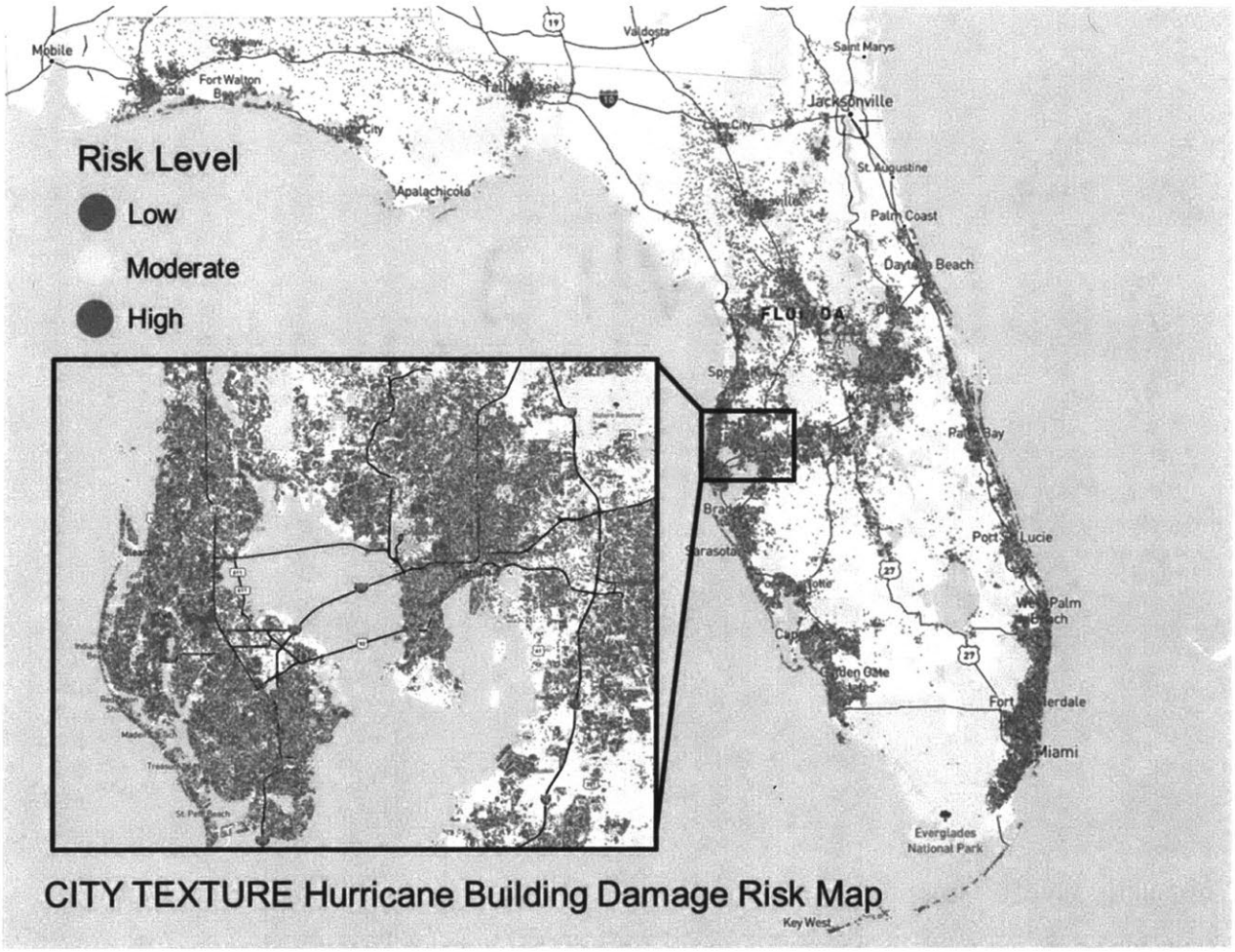

FIG.5-13. Drag Coefficient Hurricane Damage Risk Map for Florida.

5.5. Summary

In this chapter, we established a method for enhancing prediction of drag coefficients with local city texture values. We found that with the right set of limits, this method finds its applicability to predict more accurate drag coefficient for residential buildings, which could be applied to any city in the world. With more than 50% of buildings exceeding the safe design norm limits, we identified that the city texture model can be used to explain the severe damage in Mexico Beach during 2018 hurricane Michael. It could also be used to prevent damage with city or state-wide building hurricane damage risk maps.

Chapter 6

6. Conclusion

6.1. Significance and Impact

It is important to recognize that herein obtained values, which we used to derive city texture parameters, are averages obtained from GIS information for thousands of buildings with their shapes generalized to regular 3D cuboids (sometimes merged to form more complex shapes) with fixed heights. In real life, these shapes, while may not differ much on the façade side of a building, vary in terms of heights and roof shapes. In addition, since urban designs focus on various pragmatic aspects of sustainability, resilience and living comfort, they have components besides buildings that may affect flows in urban environments, whether is that of water during flooding, heat in the context of UHI, wind during hurricanes, or the spread and growth of fire. Cities are dynamic systems that rarely, if ever, are truly reflective of their designs done by a team of planners, engineers and architect. Rather, they are living communities that aim to optimize the equation composed of, aesthetics fit, access, vitality, sense, control and function (*128*) that evolve over the time. Unequivocally, the equation is of a complex form and solving it is a task that we are going to continue working on for generations to come. Interactions between spatial arrangements and urban agents that act as fundamental nodes of urban networks may be chaotic and isolated, smooth and connected, or be a combination of the two. Whatever the form they may take, they are always supported by a ring of externalities, some which are inevitable, but some that may well be controlled. Yet, however complex the urban form equation may be, by isolating building footprints from the equation, we were able to identify unique city texture for different cities world-wide, with gas-, liquid- and crystal-like textures. The last type of cities is only found in the North America (US and Canada [Figs.3-4 and 3-5]), where cities have history of grid-like streets (i.e. Chicago), which are not found on other continents, where historical growth of cities created more disorder (i.e. Paris). Beyond $g(r)$ calculations, we found that local texture characteristic can be used to provide further means of characterizing cities, necessary for their reconstruction in the form of

synthetic models with only a fraction of buildings that cities have, which may find their purpose in heat or fluid flow simulations.

6.2. Controlling Urban Heat Island

The Urban Heat Island phenomenon that intensifies urban air temperature when compared to their rural surroundings falls into the latter category. Our UHI analysis suggests that city texture plays a key role in determining its response to heat radiation phenomena and points to urban design parameters that can be modulated to mitigate UHI in planning and retrofitting of cities (*52*, *170*, *171*). In a broader context, our work suggests that tools and methods from statistical physics, at the right scale can provide means to quantitatively address the response of cities to climate. Our results complement previous studies on factors influencing day-time UHI (*63*). Observation that the causes of day- and night- time UHIs are fundamentally different corroborates that $\Delta T_{u-r}s$ at day- and night- time are uncorrelated (*172*). According to our findings, the increase of radiating surface area of cities is the main contributor to the nocturnal UHI. While large scale changes to already existing urban textures appear unrealistic, efforts of UHI mitigation in the development of future urban structures should aim at minimizing the enveloping surface of urban structures. The resulting reduction in the release of stored heat during night-time is expected to have a positive impact on energy consumption and health (*173*).

Furthermore, we demonstrated that costs of UHI are closely related to regional temperature variations, which can shift financial and environmental costs from positive to negative, and vice versa. By quantifying environmental impact that UHI-imposed temperature changes have on energy consumptions in residential buildings, we are in a unique position to help cities and states tackle climate change with executable and concrete measures. Projection of financial benefits and carbon emission reductions appeal not only to legislators and policy makers, but also to voters and private investors who recognize the value in sustainable design. When linked with urban population changes this analysis can be applied to prioritizing energy policies and regulations for UHI controls. Current cities where UHI has negative effects should seek to utilize sustainability retrofitting strategies (*79*) such as green and cool roofs, or reflective pavements, while future cities should focus their efforts on minimizing the envelope structure of buildings and considering non-

regular layouts for streets. On the other hand, cities that seek to maximize benefits of UHI through lowered heating energy demand should concentrate on forming high density building clusters arranged on a regular grid (*57*). As a result, controlling UHI becomes a method for partially managing space heating and cooling energy consumption and a tool for helping cities, states and countries achieve their greenhouse gas emissions reduction goals. States of Florida and Texas are currently the most negatively influenced by UHI states in the US and in consideration of their future population growth, they should be prioritized for any future environmental building energy regulations and UHI mitigation strategies. They should also consider adopting street layouts and sky view factors that minimize UHI in their future urban expansion. We are confident that the negative impacts of UHI from the residential sector outlined in this study, will translate directly in the form of intensified energy bills among the commercial sector, which contributes to about 10% of the US total energy consumption (*51*). However, before making any policy recommendations for states with high ratio of $HDD{:}CDD$, where for the residential sector UHI has positive effects on energy costs and CO_2 emissions, we strongly recommend investigating impacts of UHI on the commercial sector, which has much higher cooling costs relative to heating expenditure when compared to residential buildings. Above all, urban planners and legislators should not neglect common UHI mitigation techniques simply because UHI significantly lowers the energy bill. UHI mitigation techniques that increase green space in cities have the potential to reduce the severity of summer heatwaves (*174*), as well as improve comfort, health and safety of local communities (*175*), which are benefits that extend far beyond the monetary energy savings. Therefore, we believe that UHI mitigation techniques should always be incorporated into planning methods for optimizing UHI in cities.

6.3. Improving Building Design Codes

To reinvigorate design codes and better predict hazard damage, we identified that city texture, specifically unique local geometric layouts affect the flow and thus pressure acting on buildings captured in the form of drag coefficients. This urban resilience model created using computational fluid dynamics models of different city textures with common geometrical layouts as well as idealistic regular and staggered grids of different densities shows that on average current building design codes, which assume $C_d \leq 2$, capture less than 50% expected maximal damage, which may

partially explain why we buildings during hurricanes of categories 3 or 4, experience damage expected to be seen during hurricane of category 5. Verified using CFD experiments and tested for the case study of damage in Mexico Beach, FL in 2018 for Hurricane Michael, city texture approach is able to predict damage with over 67% accuracy with just a single easy to obtain—using online maps, here exemplified for OpenStreetMap—input of building footprints, which are analyzed to derive two, critical for C_d, local parameters: 1) commonly used in wind flow studies frontal density λ_f and 2) a number of local neighboring buildings C_n. Furthermore, we find that crystal-like cites have higher susceptibility to hurricane damage showing higher proportion of buildings with upper range values of drag coefficients. Using this approach, stakeholders not only can readily identify entire cities' textures and their vulnerability to hurricane damage, but also (and more importantly) can identify buildings with the highest risk of damage. This will ease the process of targeted retrofitting thereby enabling more resilient developments and urban planning to reduce the risk of hurricane damage and mitigate the kinds of extreme damage experienced by communities like Mexico Beach, FL. This comes in time for the uncertain future of changing climate and the intensified extreme weather conditions, especially in regions likes Texas or Florida, places that are expected to have tens of thousands of residential buildings build in the next decade to accommodate some of the highest population growths in the US [Fig.4-12].

6.4. Future Work

The city texture drag coefficient model relies on two main assumptions: 1) buildings have the same heights and 2) there are no object between buildings. The model also ignores any changes in elevation, by assuming a flat landscape. In real-life these assumptions are not always true and therefore should be tested under hurricane conditions using CFD simulations, to improve its accuracy. Moreover, incorporating information about building materials is going to be critical in predicting accurately damage during the storm as collapsing buildings are going to change the local city texture. Ultimately, with an enhanced approach of this kind, with current availability of GIS and wind speed data from climatic models, we could create accurate hurricane risk maps for any city or building in the world. In addition, to understand the influence of order of buildings, we suggest conducting a large sample, controlled study, which accounts for various distributions of local order parameters, while keeping average density and building sizes fixed. In addition, we

suggest that exploring a multi-size particle $g(r)$ could offer valuable insights on cities with a high variability in building size and possibly lead to better prediction in UHI and drag coefficient modeling.

Beyond the scope of hurricane damage and Urban Heat Islands, we believe that utilizing city texture approach for quantifying the intrinsic complexity of building networks have the potential to be applied to study amenities, transportation, as well as other urban functions to create new urban models that focus on all aspects of a livable and vibrant smart city of the future.

7. References

1. G. Holland, C. L. Bruyère, Recent intense hurricane response to global climate change. *Clim. Dyn.* **42**, 617–627 (2014).

2. P. Peduzzi, B. Chatenoux, H. Dao, A. D. Bono, C. Herold, J. Kossin, F. Mouton, O. Nordbeck, Global trends in tropical cyclone risk. *Nat. Clim. Change*. **2**, 289–294 (2012).

3. K. T. Bhatia, G. A. Vecchi, T. R. Knutson, H. Murakami, J. Kossin, K. W. Dixon, C. E. Whitlock, Recent increases in tropical cyclone intensification rates. *Nat. Commun.* **10**, 1–9 (2019).

4. T. W. Smith, J. Kim, J. Son, Public Attitudes toward Climate Change and Other Environmental Issues across Countries. *Int. J. Sociol.* **47**, 62–80 (2017).

5. H. Graham, S. de Bell, N. Hanley, S. Jarvis, P. C. L. White, Willingness to pay for policies to reduce future deaths from climate change: evidence from a British survey. *Public Health*. **174**, 110–117 (2019).

6. L. Everuss, M. Carvalho, J. L. Casanova, D. Chaffee, C. Lever-Tracy, Assessing the public willingness to contribute income to mitigate the effects of climate change: A comparison of Adelaide and Lisbon. *J. Sociol.* **53**, 334–350 (2017).

7. E. Marris, Why young climate activists have captured the world's attention. *Nature*. **573**, 471–472 (2019).

8. Q. Schiermeier, K. Atkinson, E. R. Mega, T. V. Padma, E. Stoye, J. Tollefson, A. Witze, Scientists worldwide join strikes for climate change. *Nature*. **573**, 472–473 (2019).

9. M. Lockwood, Solar change and climate: an update in the light of the current exceptional solar minimum. *Proc. R. Soc. Math. Phys. Eng. Sci.* **466**, 303–329 (2010).

10. J. L. Lean, Cycles and trends in solar irradiance and climate. *WIREs Clim. Change*. **1**, 111–122 (2010).

11. K. Emanuel, Assessing the present and future probability of Hurricane Harvey's rainfall. *Proc. Natl. Acad. Sci.* **114**, 12681–12684 (2017).

12. K. J. E. Walsh, J. L. McBride, P. J. Klotzbach, S. Balachandran, S. J. Camargo, G. Holland, T. R. Knutson, J. P. Kossin, T. Lee, A. Sobel, M. Sugi, Tropical cyclones and climate change. *WIREs Clim. Change*. **7**, 65–89 (2016).

13. D. Keellings, J. J. H. Ayala, Extreme Rainfall Associated With Hurricane Maria Over Puerto Rico and Its Connections to Climate Variability and Change. *Geophys. Res. Lett.* **46**, 2964–2973 (2019).

14. J. Jouzel, V. Masson-Delmotte, O. Cattani, G. Dreyfus, S. Falourd, G. Hoffmann, B. Minster, J. Nouet, J. M. Barnola, J. Chappellaz, H. Fischer, J. C. Gallet, S. Johnsen, M. Leuenberger, L. Loulergue, D. Luethi, H. Oerter, F. Parrenin, G. Raisbeck, D. Raynaud, A. Schilt, J. Schwander, E. Selmo, R. Souchez, R. Spahni, B. Stauffer, J. P. Steffensen, B. Stenni, T. F. Stocker, J. L. Tison, M. Werner, E. W. Wolff, Orbital and Millennial Antarctic Climate Variability over the Past 800,000 Years. *Science*. **317**, 793–796 (2007).

15. Core Writing Team, R. K. Pachauri, L. A. Meyer, IPCC, 2014: Climate Change 2014: Synthesis Report. Contribution of Working Groups I, II and III to the Fifth Assessment Report of the Intergovernmental Panel on Climate Change (2014).

16. T. Dinan, Projected Increases in Hurricane Damage in the United States: The Role of Climate Change and Coastal Development. *Ecol. Econ.* **138**, 186–198 (2017).

17. K. Bhatia, G. Vecchi, H. Murakami, S. Underwood, J. Kossin, Projected Response of Tropical Cyclone Intensity and Intensification in a Global Climate Model. *J. Clim.* **31**, 8281–8303 (2018).

18. G. C. Hegerl, S. Brönnimann, T. Cowan, A. R. Friedman, E. Hawkins, C. Iles, W. Müller, A. Schurer, S. Undorf, Causes of climate change over the historical record. *Environ. Res. Lett.* **14**, 123006 (2019).

19. B. T. Anderson, J. R. Knight, M. A. Ringer, J.-H. Yoon, A. Cherchi, Testing for the Possible Influence of Unknown Climate Forcings upon Global Temperature Increases from 1950 to 2000. *J. Clim.* **25**, 7163–7172 (2012).

20. S. C. Sekhar, Thermal comfort in air-conditioned buildings in hot and humid climates – why are we not getting it right? *Indoor Air*. **26**, 138–152 (2016).

21. Z. R. Stahlschmidt, D. F. DeNardo, J. N. Holland, B. P. Kotler, M. Kruse-Peeples, Tolerance mechanisms in North American deserts: Biological and societal approaches to climate change. *J. Arid Environ.* **75**, 681–687 (2011).

22. J. P. Gibert, M.-C. Chelini, M. F. Rosenthal, J. P. DeLong, Crossing regimes of temperature dependence in animal movement. *Glob. Change Biol.* **22**, 1722–1736 (2016).

23. P. J. Thomas, A. K. Labrosse, A. C. Pomeroy, K. A. Otter, Effects of weather on avian migration at proposed ridgeline wind energy sites. *J. Wildl. Manag.* **75**, 805–815 (2011).

24. M. Abecassis, I. Senina, P. Lehodey, P. Gaspar, D. Parker, G. Balazs, J. Polovina, A Model of Loggerhead Sea Turtle (Caretta caretta) Habitat and Movement in the Oceanic North Pacific. *PLOS ONE.* **8**, e73274 (2013).

25. R. A. Kerr, Melting Glaciers, Not Just Ice Sheets, Stoking Sea-Level Rise. *Science.* **340**, 798–798 (2013).

26. P. D. Noerdlinger, K. R. Brower, The melting of floating ice raises the ocean level. *Geophys. J. Int.* **170**, 145–150 (2007).

27. J. T. Overpeck, B. L. Otto-Bliesner, G. H. Miller, D. R. Muhs, R. B. Alley, J. T. Kiehl, Paleoclimatic Evidence for Future Ice-Sheet Instability and Rapid Sea-Level Rise. *Science.* **311**, 1747–1750 (2006).

28. R. B. Alley, P. U. Clark, P. Huybrechts, I. Joughin, Ice-Sheet and Sea-Level Changes. *Science.* **310**, 456–460 (2005).

29. Rhein, M., S.R. Rintoul, S. Aoki, E. Campos, D. Chambers, R.A. Feely, S. Gulev, G.C. Johnson, S.A. Josey, A. Kostianoy, C. Mauritzen, D. Roemmich, L.D. Talley and F. Wang, "2013: Observations: Ocean. In: Climate Change 2013: The Physical Science Basis. Contribution of Working Group I to the Fifth Assessment Report of the Intergovernmental Panel on Climate Change [Stocker, T.F., D. Qin, G.-K. Plattner, M. Tignor, S.K. Allen, J. Boschung, A. Nauels, Y. Xia, V. Bex and P.M. Midgley (eds.)]. Cambridge University Press, Cambridge, United Kingdom and New York, NY, USA."

30. E. W. LEULIETTE, J. K. WILLIS, Balancing the Sea Level Budget. *Oceanography.* **24**, 122–129 (2011).

31. M. J. Widlansky, A. Timmermann, W. Cai, Future extreme sea level seesaws in the tropical Pacific. *Sci. Adv.* **1**, e1500560 (2015).

32. J. Obeysekera, J. Park, Scenario-Based Projection of Extreme Sea Levels. *J. Coast. Res.*, 1–7 (2012).

33. T. Wahl, Sea-level rise and storm surges, relationship status: complicated! *Environ. Res. Lett.* **12**, 111001 (2017).

34. G. J. van Oldenborgh, K. van der Wiel, A. Sebastian, R. Singh, J. Arrighi, F. Otto, K. Haustein, S. Li, G. Vecchi, H. Cullen, Attribution of extreme rainfall from Hurricane Harvey, August 2017. *Environ. Res. Lett.* **12**, 124009 (2017).

35. A. K. Mishra, V. P. Singh, Drought modeling – A review. *J. Hydrol.* **403**, 157–175 (2011).

36. H. Ramsay, The Global Climatology of Tropical Cyclones. *Oxf. Res. Encycl. Nat. Hazard Sci.* (2017), doi:10.1093/acrefore/9780199389407.013.79.

37. M. D. Risser, M. F. Wehner, *Geophys. Res. Lett.*, in press, doi:10.1002/2017GL075888.

38. P. Nejat, F. Jomehzadeh, M. M. Taheri, M. Gohari, M. Z. Abd. Majid, A global review of energy consumption, CO 2 emissions and policy in the residential sector (with an overview of the top ten CO 2 emitting countries). *Renew. Sustain. Energy Rev.* **43**, 843–862 (2015).

39. D. Lüthi, M. L. Floch, B. Bereiter, T. Blunier, J.-M. Barnola, U. Siegenthaler, D. Raynaud, J. Jouzel, H. Fischer, K. Kawamura, T. F. Stocker, High-resolution carbon dioxide concentration record 650,000–800,000 years before present. *Nature*. **453**, 379–382 (2008).

40. NOAA, Hurricane Costs, (available at https://coast.noaa.gov/states/fast-facts/hurricane-costs.html).

41. E. A. Parson, D. W. Keith, Fossil Fuels Without CO2 Emissions. *Science*. **282**, 1053–1054 (1998).

42. M. Höök, X. Tang, Depletion of fossil fuels and anthropogenic climate change—A review. *Energy Policy*. **52**, 797–809 (2013).

43. G. Martin, E. Saikawa, Effectiveness of state climate and energy policies in reducing power-sector CO2 emissions. *Nat. Clim. Change*. **7**, 912–919 (2017).

44. P.-P. Pichler, T. Zwickel, A. Chavez, T. Kretschmer, J. Seddon, H. Weisz, Reducing Urban Greenhouse Gas Footprints. *Sci. Rep.* **7**, 14659 (2017).

45. O. Edenhofer, R. Pichs-Madruga, Y. Sokona, J. C. Minx, E. Farahani, S. Kadner, K. Seyboth, A. Adler, I. Baum, S. Brunner, P. Eickemeier, B. Kriemann, J. Savolainen, S.

Schlömer, C. von Stechow, T. Zwickel, "Climate Change 2014: Mitigation of Climate Change" (2014).

46. B. G. Rabe, *Statehouse and Greenhouse: The Emerging Politics of American Climate Change Policy* (Brookings Institution Press, Washington, D.C, 2004).

47. K. Hubacek, G. Baiocchi, K. Feng, R. Muñoz Castillo, L. Sun, J. Xue, Global carbon inequality. *Energy Ecol. Environ.* **2**, 361–369 (2017).

48. M. B. Ali, R. Saidur, M. S. Hossain, A review on emission analysis in cement industries. *Renew. Sustain. Energy Rev.* **15**, 2252–2261 (2011).

49. G. Peters, J. Minx, C. Weber, O. Edenhofer, Growth in emission transfers via international trade from 1990 to 2008. *Proc. Natl. Acad. Sci. U. S. A.* **108**, 8903–8 (2011).

50. L. Pérez-Lombard, J. Ortiz, C. Pout, A review on buildings energy consumption information. *Energy Build.* **40**, 394–398 (2008).

51. D. Ürge-Vorsatz, L. F. Cabeza, S. Serrano, C. Barreneche, K. Petrichenko, Heating and cooling energy trends and drivers in buildings. *Renew. Sustain. Energy Rev.* **41**, 85–98 (2015).

52. M. J. Abdolhosseini Qomi, A. Noshadravan, J. M. Sobstyl, J. Toole, J. Ferreira, R. J.-M. Pellenq, F.-J. Ulm, M. C. Gonzalez, Data analytics for simplifying thermal efficiency planning in cities. *J. R. Soc. Interface.* **13** (2016), doi:10.1098/rsif.2015.0971.

53. A. M. Rizwan, L. Y. C. Dennis, C. Liu, A review on the generation, determination and mitigation of Urban Heat Island. *J. Environ. Sci.* **20**, 120–128 (2008).

54. X. Li, Y. Zhou, G. R. Asrar, M. Imhoff, X. Li, The surface urban heat island response to urban expansion: A panel analysis for the conterminous United States. *Sci. Total Environ.* **605–606**, 426–435 (2017).

55. T. R. Oke, City size and the urban heat island. *Atmospheric Environ. 1967.* **7**, 769–779 (1973).

56. P. Ramamurthy, E. Bou-Zeid, Heatwaves and urban heat islands: A comparative analysis of multiple cities. *J. Geophys. Res. Atmospheres.* **122**, 2016JD025357 (2017).

57. J. Sobstyl, T. Emig, M. J. Abdolhosseini Qomi, F.-J. Ulm, R. J.-M. Pellenq, Role of City Texture in Urban Heat Islands at Night Time. *Phys. Rev. Lett.* **120**, 108701 (2018).

58. B. A. Norton, A. M. Coutts, S. J. Livesley, R. J. Harris, A. M. Hunter, N. S. G. Williams, Planning for cooler cities: A framework to prioritise green infrastructure to mitigate high temperatures in urban landscapes. *Landsc. Urban Plan.* **134**, 127–138 (2015).

59. P. A. Mirzaei, Recent challenges in modeling of urban heat island. *Sustain. Cities Soc.* **19**, 200–206 (2015).

60. P. A. Mirzaei, D. Olsthoorn, M. Torjan, F. Haghighat, Urban neighborhood characteristics influence on a building indoor environment. *Sustain. Cities Soc.* **19**, 403–413 (2015).

61. M. G. Flanner, Integrating anthropogenic heat flux with global climate models. *Geophys. Res. Lett.* **36**, L02801 (2009).

62. M. Santamouris, *Energy and Climate in the Urban Built Environment* (2001; https://www.amazon.com/Energy-Climate-Environment-Buildings-Technology/dp/1873936907), *Buildings Energy and Solar Technology.*

63. L. Zhao, X. Lee, R. B. Smith, K. Oleson, Strong contributions of local background climate to urban heat islands. *Nature.* **511**, 216–219 (2014).

64. M. Santamouris, C. Cartalis, A. Synnefa, D. Kolokotsa, On the impact of urban heat island and global warming on the power demand and electricity consumption of buildings—A review. *Energy Build.* **98**, 119–124 (2015).

65. U.S. Environmental Protection Agency, "Reducing urban heat islands: Compendium of strategies" (2008), (available at https://www.epa.gov/heat-islands/heat-island-compendium).

66. F. Estrada, W. J. W. Botzen, R. S. J. Tol, A global economic assessment of city policies to reduce climate change impacts. *Nat. Clim. Change.* **7**, 403–406 (2017).

67. B. Stone, J. J. Hess, H. Frumkin, Urban Form and Extreme Heat Events: Are Sprawling Cities More Vulnerable to Climate Change Than Compact Cities? *Environ. Health Perspect.* **118**, 1425–1428 (2010).

68. J. A. Voogt, T. R. Oke, Thermal remote sensing of urban climates. *Remote Sens. Environ.* **86**, 370–384 (2003).

69. L. Doulos, M. Santamouris, I. Livada, Passive cooling of outdoor urban spaces. The role of materials. *Sol. Energy.* **77**, 231–249 (2004).

70. J. Unger, Intra-urban relationship between surface geometry and urban heat island: Review and new approach. *Clim. Res.* **27**, 253–264 (2004).

71. T. Oke, The energetic basis of urban heat island. *Q. J. R. Meteorol. Soc.* **108**, 1–24 (1982).

72. W. Zhou, G. Huang, M. L. Cadenasso, Does spatial configuration matter? Understanding the effects of land cover pattern on land surface temperature in urban landscapes. *Landsc. Urban Plan.* **102**, 54–63 (2011).

73. A. Mohajerani, J. Bakaric, T. Jeffrey-Bailey, The urban heat island effect, its causes, and mitigation, with reference to the thermal properties of asphalt concrete. *J. Environ. Manage.* **197**, 522–538 (2017).

74. F. Rosso, I. Golasi, V. L. Castaldo, C. Piselli, A. L. Pisello, F. Salata, M. Ferrero, F. Cotana, A. de Lieto Vollaro, On the impact of innovative materials on outdoor thermal comfort of pedestrians in historical urban canyons. *Renew. Energy.* **118**, 825–839 (2018).

75. M. Medina-Ramón, J. Schwartz, Temperature, temperature extremes, and mortality: a study of acclimatisation and effect modification in 50 US cities. *Occup. Environ. Med.* **64**, 827–833 (2007).

76. M. Meinshausen, N. Meinshausen, W. Hare, S. C. B. Raper, K. Frieler, R. Knutti, D. J. Frame, M. R. Allen, Greenhouse-gas emission targets for limiting global warming to 2 °C. *Nature*. **458**, 1158–1162 (2009).

77. N. B. Grimm, S. H. Faeth, N. E. Golubiewski, C. L. Redman, J. Wu, X. Bai, J. M. Briggs, Global Change and the Ecology of Cities. *Science*. **319**, 756–760 (2008).

78. Q. Huang, Y. Lu, Urban heat island research from 1991 to 2015: a bibliometric analysis. *Theor. Appl. Climatol.* (2017), doi:10.1007/s00704-016-2025-1.

79. H. Akbari, C. Cartalis, D. Kolokotsa, A. Muscio, A. L. Pisello, F. Rossi, M. Santamouris, A. Synnefa, N. H. Wong, M. Zinzi, Local climate change and urban heat island mitigation techniques – the state of the art. *J. Civ. Eng. Manag.* **22**, 1–16 (2016).

80. Y. Kikegawa, Y. Genchi, H. Yoshikado, H. Kondo, Development of a numerical simulation system toward comprehensive assessments of urban warming countermeasures including their impacts upon the urban buildings' energy-demands. *Appl. Energy*. **76**, 449–466 (2003).

81. M. Santamouris, N. Papanikolaou, I. Livada, I. Koronakis, C. Georgakis, A. Argiriou, D. N. Assimakopoulos, On the impact of urban climate on the energy consumption of buildings. *Sol. Energy.* **70**, 201–216 (2001).

82. S. Magli, C. Lodi, L. Lombroso, A. Muscio, S. Teggi, Analysis of the urban heat island effects on building energy consumption. *Int. J. Energy Environ. Eng.* **6**, 91–99 (2015).

83. D. R. Easterling, G. A. Meehl, C. Parmesan, S. A. Changnon, T. R. Karl, L. O. Mearns, Climate Extremes: Observations, Modeling, and Impacts. *Science.* **289**, 2068–2074 (2000).

84. N. A. Rayner, D. E. Parker, E. B. Horton, C. K. Folland, L. V. Alexander, D. P. Rowell, E. C. Kent, A. Kaplan, Global analyses of sea surface temperature, sea ice, and night marine air temperature since the late nineteenth century. *J. Geophys. Res. Atmospheres.* **108** (2003), doi:10.1029/2002JD002670.

85. K. E. Taylor, R. J. Stouffer, G. A. Meehl, An Overview of CMIP5 and the Experiment Design. *Bull. Am. Meteorol. Soc.* **93**, 485–498 (2011).

86. L. G. Swan, V. I. Ugursal, Modeling of end-use energy consumption in the residential sector: A review of modeling techniques. *Renew. Sustain. Energy Rev.* **13**, 1819–1835 (2009).

87. R. L. Wilby, R. Keenan, Adapting to flood risk under climate change. *Prog. Phys. Geogr. Earth Environ.* **36**, 348–378 (2012).

88. W. G. Peacock, S. D. Brody, W. Highfield, Hurricane risk perceptions among Florida's single family homeowners. *Landsc. Urban Plan.* **73**, 120–135 (2005).

89. Li Yue, Ahuja Aakash, Padgett Jamie E., Review of Methods to Assess, Design for, and Mitigate Multiple Hazards. *J. Perform. Constr. Facil.* **26**, 104–117 (2012).

90. Zahmatkesh Zahra, Burian Steven J., Karamouz Mohammad, Tavakol-Davani Hassan, Goharian Erfan, Low-Impact Development Practices to Mitigate Climate Change Effects on Urban Stormwater Runoff: Case Study of New York City. *J. Irrig. Drain. Eng.* **141**, 04014043 (2015).

91. P. J. Vickery, F. J. Masters, M. D. Powell, D. Wadhera, Hurricane hazard modeling: The past, present, and future. *J. Wind Eng. Ind. Aerodyn.* **97**, 392–405 (2009).

92. New York Times, Among the Ruins of Mexico Beach Stands One House, Built 'for the Big One' (2018), (available at https://www.nytimes.com/2018/10/14/us/hurricane-michael-florida-mexico-beach-house.html).

93. American Society of Civil Engineers (ASCE), Minimum design loads for buildings and other structures (2010).

94. P. Krishna, Wind loads on low rise buildings — A review. *J. Wind Eng. Ind. Aerodyn.* **54–55**, 383–396 (1995).

95. D. K. Kwon, A. Kareem, Comparative study of major international wind codes and standards for wind effects on tall buildings. *Eng. Struct.* **51**, 23–35 (2013).

96. E. Aktas, F. Moses, M. Ghosn, Cost and safety optimization of structural design specifications. *Reliab. Eng. Syst. Saf.* **73**, 205–212 (2001).

97. M. M. Szerszen, A. S. Nowak, Calibration of Design Code for Buildings (ACI 318): Part 2—Reliability Analysis and Resistance Factors. *Struct. J.* **100**, 383–391 (2003).

98. X. Chen, N. Zhou, Equivalent static wind loads on low-rise buildings based on full-scale pressure measurements. *Eng. Struct.* **29**, 2563–2575 (2007).

99. H. Tanaka, Y. Tamura, K. Ohtake, M. Nakai, Y. Chul Kim, Experimental investigation of aerodynamic forces and wind pressures acting on tall buildings with various unconventional configurations. *J. Wind Eng. Ind. Aerodyn.* **107–108**, 179–191 (2012).

100. B. Xu, N. Huang, W. He, Y. Chen, Investigation on terminal velocity and drag coefficient of particles with different shapes. *J. Phys. Conf. Ser.* **822**, 012047 (2017).

101. W. F. Dabberdt, F. L. Ludwig, W. B. Johnson, Validation and applications of an urban diffusion model for vehicular pollutants. *Atmospheric Environ. 1967.* **7**, 603–618 (1973).

102. T. R. Oke, Street design and urban canopy layer climate. *Energy Build.* **11**, 103–113 (1988).

103. L. Chen, J. Hang, M. Sandberg, L. Claesson, S. Di Sabatino, H. Wigo, The impacts of building height variations and building packing densities on flow adjustment and city breathability in idealized urban models. *Build. Environ.* **118**, 344–361 (2017).

104. J. L. Santiago, A. Martilli, F. Martín, CFD simulation of airflow over a regular array of cubes. Part I: Three-dimensional simulation of the flow and validation with wind-tunnel measurements. *Bound.-Layer Meteorol.* **122**, 609–634 (2007).

105. A. Martilli, J. L. Santiago, CFD simulation of airflow over a regular array of cubes. Part II: analysis of spatial average properties. *Bound.-Layer Meteorol.* **122**, 635–654 (2007).

106. C. S. B. Grimmond, T. R. Oke, Aerodynamic Properties of Urban Areas Derived from Analysis of Surface Form. *J. Appl. Meteorol.* **38**, 1262–1292 (1999).

107. E. Gutiérrez, A. Martilli, J. L. Santiago, J. E. E. González, A Mechanical Drag Coefficient Formulation and Urban Canopy Parameter Assimilation Technique for Complex Urban Environments. *Bound.-Layer Meteorol.* **157**, 333–341 (2015).

108. Steady-flow experiments in urban areas and anisotropic porosity model: Journal of Hydraulic Research: Vol 55, No 1, (available at https://www.tandfonline.com/doi/abs/10.1080/00221686.2016.1238013).

109. R. Ramponi, B. Blocken, L. B. de Coo, W. D. Janssen, CFD simulation of outdoor ventilation of generic urban configurations with different urban densities and equal and unequal street widths. *Build. Environ.* **92**, 152–166 (2015).

110. W.-C. Cheng, F. Porté-Agel, Adjustment of Turbulent Boundary-Layer Flow to Idealized Urban Surfaces: A Large-Eddy Simulation Study. *Bound.-Layer Meteorol.* **155**, 249–270 (2015).

111. A. F. Mohammad, S. A. Zaki, M. S. M. Ali, H. Aya, A. A. Razak, M. Shirakashi, N. Arai, Large Eddy Simulation of Wind Pressure Distribution on Heterogeneous Buildings in Idealised Urban Models. *Energy Procedia.* **78**, 3055–3060 (2015).

112. J. Allegrini, V. Dorer, J. Carmeliet, Influence of morphologies on the microclimate in urban neighbourhoods. *J. Wind Eng. Ind. Aerodyn.* **144**, 108–117 (2015).

113. M. J. Brown, R. E. Lawson, "COMPARISON OF CENTERLINE VELOCITY MEASUREMENTS OBTAINED AROUND 2D AND 3D BUILDING ARRAYS IN A WIND TUNNEL" (LA-UR-01-4131, Los Alamos National Lab., NM (US), 2001), (available at https://www.osti.gov/biblio/783425-comparison-centerline-velocity-measurements-obtained-around-building-arrays-wind-tunnel).

114. E. Bernardini, S. M. J. Spence, D. Wei, A. Kareem, Aerodynamic shape optimization of civil structures: A CFD-enabled Kriging-based approach. *J. Wind Eng. Ind. Aerodyn.* **144**, 154–164 (2015).

115. M. Barthelemy, P. Bordin, H. Berestycki, M. Gribaudi, Self-organization versus top-down planning in the evolution of a city (2013).

116. P. Bogucki, *Origin of Human Society* (John Wiley & Sons, 1 edition., 1999).

117. E. Glaeser, *Triumph of the City: How Our Greatest Invention Makes Us Richer, Smarter, Greener, Healthier, and Happier* (Penguin Books, Reprint edition., 2012).

118. J. Jacobs, *The Death and Life of Great American Cities* (Vintage, Reissue edition., 1992).

119. P. L. Knox, L. M. McCarthy, *Urbanization: An Introduction to Urban Geography* (Pearson, 3 edition., 2011).

120. F. Lederbogen, P. Kirsch, L. Haddad, F. Streit, H. Tost, P. Schuch, S. Wüst, J. C. Pruessner, M. Rietschel, M. Deuschle, A. Meyer-Lindenberg, City living and urban upbringing affect neural social stress processing in humans. *Nature*. **474**, 498–501 (2011).

121. P. M. Pardalos, S. Th. Rassia, *Cities for Smart Environmental and Energy Futures: Impacts on Architecture and Technology (Energy Systems)* (Springer, 2013; https://www.abebooks.com/9783642376603/Cities-Smart-Environmental-Energy-Futures-3642376606/plp).

122. Aristotle, *Complete Works of Aristotle, Vol. 1* (Princeton University Press, Bollingen Series edition., 1984).

123. H. A. Makse, S. Havlin, H. E. Stanley, Modelling urban growth patterns. *Nature*. **377**, 608–612 (1995).

124. M. Batty, The Size, Scale, and Shape of Cities. *Science*. **319**, 769–771 (2008).

125. L. Bettencourt, G. West, A unified theory of urban living. *Nature*. **467**, 912–913 (2010).

126. D. Black, V. Henderson, A Theory of Urban Growth. *J. Polit. Econ.* **107**, 252–284 (1999).

127. L. M. A. Bettencourt, J. Lobo, D. Helbing, C. Kühnert, G. B. West, Growth, innovation, scaling, and the pace of life in cities. *Proc. Natl. Acad. Sci.* **104**, 7301–7306 (2007).

128. K. Lynch, *Good City Form* (The MIT Press, Reprint edition., 1984).

129. M. C. Boyer, *Dreaming the rational city: The myth of American city planning* (MIT Press, First Edition edition., 1983).

130. A. J. Arnfield, Two decades of urban climate research: a review of turbulence, exchanges of energy and water, and the urban heat island. *Int. J. Climatol.* **23**, 1–26 (2003).

131. (EIA) U.S. Energy Information Administration, Residential Energy Consumption Survey (RECS) - Data. U.S. Energy Information Administration (EIA) (2009), (available at https://www.eia.gov/consumption/residential/data/2009/).

132. N. National Centers for Environmental Information, Climate at a Glance: Time Series (2009), (available at https://www.ncdc.noaa.gov/cag/time-series/us/).

133. *microsoft/USBuildingFootprints* (Microsoft, 2020; https://github.com/microsoft/USBuildingFootprints).

134. U.S. Census Bureau, "State Interim Population Projections by Age and Sex: 2004 - 2030" (2005).

135. U. C. B. US Census Bureau, 2010 Census Urban and Rural Classification and Urban Area Criteria (2010), (available at https://www.census.gov/geo/reference/ua/urban-rural-2010.html).

136. K. Lynch, The Form of Cities. *Sci. Am.* **190**, 54–63 (1954).

137. A. G. Wilson, Modelling and Systems Analysis in Urban Planning. *Nature*. **220**, 963–966 (1968).

138. M. Batty, *Cities and Complexity: Understanding Cities with Cellular Automata, Agent-Based Models, and Fractals* (MIT Press, 2007).

139. R. Louf, M. Barthelemy, Modeling the polycentric transition of cities. *Phys. Rev. Lett.* **111**, 198702 (2013).

140. N. D. Mermin, Crystalline Order in Two Dimensions. *Phys. Rev.* **176**, 250–254 (1968).

141. J. P. Sethna, *Statistical Mechanics: Entropy, Order Parameters and Complexity* (Oxford University Press, 2006).

142. H. Kusaka, F. Kimura, Thermal Effects of Urban Canyon Structure on the Nocturnal Heat Island: Numerical Experiment Using a Mesoscale Model Coupled with an Urban Canopy Model. *J. Appl. Meteorol.* **43**, 1899–1910 (2004).

143. I. Eliasson, Urban nocturnal temperatures, street geometry and land use. *Atmos. Environ.* **30**, 379–392 (1996).

144. J. Fröhlich, D. von Terzi, Hybrid LES/RANS methods for the simulation of turbulent flows. *Prog. Aerosp. Sci.* **44**, 349–377 (2008).

145. C.-H. Wu, G. A. Kopp, Estimation of Wind-Induced Pressures on a Low-Rise Building Using Quasi-Steady Theory. *Front. Built Environ.* **2** (2016), doi:10.3389/fbuil.2016.00005.

146. W. Rodi, Comparison of LES and RANS calculations of the flow around bluff bodies. *J. Wind Eng. Ind. Aerodyn.* **69–71**, 55–75 (1997).

147. B. Li, J. Liu, J. Gao, Surface wind pressure tests on buildings with various non-uniformity morphological parameters. *J. Wind Eng. Ind. Aerodyn.* **137**, 14–24 (2015).

148. R. L. McGreevy, M. A. Howe, RMC: Modeling Disordered Structures. *Annu. Rev. Mater. Sci.* **22**, 217–242 (1992).

149. C. Bousige, A. Boţan, F.-J. Ulm, R. J.-M. Pellenq, B. Coasne, Optimized molecular reconstruction procedure combining hybrid reverse Monte Carlo and molecular dynamics. *J. Chem. Phys.* **142**, 114112 (2015).

150. G. Tóth, A. Baranyai, Conceptual and technical improvement of the reverse Monte Carlo algorithm. *J. Chem. Phys.* **107**, 7402–7408 (1997).

151. J. Naudts, Solving inverse problems by combination of maximum entropy and montecarlo simulation (2000).

152. T. Broderick, M. Dudik, G. Tkacik, R. E. Schapire, W. Bialek, Faster solutions of the inverse pairwise Ising problem. *ArXiv07122437 Cond-Mat Q-Bio* (2007) (available at http://arxiv.org/abs/0712.2437).

153. K. Weise, M. Matzke, A priori distributions from the principle of maximum entropy for the Monte Carlo unfolding of particle energy spectra. *Nucl. Instrum. Methods Phys. Res. Sect. Accel. Spectrometers Detect. Assoc. Equip.* **280**, 103–112 (1989).

154. A. E. Roy, *Astronomy, principles and practice* (Hilger, 1977).

155. P. J. C. Schrijvers, H. J. J. Jonker, S. Kenjereš, S. R. de Roode, Breakdown of the night time urban heat island energy budget. *Build. Environ.* **83**, 50–64 (2015).

156. H. Taha, Urban climates and heat islands: albedo, evapotranspiration, and anthropogenic heat. *Energy Build.* **25**, 99–103 (1997).

157. T. R. Oke, Canyon geometry and the nocturnal urban heat island: Comparison of scale model and field observations. *J. Climatol.* (1981), doi:10.1002/joc.3370010304.

158. Source Energy. Energy Star Portfolio Manager Technical Reference (2013).

159. N. S. Fouad, G. H. Mahmoud, N. E. Nasr, Comparative study of international codes wind loads and CFD results for low rise buildings. *Alex. Eng. J.* **57**, 3623–3639 (2018).

160. P. A. Irwin, Wind engineering challenges of the new generation of super-tall buildings. *J. Wind Eng. Ind. Aerodyn.* **97**, 328–334 (2009).

161. T. Nozu, T. Tamura, K. Takeshi, K. Akira, Mesh-adaptive LES for wind load estimation of a high-rise building in a city. *J. Wind Eng. Ind. Aerodyn.* **144**, 62–69 (2015).

162. S. T. Laboy-Rodríguez, K. R. Gurley, F. J. Masters, Revisiting the directionality factor in ASCE 7. *J. Wind Eng. Ind. Aerodyn.* **133**, 225–233 (2014).

163. J. C. Senkbeil, S. C. Sheridan, A Postlandfall Hurricane Classification System for the United States. *J. Coast. Res.* **2006**, 1025–1034 (2006).

164. M. Velickovic, Y. Zech, S. Soares-Frazão, Steady-flow experiments in urban areas and anisotropic porosity model. *J. Hydraul. Res.* **55**, 85–100 (2017).

165. Zhou Yin, Kareem Ahsan, Gu Ming, Mode Shape Corrections for Wind Load Effects. *J. Eng. Mech.* **128**, 15–23 (2002).

166. J. L. Santiago, O. Coceal, A. Martilli, S. E. Belcher, Variation of the Sectional Drag Coefficient of a Group of Buildings with Packing Density. *Bound.-Layer Meteorol.* **128**, 445–457 (2008).

167. M. Saeedi, B.-C. Wang, Large-eddy simulation of turbulent flow and dispersion over a matrix of wall-mounted cubes. *Phys. Fluids.* **27**, 115104 (2015).

168. C. Pozrikidis, *Fluid Dynamics: Theory, Computation, and Numerical Simulation* (Springer, New York, NY, 3rd ed. 2017 edition., 2016).

169. *ANSYS, Inc.* (2018).

170. I. Eliasson, The use of climate knowledge in urban planning. *Landsc. Urban Plan.* **48**, 31–44 (2000).

171. Y. Rydin, A. Bleahu, M. Davies, J. D. Dávila, S. Friel, G. De Grandis, N. Groce, P. C. Hallal, I. Hamilton, P. Howden-Chapman, K.-M. Lai, C. J. Lim, J. Martins, D. Osrin, I. Ridley, I. Scott, M. Taylor, P. Wilkinson, J. Wilson, Shaping cities for health: complexity and the planning of urban environments in the 21st century. *Lancet.* **379**, 2079–2108 (2012).

172. S. Peng, S. Piao, P. Ciais, P. Friedlingstein, C. Ottle, F.-M. Bréon, H. Nan, L. Zhou, R. B. Myneni, Surface Urban Heat Island Across 419 Global Big Cities. *Environ. Sci. Technol.* **46**, 696–703 (2012).

173. J. A. Patz, D. Campbell-Lendrum, T. Holloway, J. A. Foley, Impact of regional climate change on human health. *Nature.* **438**, 310–317 (2005).

174. L. Zhao, M. Oppenheimer, Q. Zhu, J. W. Baldwin, K. L. Ebi, E. Bou-Zeid, K. Guan, X. Liu, Interactions between urban heat islands and heat waves. *Environ. Res. Lett.* **13**, 034003 (2018).

175. C. C. Branas, E. South, M. C. Kondo, B. C. Hohl, P. Bourgois, D. J. Wiebe, J. M. MacDonald, Citywide cluster randomized trial to restore blighted vacant land and its effects on violence, crime, and fear. *Proc. Natl. Acad. Sci.*, 201718503 (2018).

8. Appendix

Matlab code for calculating drag coefficients

```
function city_texture_cd_model (load_name, save_name)
%%

clear
clc
% load LON LAT and AREA
% units for LON, LAT are decimal degrees
% units for AREA is m2
% load('FL_points.mat', 'A', 'X', 'Y')
load(load_name, 'A', 'X', 'Y')
% save_name = 'damage_data.mat';


var_x = 10000;
% tranform LON and LAT (var_x may need experimenting for optimal
performance)
cx = abs(X)*var_x;
cy = abs(Y)*var_x;
xmax = max(cx);
xmin = min(cx);
ymax = max(cy);
ymin = min(cy);
% find average building size
avg_area = exp(nanmean(log(A)));
avg_length = sqrt(avg_area);
% avg_length = nanmean(sqrt(A));

% calculate box size (may need experimenting with the constant)
alpha = avg_length*10;
%move all the coordinates by xmin and ymin, such that (xmin, ymin)-
>(0,0)
cx_new = cx - xmin;
cy_new = cy - ymin;

Nx = ceil((xmax-xmin)/alpha);
Ny = ceil((ymax-ymin)/alpha);
avail = zeros(Nx, Ny);
% distribute buildings into a 3D matrix
counter = length(cx_new);
for h = 1:length(cx_new)
    if (rem(cx_new(h),alpha) == 0) && (cx_new(h)~=0)
        NNx = floor((cx_new(h))/alpha);
    else
        NNx = floor((cx_new(h))/alpha)+1;
```

```
    end
    if (rem(cy_new(h),alpha) == 0) && (cy_new(h)~=0)
        NNy = floor((cy_new(h))/alpha);
    else
        NNy = floor((cy_new(h))/alpha)+1;
    end
    avail(NNx,NNy) = avail(NNx,NNy)+1;
    resv(NNx,NNy,avail(NNx,NNy)) = h;
    counter = counter -1;
    disp(counter);
end
% calculate cut off radius based on average L

timer = 0;
counter = length(cx);
radius=6371;
damage = ones(length(cx), 1);
den = zeros(length(cx), 1);
L = nan(length(cx), 1);
Cn = nan(length(cx), 1);
LAT = zeros(length(cx), 1);
LON = zeros(length(cx), 1);
A_b = nan(length(cx), 1);
for h = 1:size(avail, 1)
    for j = 1:size(avail, 2)
        if avail(h,j) > 0
            for k = 1:avail(h,j)
                lat1 = Y(resv(h,j,k))*pi/180;
                lon1 = X(resv(h,j,k))*pi/180;
                % reference building size
                B_ref_size = sqrt(A(resv(h,j,k)));
                B_neighbor_size = nan(1000, 1);
                dist_local = nan(1000, 1);
                nsur = 0;
                for l = -1:1
                    ii = h + l;
                    for m = -1:1
                        jj = j + m;
                        if (ii>0) && (ii<=size(avail,1)) && (jj>0) &&
(jj<=size(avail,2)) && (avail(ii,jj)>0)
                            for n = 1:avail(ii, jj)
                                if (isequal(cx(resv(h,j,k)),
cx(resv(ii,jj,n))) == 0)...
                                        && (isequal(cy(resv(h,j,k)),
cy(resv(ii,jj,n))) == 0)
                                    % calculate distance between two
GPS
                                    % points
                                    lat2 = Y(resv(ii,jj,n))*pi/180;
                                    lon2 = X(resv(ii,jj,n))*pi/180;
                                    deltaLat=lat2-lat1;
                                    deltaLon=lon2-lon1;
```

```
                                        a=sin((deltaLat)/2).^2 +
cos(lat1).*cos(lat2) .* sin(deltaLon/2).^2;
                                        c=2*atan2(sqrt(a),sqrt(1-a));
                                        % distance in meters
                                        dist=radius*c*1000;
                                        nsur = nsur + 1;
                                        B_neighbor_size(nsur) =
sqrt(A(resv(ii,jj,n)));
                                        dist_local(nsur) = dist;
                                    end
                                end
                            end
                        end
                    end
                    % avg size for buildings within distance alpha
                    avg_length = nanmean([B_ref_size; B_neighbor_size]);
                    rcut = avg_length*3.5;
                    area_circle = pi()*rcut^2;
                    var = dist_local<=rcut;
                    nsur = sum(var);
                    timer = timer + 1;
                    % allocate X to LON and Y to LAT
                    LAT(timer) = Y(resv(h,j,k));
                    LON(timer) = X(resv(h,j,k));
                    A_b(timer) = A(resv(h,j,k));
                    % calculate drag coefficient
                    density_planar =
((B_ref_size^2)+sum(B_neighbor_size(var).^2))/(area_circle);
                    if nsur>0 && density_planar < 0.63 % Ref (108)
                        density_local = (1+nsur)/(area_circle);
                        density_length =
(B_ref_size+sum(B_neighbor_size(var)))/(nsur+1);
                        damage(timer) =
nsur*(9.5*density_local*density_length)^0.5+1; % Eq. (5.18), H=9.5
[Ref (57)]
                        den(timer) = density_local;
                        L(timer) = density_length;
                        Cn(timer) = nsur;
                    else
                        L(timer) = B_ref_size;
                        den(timer) = (1)/(area_circle);
                        Cn(timer) = 0;
                    end
                    counter = counter - 1;
                    disp(counter);
                end
            end
        end
    end
end
A = A_b;

% % % save matlab file
```

```
save(save_name, 'damage', 'LON', 'LAT', 'A', 'den', 'L', 'Cn', 'A')

% % % save CSV file
Cd = damage;
Cd(damage<=2) = 2;
Cd(damage>2 & damage<=3) = 3;
Cd(damage>3) = 4;
Cd_actual = damage;

% % defines columns to save in the table
T = table(LAT, LON, Cd, Cd_actual);
writetable(T, [save_name(1:end-3),'csv']);


end
```